International
Progress Report

IPR-04-31

Äspö Hard Rock Laboratory

Äspö Task Force

Task 6A, 6B and 6B2

Modelling of the STT1B, detailed scale tracer tests at Äspö using the channel network model

James Crawford
Louis Moreno

Chemical Engineering and Technology
Royal Institute of Techonlogy

January 2003

Svensk Kärnbränslehantering AB
Swedish Nuclear Fuel
and Waste Management Co
Box 5864
SE-102 40 Stockholm Sweden
Tel 08-459 84 00
+46 8 459 84 00
Fax 08-661 57 19
+46 8 661 57 19

Äspö Hard Rock
Laboratory

Report no.
IPR-04-31
No.
F65K
Author
James Crawford
Louis Moreno
Date
Jan 2003
Checked by
Jan-Olof Selroos
Date
July 2004
Approved
Christer Svemar
Date
2004-08-26

Äspö Hard Rock Laboratory

Äspö Task Force

Task 6A, 6B and 6B2

Modelling of the STT1B, detailed scale tracer tests at Äspö using the channel network model

James Crawford
Louis Moreno

Chemical Engineering and Technology
Royal Institute of Techonlogy

January 2003

Keywords: Fractured media, channel network, tracer tests, sorption, diffusion

Abstract

The tracer test STT1b with sorbing and non-sorbing species performed as part of the TRUE-1 experiments have been re-evaluated as part of the Task 6A and 6B project. The aim of this project is to gain insights into how transport models used separately for the purposes of site characterisation and performance assessment studies can be harmonised. The STT1b test was carried out in radically converging flow geometry with a travel distance of about 5m. The tracers that have been evaluated in the context of Task 6A and 6B were ^{85}Sr, ^{58}Co, ^{99}Tc. Calibration of the flow porosity was made by evaluation of the breakthrough of the non-sorbing tracers ^{131}I and tritiated water (Hto). In addition to these tracers the theoretical transport of the radionuclide ^{241}Am was also studied even though this was not included in the original experimental study.

The tracer transport was modelled using the Channel Network Model (implemented in the code CHAN3D). An attempt to reconcile the tracer breakthrough data was made by comparing results where 2D and 3D flow assumptions were used in the modelling. Task 6B and Task 6B2 involved the simulation of tracer transport under hydraulic conditions that are more representative of what would be expected under actual repository conditions. Under these conditions, matrix interaction processes play an overwhelmingly important role in determining radionuclide retardation rather than surface sorption which is the primary retardation mechanism operating during the STT1b experiment modelled in Task 6A.

Sammanfattning

Spårämnesförsöket STT1b, som genomfördes under TRUE-1 programmet, har åter utvärderats inom Task 6A och 6B. Målsättningen var att erhålla kunskaper om hur transportmodeller som vanligtvis används separat för platskarakterisering och säkerhetsanalys kan harmoniseras. STT1b-försöket utfördes under en radiell, konvergerande flödesgeometri med ett linjärt avstånd på ca 5 m mellan injektions- och pumpningsborrhålen. Spårämnen som har utvärderats i Task 6A är ^{85}Sr, ^{58}Co, ^{99}Tc. Flödesporositeten kalibrerades genom att jämföra det simulerade och det experimentellt uppmätta genombrottet av de icke-sorberande spårämnena ^{131}I och tritierat vatten (Hto). Transport av ^{241}Am studerades teoretiskt trots att detta spårämne ej ingick i det ursprungliga experimentella försöket.

Spårämnestransporten modellerades med hjälp av kanalnätverksmodellen i simuleringsprogrammet CHAN3D. Simuleringsresultat från modeller med flödesantaganden i 2D respektive 3D har också jämförts för att kunna avgöra systemets flödesdimensionalitet.

Task 6B och Task 6B2 omfattar simuleringar av spårämnestransport under hydrauliska förhållanden som mer liknar de som kan förväntas råda i ett förvar. Under sådana förhållanden har det påvisats att matrisdiffusionsprocesser kommer att ha avgörande betydelse för radionuklidtransporten, medan ytsorption kommer att ha mindre betydelse. Ytsorption är dock den dominerande processen under de experimentella förhållanden som rådde i STT1b-försöket, vilket modellerades i Task 6A.

Executive Summary

The tracer test STT1b with sorbing and non-sorbing species performed as part of the TRUE-1 experiments has been re-evaluated as part of the Task 6A and 6B project. The aim of this project is to gain insights into how transport models used separately for the purposes of site characterisation and performance assessment studies can be harmonised. The STT1b test was carried out in a radially converging flow geometry with a travel distance of about 5m. The tracers that have been evaluated in the context of Task 6A and 6B were ^{85}Sr, ^{58}Co, ^{99}Tc. Calibration of the flow porosity was made by evaluation of the breakthrough of the non-sorbing tracers ^{131}I and tritiated water (Hto). In addition to these tracers the theoretical transport of the radionuclide ^{241}Am was also studied even though this was not included in the original experimental study.

The tracer transport was modelled using the Channel Network Model (implemented in the code CHAN3D). The Channel Network Model assumes that fluid flow and solute transport take place through a network of interconnected channels. It includes solute transport by advection, diffusion into the rock matrix, and sorption within the rock matrix and on the channel surface. Sorption and diffusion data were obtained from compiled laboratory experimental values and the Modelling Input Data Set (MIDS). These data were given as part of the task specification in order that the different modelling groups would use the same data set for making predictions.

An attempt to reconcile the tracer breakthrough data was made by comparing results where 2D and 3D flow assumptions were used in the modelling. Although the results were inconclusive based upon the tracers specified for this task, it is the author's opinion that a 3D flow structure is probably a more accurate representation of the actual system. The results from previous evaluations of tracer data from the STT1b experiments (tracers that have not been examined in this report but considered in Task 4) are strongly suggestive of a 3D flow system. Additionally, the transport aperture estimated if we consider a 2D flow structure in the plane of Feature A (2 mm) appears to be larger than what is reasonable to expect. The 3D flow assumption gives fracture apertures that are much closer to what would be expected, based upon experimental observations e.g., previous experiences during the Stripa project (Birgersson et al., 1992).

Under the hydraulic conditions specified for Task 6B, surface sorption accounts for a much smaller proportion of the simulated tracer retardation and matrix interaction plays an overwhelming role for the transport time of the strongly sorbing tracer ^{241}Am. For the more weakly sorbing tracer ^{58}Co, surface sorption and matrix interaction are equally important retardation mechanisms. This is in contrast to the Task 6A simulations where surface sorption was the overwhelmingly dominant retardation mechanism for ^{58}Co and ^{241}Am.

Many of the qualitative observations made in the Task 6A and 6B studies were also noted in the case studies relating to Task 6B2. In particular, it was found that the flow porosity could be varied over several orders of magnitude without affecting the breakthrough characteristics for strongly sorbing tracers. It was also found that matrix interaction played an overwhelmingly important role for tracer retardation and surface sorption processes had very little influence upon the tracer recovery times.

Contents

Appendices

Appendix 1

Input Data: Some Theoretical Considerations

- Estimation of the Channel Conductance Distribution
- Estimation of the Flow-Wetted Surface in Fractured Rock

Appendix 2

Task 6A. Breakthrough Concentration-Time Curves (BTCs)

- 3D simulations using experimental tracer injection data (3DQ1)
- Breakthrough time summary for modelled tracers (3DQ1)
- Maximum nuclide release rate (3DQ1)
- Comparison of injection pulse data and Dirac pulse arrival times (3DQ1)
- Comparison of 3D simulations (using experimental tracer injection data) with high and low injection flow criterion – 3DQ1 & 3DQ1b
- Breakthrough time summary for modelled tracers (3DQ1b)
- 2D simulations using experimental tracer injection data (2DQ1)
- Breakthrough time summary for modelled tracers (2DQ1)
- Maximum nuclide release rate (2DQ1)
- Comparison of injection pulse data and Dirac pulse arrival times (2DQ1)
- Comparison of 2D simulations (using experimental tracer injection data) with high and low injection flow criterion – 2DQ1 & 2DQ1b
- Breakthrough time summary for modelled tracers (2DQ1b)
- Comparison of 2D & 3D simulations (using experimental tracer injection data) – 3DQ1, 2DQ1
- Comparison of 2D & 3D simulations (Dirac pulse) – 3DQ1, 2DQ1

Appendix 3

Task 6B. Breakthrough Concentration-Time Curves (BTC)

- Comparison of 2D & 3D simulations (Dirac pulse) – 3DQ2, 2DQ2
- Breakthrough time summary for modelled tracers (3DQ2)
- Maximum nuclide release rate (3DQ2)
- Comparison of Task 6A (3DQ1) and Task 6B (3DQ2) tracer arrival times
- Breakthrough time summary for modelled tracers (2DQ2)
- Maximum nuclide release rate (2DQ2)
- Comparison of Task 6A (2DQ1) and Task 6B (2DQ2) tracer arrival times
- Comparison of 2D & 3D simulations (constant injection) – 3DQ2, 2DQ2

Appendix 4

Task 6B2. Breakthrough Concentration-Time Curves (BTC)

- Comparison of selected simulations (Dirac pulse) with and without background fracturing

Appendix 5

Sensitivity Analysis Concerning Channel Lengths

- Comparison of 2D & 3D simulations with varying channel lengths

List of Figures

List of Tables

1 Introduction

1.1 Description of Task 6A and 6B

The Swedish concept for the disposal of high-level nuclear waste (the KBS-3 system) involves encapsulation of spent fuel rods in corrosion-resistant iron-copper canisters surrounded by a bentonite clay buffer at a depth of approximately 500 metres in crystalline bedrock. The canisters are to be located in deposition holes that will be bored in the floors of a system of tunnels comprising the repository. Central to the successful implementation of the KBS-3 system is a meticulous characterisation of potential sites as a starting point for determining an appropriate repository location. In addition to this, a comprehensive performance assessment is also required to give an indication of whether the repository will behave as intended over the geological time scales appropriate for risk analysis.

The goal of site characterisation (SC) is to obtain input data that can later be used in performance assessment (PA) calculations. This input data generally takes the form of parameter values describing the physical and geochemical properties of the studied rock volume. Performance assessment calculations are based upon the premise that there may be one or more initially defective canisters that can leak radionuclides to the surrounding rock (even though the structural integrity of the canister is designed to remain intact for some 100 000 years). The properties of the surrounding rock volume that comprises the natural barrier for radionuclide migration are therefore of overwhelming importance for the operational safety of the repository after closure.

Frequently, the parameter values necessary for PA are obtained from interpretation of field tests and experiments using theoretical models that attempt to capture the essential physics of the flow and transport system. Processes that may be important in a PA setting may not necessarily be dominating processes or may not even be observable in the SC phase. There is therefore a continuing need to bridge the conceptual gaps between the models used to interpret field data during SC and the models used to make PA predictions, and more specifically, how the parameter values derived from SC may be expected to be different in a PA setting.

To provide a methodological basis for this work, an exhaustive program of experimental and theoretical analysis has been undertaken at the Äspö Hard Rock Laboratory (HRL) in the municipality of Oskarshamn, Sweden. The Äspö HRL constitutes an important component of SKB's work to design, construct, and implement a deep geological repository for spent nuclear fuel, as well as to develop and test methods for characterisation of selected repository sites (SKB, 2001).

Radionuclides that are released to the rock volume are transported by the groundwater flowing in fractures within the rock. From the fractures, they may diffuse into and interact with the micro-surfaces within the rock matrix. Diffusion into the rock matrix and retention within the rock mass are important retardation mechanisms for the transport of radionuclides. The retention effect of the rock at Äspö HRL has been studied by tracer tests in the TRUE experimental programme (Tracer Retention Understanding Experiments).

Laboratory investigations have difficulties in simulating representative natural conditions that may exist within a repository environment and require supplementary field studies for corroboration. Theoretical models also require in-data from both laboratory and field investigations, and need to be validated against field observations. For this reason, a programme of modelling tasks has been undertaken as an adjunct to the experimental field studies carried out within TRUE.

The present report concerns the preliminary phase of Task 6 where the stated aim is to provide a bridge between SC and PA approaches to studying solute transport in fractured rock. Both Task 6A and 6B focus upon tracer transport processes at the TRUE-1 site at Äspö on a 5 meter scale.

Task 6A involves the modelling of selected tracers (^{131}I, ^{58}Co, ^{85}Sr, ^{99}Tc) that were used in the STT1b test performed within the TRUE-1 program as well as the sorbing radionuclide ^{241}Am that was not used in the test. The purpose of Task 6A is to provide an initial reference case for future comparison of the modelling efforts carried out within the Task 6 framework.

Task 6B consists of modelling the same tracers investigated in Task 6A using boundary conditions and time scales relevant for performance assessment studies. The purpose of Task 6B is to identify and understand the differences between site characterisation and performance assessment models as well as to study the impact and significance of assumptions made in the modelling work.

1.2 Description of the STT1b Tracer Experiment

A general description of the geological structures at the TRUE-1 site has been given by Winberg et al. (2000), in the *Final Report of the First Stage of the Tracer Retention and Understanding Experiments*. The location, orientation, and extent of these features have been interpreted from mylonitic structures identified in the six boreholes intersecting the rock volume. In all, five hydraulically conductive features extending between two or more boreholes have been identified in the rock volume. These features are denoted A, B, C, D, and NW-2'. In the structural model, Feature A and C are approximated as simple planar structures, while features B, D, and NW-2' are somewhat more complex and are thought to consist of a number of intersecting hydraulically conductive fractures grouped together.

Task 6A and 6B concern the transport and retardation processes occurring in and around the "Feature A" geological structure where the STT1b tracer test was carried out. The tracers were injected in the KXTT1 borehole and recovered in borehole KXTT3. Both the injection and recovery sections (KXTT1-R2 and KXTT3-R2) were packed-off borehole volumes within the plane of Feature A. The locations of Features A-D as well as the injection and recovery locations are shown in Figure 1. Although Features B and D cannot be readily interpreted as planar fractures, an approximate plane of orientation is given in the figure for visualisation purposes.

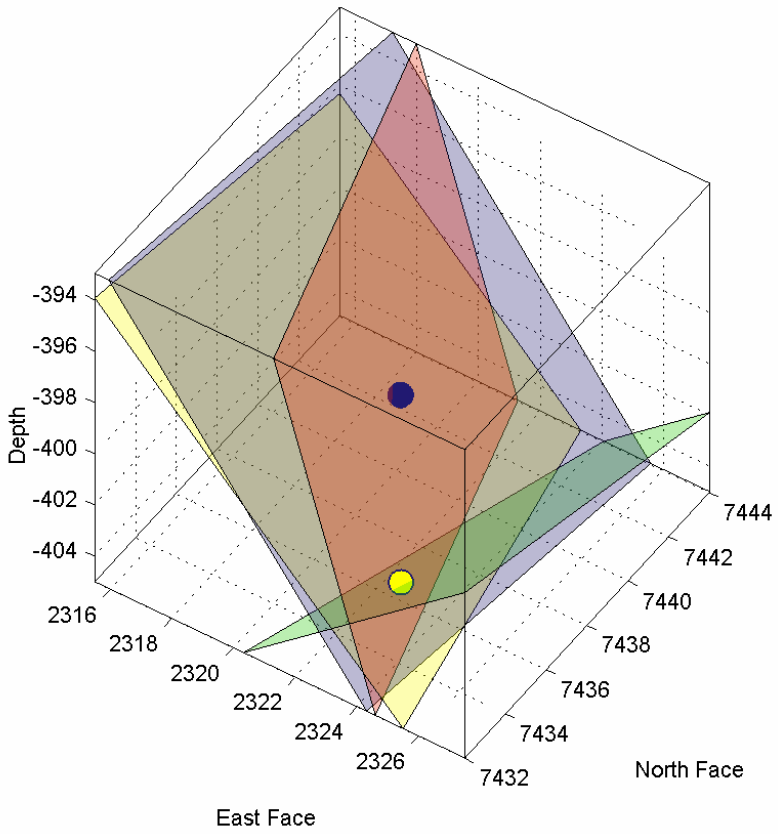

Figure 1 *Schematic showing the location of hydraulically conductive features in the TRUE-1 rock volume at Äspö; Feature A (red), B (blue), C (green), and D (yellow). The yellow marker in the bottom corner of the diagram indicates the tracer injection location, and the blue one the pumping location.*

The tracers that were used in the STT1b test were tritiated water, iodine, strontium, cobalt, and technetium. These tracers represent a broad spectrum of sorption strengths from none to weakly, moderately, and strongly sorbing.

The injection apparatus was designed in such a way that the tracer in the injection section could be quickly exchanged with unlabeled water after a short period, thus enabling the creation of a finite tracer pulse at the injection point. The total volume of the injection section was roughly 1900 ml (including injection loop tubing) over a one-meter packed-off section of the borehole. The packed-off borehole sections in the injection and recovery boreholes were equipped with volume reducers ("dummies") which allowed a 40% reduction in section volume. A more detailed description of the apparatus and the injection procedure can be found in Winberg et al. (2000).

Gamma emitters were detected using an inline High Purity Germanium (HPGe) detector with a Multi-Channel Analyser (MCA) to facilitate simultaneous measurement of all gamma-emitting tracers. Tritiated water (Hto) samples were measured off-site by Liquid Scintillation at the SKB operated radiochemical laboratory BASLAB.

The linear distance from the injection well to the recovery well was 5.03 m. A spherical volume of 5m radius is indicated in Figure 2 below to show the approximate extent of the sampled rock volume (assuming a three-dimensional flow field).

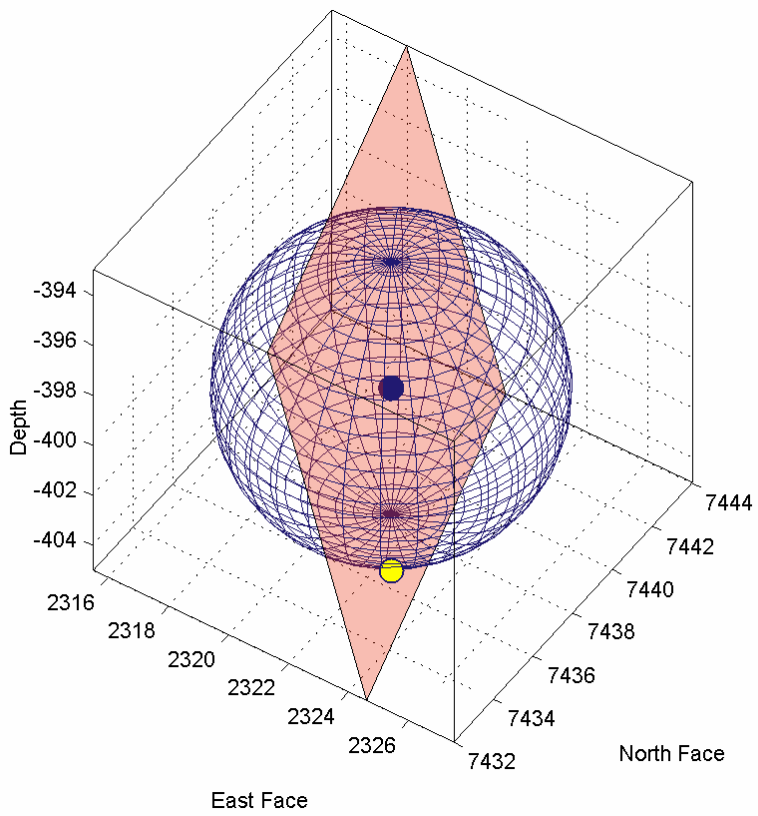

Figure 2 *Schematic showing only Feature A. The sphere inscribed in the rock volume indicates a radius of 5 m from the STT1b pumping location (blue marker). The yellow marker in the bottom corner of the diagram indicates the tracer injection location.*

1.3 Description of Task 6B2

At the 15th Task Force meeting in Goslar, Germany, an extension of the task was proposed (Task 6B2). In this task the boundary conditions are modified to produce flow and transport over a larger area of Feature A. The input boundary is no longer a point source and the tracers are assumed to be collected in a fracture intersecting Feature A as shown in Figure 3 below:

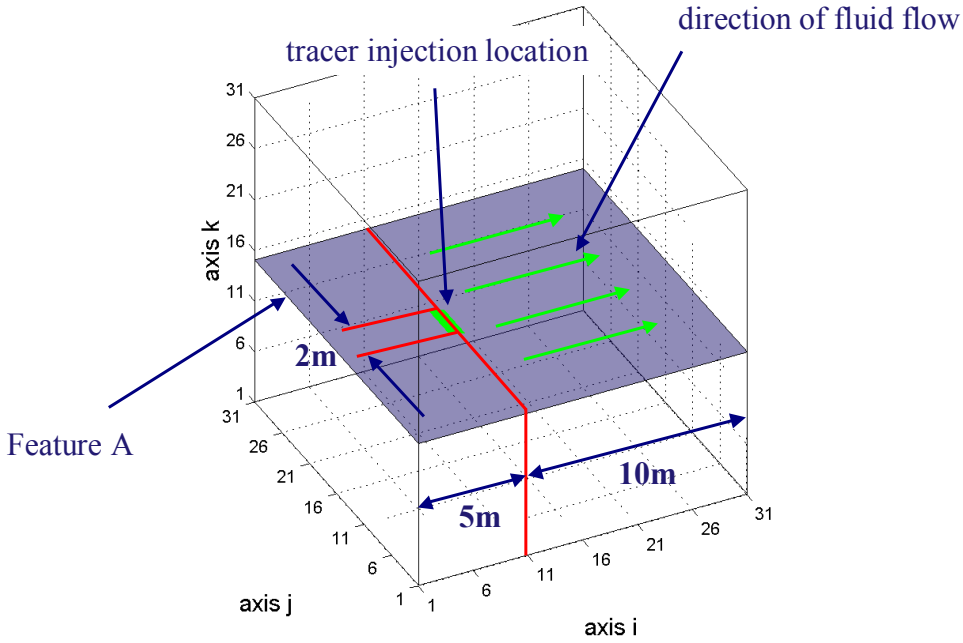

Figure 3 *Principal geometry for Task 6B2. Feature A is visualised as a blue plane intersecting the simulation volume. The tracer injection location is indicated as a green line of length 2 m.*

The modelling Task 6B2 focuses upon transport in Feature A. The situation envisaged is of a PA-type where there is no tunnel or extraction borehole causing drawdown. Instead the water flow is governed by small natural gradients. In this modelling task, the water flow in Feature A is assumed to be governed by the head difference between two fractures intersecting Feature A, positioned roughly where Feature B and NW-2' are interpreted to intersect Feature A. However, for the modelling task the two fracture intersections have been assumed to be parallel in order to simplify the geometry. In Figure 3 the bounding planes perpendicular to the illustrated direction of flow correspond to these intersecting planes. A hydraulic gradient of 0.01 was applied over the simulation volume which was 15 m in extent.

Injection is assumed to occur along a line source, 2m in length overlapping the position of borehole section KXTT1-R2. The distance from the upstream intersecting fracture to the injection line is 5 metres. The flow will follow the general direction of the flow path used in STT1b, i.e. from KXTT1 to KXTT3. However, in this case no pumping will occur in KXTT3. Tracer is collected in the recovery fracture, situated a distance of 10 meters downstream from the injection section.

The tracers to be modelled for Task 6B2 were the same as those used in Task 6A and 6B (i.e., ^{131}I, ^{85}Sr, ^{58}Co, ^{99}Tc and ^{241}Am). Two types of tracer injection boundary condition were considered; a constant injection of 1 MBq/year and a unit Dirac pulse input.

2 The Channel Network Model – CHAN3D

2.1 Solute transport in a channel

Within an individual channel, the tracer is transported by advective flow. At the same time, the tracer may diffuse from the channel into the rock matrix. This is what is referred to as matrix diffusion.

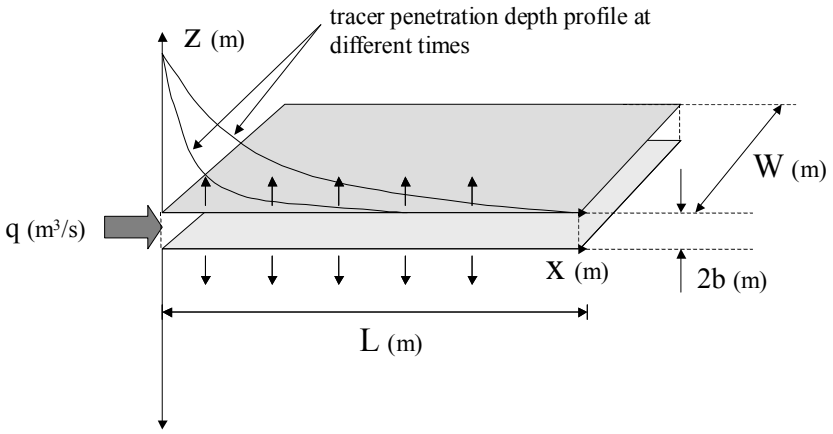

Figure 4 *Conceptual illustration of tracer transport within a channel combined with diffusion within the rock matrix. Advective flow occurs in the channel along the x-axis, while matrix diffusion is outwards into the rock volume perpendicular to the fracture plane.*

An unsteady-state, differential mass balance is used to describe the advective transport of the tracer, linear sorption on the fracture surface, and diffusion from the channel into the rock matrix. In the absence of radioactive decay, this mass balance is:

$$\left(1+\frac{K_a}{b}\right)\frac{\partial C_f}{\partial t} = -\frac{q}{2Wb}\frac{\partial C_f}{\partial x} + \frac{D_e}{b}\frac{\partial C_p}{\partial z}\bigg|_{z=0} \qquad (1)$$

Here, C_f is the aqueous concentration in the fracture, C_p is the porewater concentration, K_a is the surface sorption coefficient, b is the fracture half-thickness, W is the channel width, D_e is the effective diffusivity, and q is the advective flowrate in the channel. The term on the left-hand side of the equation is the accumulation term describing the rate of change of concentration in the fracture water, where sorption of tracer on the fracture surface is accounted for. On the right-hand side of the equation are the advective flux term and the matrix diffusive flux term, respectively.

A similar mass balance is used to describe the diffusive transport and linear sorption of a tracer within the rock matrix.

$$K_d \rho_p \frac{\partial C_p}{\partial t} = D_e \frac{\partial^2 C_p}{\partial z^2} \tag{2}$$

Where,

$$K_d \rho_p = \varepsilon_p + \left(1 - \varepsilon_p\right) \cdot K_d' \rho_s$$

The variables K_d and K_d' are the matrix sorption coefficients based upon the bulk (ρ_p) and solid densities (ρ_s), respectively; ε_p is the matrix porosity (Neretnieks, 1980). As the matrix porosity is very low in igneous rocks, the bulk and solid densities are for all practical purposes the same.

In the rock matrix differential mass balance, the accumulation term on the left-hand side of the equation gives the rate of change of the pore water concentration within the rock matrix, where the sorbed concentration of tracer is simultaneously accounted for. The term on the right-hand side of the equation is the diffusive flux term for the tracer.

For an instantaneous "step" change in concentration at the mouth of the channel, the coupled mass balances can be solved to give an analytical solution for the tracer concentration at the channel outlet. This is the breakthrough curve or BTC for the channel. In terms of the flow-wetted surface, this is:

$$\frac{C(t)}{C_0} = \begin{cases} 0 & \text{for } t \le R_* t_w \\ \operatorname{erfc}\left[\frac{1}{2} \left(\frac{D_e K_d \rho_p}{t - R_* t_w} \right)^{\frac{1}{2}} \cdot \frac{FWS}{q} \right] & \text{for } t > R_* t_w \end{cases} \tag{3}$$

The variable R_* is the retardation constant for surface sorption given by:

$$R_* = 1 + \frac{K_a}{b}$$

2.2 The Channel Network Model

The simulations were made using the CHAN3D computer program (Gylling, 1997) which is based in the Channel Network Model (Moreno and Neretnieks, 1993). The model takes into account the uneven flow distribution observed in fractured rock and the stochastic nature of the hydraulic features, and it includes retarding physical processes like matrix diffusion and sorption within the matrix. Sorption onto the fracture/channel surfaces is also included. One of the important aspects of the model is its ability to accommodate the transport of solutes that diffuse into the rock matrix and may be sorbed within the matrix.

The flow paths are assumed to make up a network of flow channels in the rock and the model concept assumes that fluid flow and solute transport take place in a three-dimensional network of channels. The hydraulic properties of individual channels can be generated by including the effects of different lengths, different hydraulic conductivities, and other properties of interest. Data can be obtained from borehole transmissivity measurements and observations of fracture widths (Gylling et al., 1998).

Conceptually, the channel network model considers that there can be up to six interconnected channels at the point of fracture intersection. This is partially based upon the premise that when fracture planes intersect, preferential flowpaths or channels in the plane of one fracture can interconnect both with channels in the other plane as well as the stream tube along the line of plane intersection. The interconnecting channels at a fracture intersection may appear similarly to that shown in Figure 5.

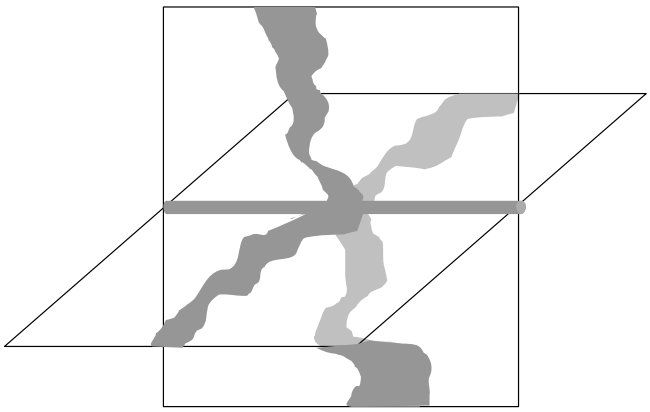

Figure 5 *Illustration of interconnected channels both within the fracture planes as well as at the line of fracture intersection.*

Although the geometry of intersecting channels may be randomly oriented within the rock, the channel network model considers a regular, rectangular grid of channels as shown in Figure 6.

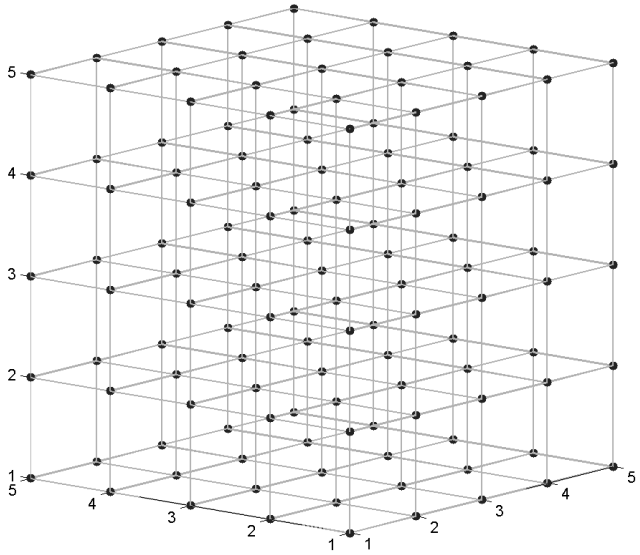

Figure 6 *Schematic view of the channel network made up of interconnected mixing nodes. Each node is connected to six other nodes in a regular, rectangular grid arrangement.*

Each member of the network is assigned a hydraulic conductance. This is the only entity needed to calculate the flow, if the pressure field is known. If the residence time for non-interacting solutes is to be calculated, then the volume of the channel members is also needed. If sorption onto the fracture surface or diffusion into the matrix is to be included in the model, the flow-wetted surface area must also be included. Some properties of the rock are needed, such as rock matrix porosity, diffusivity, and sorption capacity for sorbing species.

The properties of individual channels may differ considerably if a large standard deviation is used for the log-normal conductance distribution. This leads to a sparse flow system where there will be a few channels with relatively large flowrates and some with almost no flow at all. This is similar to what is observed in fractured rock when hydraulic tests are carried out.

2.3 CHAN3D

The simulations were made using the CHAN3D computer program. The code CHAN3D is actually two separate programs: the CHAN3D-flow program that computes the flow field in the rock fracture system, and the CHAN3D-transport program that computes the transport of solutes in the fracture system once the flow field is established using CHAN3D-flow.

2.3.1 Flow Modelling

Each member of the network is assigned a hydraulic conductance. The conductance is defined by analogy with electric networks where it is the reciprocal of resistance. Here, the flow may be expressed as the channel conductance multiplied by the hydraulic head difference between its ends:

$$q_{ij} = C_{ij}\left(H_i - H_j\right) \tag{4}$$

The variable q_{ij} is the flow through the channel connecting the nodes i and j, C_{ij} is the channel conductance; H_i and H_j are the hydraulic heads at these nodes. Furthermore, at each node i, we have the hydraulic analogy of Kirchoff's current law:

$$\sum_j q_{ij} = 0 \qquad \text{for all } i \tag{5}$$

This means simply that the net flow of water into a node should also equal the flow out of the node under steady state conditions.

The solution of this system of equations gives the hydraulic head at each node. For a network of nodes interconnected in this way, we must solve a sparse system of linear equations. The CHAN3D-flow program solves this equation system using an iterative, sparse linear equation solver. Once the hydraulic head at each node is known, the flow between adjacent channels may be calculated using equation 4.

In the present simulations, the conductances of the channel members were assumed to be log-normally distributed and not correlated in space. Owing to lack of data, the channel volume was estimated by assuming that the conductance of a channel is proportional to the cube of the channel aperture. The proportionality constant is determined, based upon the estimated flow porosity of the system. The flow porosity is determined from the residence time distribution (RTD) for a non-sorbing (conservative) tracer in the system being studied.

2.3.2 Transport Modelling

The solute transport is simulated in the CHAN3D-transport program by using a particle-following technique (Robinson, 1984; Moreno et al., 1988). Many particles are introduced, one at a time, into the known flow field at one or more locations. Particles arriving at an intersection are distributed in the outlet channel members with a probability proportional to their flow rates. The residence time of an individual particle along the whole path is determined as the sum of residence times in every channel member that the particle has traversed. The residence time distribution is then obtained from the residence times of a multitude of individual particle runs. Hydrodynamic dispersion in the individual channels is considered to be negligible. Dispersion arises instead in the model as a result of the varying transit times for particles taking alternate routes through the channel network.

In Equation 3, the right-hand side is also the cumulative probability function for the arrival time of a Dirac pulse concentration boundary condition. It therefore gives the cumulative probability vs. time for the arrival of individual tracer "particles" subject to advective transport and matrix diffusion in a channel. The derivative of the F-curve gives the so-called E-curve of the residence time distribution (RTD).

Using the probability density analogy it is possible to use the technique developed by Yamashita and Kimura (1990) to find the travel time for individual tracer particles in a channel. The travel time for each particle is determined by choosing a uniform random number in the interval [0,1]. The travel time is then calculated by solving for t in equation 6.

$$\left[R\right]_0^1 = \operatorname{erfc}\left[\frac{1}{2}\left(\frac{D_e K_d \rho_p}{t - R_* t_w}\right)^{\frac{1}{2}} \cdot \frac{FWS}{q}\right] \tag{6}$$

In this analysis, the sorption of tracer is modelled as a linear process. This means that the sorbed concentration is linearly proportional to the dissolved tracer concentration. This may not always be strictly true, but is a useful approximation that is reasonably valid for low concentrations.

For a Dirac pulse boundary condition, the arrival times are calculated for a large number of particles released into the channel network. This considers that all the particles are released simultaneously. The cumulative probability curve is then given as the proportion of particles arriving before a given time in the particle residence time distribution.

For a non-Dirac pulse injection condition, the particles are released at different times according to the cumulative tracer injection curve. The arrival time for an individual particle is then equal to the sum of residence times in every channel member that the particle has traversed, plus a time delay calculated directly from the cumulative tracer mass injection curve.

3 Input Data for the Simulations

3.1 Conductivity Distribution and Flow-Wetted Surface

The distributions of channel conductances used in the CHAN3D simulations are determined from the experimentally measured transmissivity distribution in the boreholes intersecting the rock volume being studied. The data consists of ca. 20-30 transmissivity measurements made with 0.5 m packer intervals in each of the boreholes KA3005, KXTT1, KXTT2, KXTT3, and KXTT4 giving a total of 130 measurements. Roughly 24 transmissivity measurements were made with packer intervals exceeding 0.5 m. The measured distribution of hydraulic conductivities is shown in Figure 7 below along with a normal probability plot of the data:

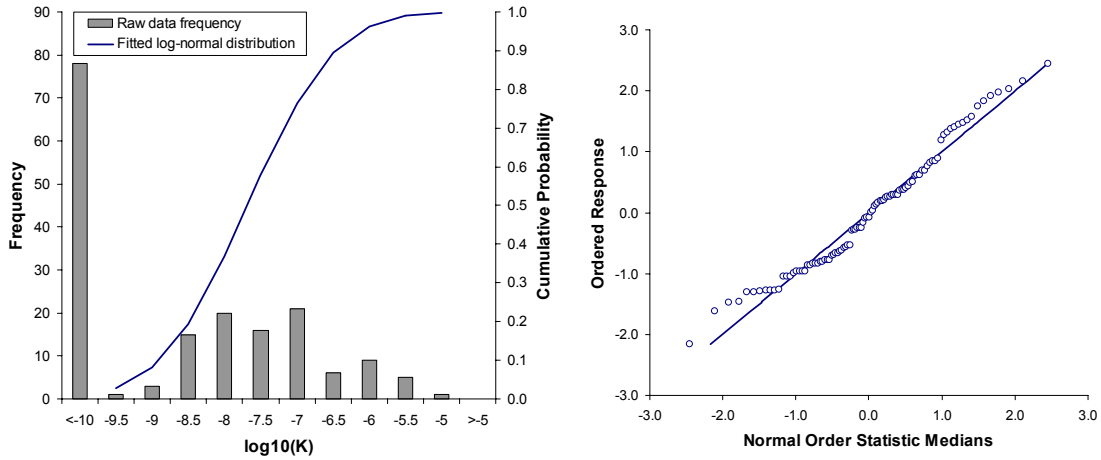

Figure 7 *The distribution of hydraulic conductivities K [m/s] in the rock mass surrounding Feature A. The left-hand figure gives the frequency histogram along with a fitted cumulative log-normal distribution for the data (the first bar indicates sections with a flowrate under the limit of detection). The figure on the right-hand side is a normal probability plot of the log-transformed data. The data fall along the 45° diagonal line indicating that the data can be represented as a log-normal distribution.*

As the log-transformed data approximately coincide with the 45° diagonal in the normal probability plot, we conclude that the distribution of hydraulic conductivities can be described reasonably accurately as a log-normal distribution. The distribution based upon the $\log_{10}$-transformed data has a mean, $\mu_{LK} = -7.68$ and standard deviation, $\sigma_{LK} = 0.95$.

To convert from hydraulic conductivity (m/s) to channel conductance (m^2/s) we use the formula (for details see appendix 1):

$$\mu_{LC} = \log_{10}(Z) + \mu_{LK} \tag{7}$$

$$\sigma_{LC} = \sigma_{LK} = 0.95 \tag{8}$$

where Z is the channel length to be used in the CHAN3D simulation model. μ_{LC} and σ_{LC} are the mean and standard deviation of the log-normal conductance distribution; μ_{LK} and σ_{LK} are the mean and standard deviation of the log-normal hydraulic conductivity distribution.

3.2 Flow-Wetted Surface

If the extents of conductive fractures are large in relation to the borehole diameter and they are randomly distributed (oriented) in space, it can be shown that the flow-wetted surface (FWS) per unit volume of rock, a_R is estimated by (Crawford et al., 2003):

$$a_R \approx -\frac{4}{L}\ln(P_0) \tag{9}$$

Where P_0 is the fraction of non-conductive intervals identified in hydraulic packer tests and L is the packer separation. From the hydraulic tests described above, roughly 40% of the packer intervals were found to be non-conductive in the rock mass surrounding Feature-A. Using these equations we find that the most likely value for FWS per unit volume of rock is:

$$a_R \approx 7\ \mathrm{m}^2/\mathrm{m}^3$$

The $100(1-\alpha)\%$ binomial confidence interval for the estimated a_R may be calculated with the expression:

$$-\frac{4}{L}\ln(P_U) \le a_R \le -\frac{4}{L}\ln(P_L) \tag{10}$$

For a data set consisting of n measurements, the two-sided confidence limits (P_U and P_L) are determined by solving the associated cumulative binomial probability equations:

$$\sum_{k=0}^{nP_0}\binom{n}{k}P_U^k(1-P_U)^{n-k} = \alpha/2 \tag{11}$$

$$\sum_{k=0}^{nP_0-1}\binom{n}{k}P_L^k(1-P_L)^{n-k} = 1-\alpha/2 \tag{12}$$

If the various assumptions used in deriving a_R are reasonably valid, the 95% confidence interval based upon purely statistical considerations is:

$$5.6 \le a_R\ [\mathrm{m}^2/\mathrm{m}^3] \le 8.9$$

In the CHAN3D model, the FWS per unit volume of rock must be scaled to give the average FWS per channel. For this calculation, we consider a “unit cell” to be a cube with dimensions equal to the channel length used in the model. Each unit cell within the

CHAN3D grid has 12 channels corresponding to the edges of the cube. If we consider a cubic volume of rock containing many unit cells, each channel is shared between four adjacent cells, the total number of channels in a continuous rock volume therefore being three times the number of cells.

The total number of channels multiplied by the FWS per channel must equal the rock volume multiplied by the FWS per unit volume of rock. The FWS for a channel is thereby given by the formula:

$$FWS = \left(\frac{Z^3}{3} \right) a_R \tag{13}$$

For Task 6, separate simulations have been made for both a 3D flow structure as well as a purely 2D flow structure representing Feature A. In the 2D model, we assume that there is a single fracture where all solute transport occurs. This is achieved in the CHAN3D program by multiplying all conductances in the hypothetical fracture plane by an arbitrary factor of 50. This gives channel conductances in the fracture plane that are significantly higher than in the surrounding grid.

Since the flowrate in the fracture plane is determined by the pumping flowrate, the arbitrary multiplication factor therefore has no physical significance for the transport problem, with the exception of encouraging preferential flow in the Feature A fracture plane.

For a 2-D fracture, we implicitly have a FWS equal to 2 m^2 per square meter of fracture (since the fracture has 2 surfaces). To simplify the problem definition, the Feature A fracture is defined in the regular plane of the grid structure rather than at an oblique angle to the grid. The fracture plane then contains a regular structure of "unit squares" with edges equal to the channel length. In direct analogy to the 3D case, the total number of channels multiplied by the FWS per channel must equal the fracture area multiplied by the FWS per fracture area. The scaling factor for the 2D case is thus:

$$FWS = \left(\frac{Z^2}{2} \right) 2 = Z^2 \tag{14}$$

For a channel length of 0.5 m, the scaled values for the FWS per channel are:

$FWS = 0.30$ m^2/channel (3D case)

$FWS = 0.25$ m^2/channel (2D case)

The total FWS in the 3D model is however, larger than that for the 2D case owing to the larger number of channels in the 3D model. It is the quotient FWS/q, however, that is critical for the retardation of sorbing tracers rather than the total available FWS. The total FWS in the 3D sphere of 5 m radius surrounding the recovery node is approximately 3700 m^2. If we consider Feature A to be an isolated deterministic fracture, the total FWS in the 2D disk of 5 m radius surrounding the recovery node is only 160 m^2. The available FWS is thus 23 times greater in the 3D simulations than in the 2D simulations.

Based upon the total FWS and total flowrate Q, the overall ratio FWS_{tot}/Q is consequently 23 times greater for the 3D scenario than for the 2D scenario, noting that the pumping flowrate is the same for both scenarios. If we make the assumption that the flowrate at the injection location is representative of the average that should be found at a distance of 5 metres from the pumping section, the average *FWS/q* ratio that an individual package water "sees" should preserve the same ratio:

$$\frac{FWS_{tot}}{Q} \approx \frac{FWS}{q} \tag{15}$$

3.3 Matrix Diffusion and Sorption Data

The matrix diffusion and sorption data for the different tracers used in the CHAN3D simulations was taken from the Task 6A and 6B Modelling task specification (Selroos and Elert, 2001). These data consisted of mass sorption coefficients (K_d'), surface sorption coefficients (K_a) and effective diffusivities (D_e) for each tracer. The bulk sorption coefficient (K_d) is related to the mass sorption coefficient (K_d') using:

$$K_d \rho_p = \varepsilon_p + \left(1 - \varepsilon_p\right) K_d' \rho_s \tag{16}$$

Here, ρ_p is the bulk density of the rock matrix including void space, ρ_s is the density of the rock without voids, and ε_p is the matrix porosity. As the porosity of Äspö diorite is very low, the bulk density, ρ_p is for all practical purposes numerically identical to the rock density, ρ_s. For a bulk density of 2700 kg/m^3 and a matrix porosity of 0.1%, the parameters used in the "base-case" simulations were as follows:

Table 1 Sorption and diffusivity parameters for base-case simulations. Data for ^{131}I, ^{99}Tc, ^{58}Co, and ^{241}Am are taken from table 3-2 in the task specification. Data for Hto and ^{85}Sr are taken from table G-1.

	Hto	^{131}I	^{85}Sr	^{99}Tc	^{58}Co	^{241}Am
K_d' [m^3/kg]	0	0	4.7×10^{-6}	0.2	8×10^{-4}	0.5
K_a [m]	0	0	8×10^{-6}	0.2	8×10^{-3}	0.5
D_e [m^2/s]	1.2×10^{-13}	8.3×10^{-14}	4×10^{-14}	4×10^{-14}	2.9×10^{-14}	4×10^{-14}
$\sqrt{D_e K_d \rho_p}$ [m/y^{½}]	6.15×10^{-5}	5.12×10^{-5}	1.31×10^{-4}	2.61×10^{-2}	1.41×10^{-3}	4.12×10^{-2}

The data contained in Table 3-2 in the task specification are not based upon Äspö material, but are derived from other experimental studies and values used in safety assessments (Carbol and Engkvist, 1997; Ohlsson and Neretnieks, 1997; Vieno and Nordman, 1999). Table G-1 in the task specification is the Modelling Input Data Set (MIDS) described in Winberg et al. (2000) and represents average values for sorption and diffusivity obtained from through-diffusion tests on unaltered Äspö diorite rock samples.

The values of K_a given in the task specification are estimated both by interpretation of batch sorption data and in some cases by dividing the mass sorption constant, K_d' by approximately known values of the BET-surface area for the rock.

The assumption of linear sorption is at best an approximation and is highly dependent upon the geochemical characteristics of the rock and its internal surface area as well as the geochemical composition of the pore water. Sorption coefficients are dependent upon both ionic strength and pH. The sorption data used are valid for a saline groundwater with an ionic strength in the range I = 0.1-0.4, pH 7-9, and a temperature of 10-30°C.

It is not known whether the data obtained from laboratory experiments are truly representative of the rock volume surrounding Feature A that the tracers came into contact with during the STT1b field experiments. It is, however, known that the surfaces of Feature-A are geochemically different to unaltered Äspö diorite. For this reason there is some degree of uncertainty regarding the actual value of sorption constants (K_d'), matrix porosities (ε_p) and effective diffusivities (D_e) that should be used for simulations of the various tracers.

In order to illustrate the range of parameter values that are possible for the different tracers, the matrix variable $\sqrt{D_e K_d \rho_p}$ and sorption constant K_a are plotted in Figure 8. Data are also plotted for ^{85}Sr, ^{58}Co, ^{99}Tc, and ^{241}Am corresponding to the base-cases specified in Table 1 (triangular markers) as well as a number of weakly sorbing tracers for both Feature-A specific rock (filled circles) and unaltered Äspö diorite (non-filled circles).

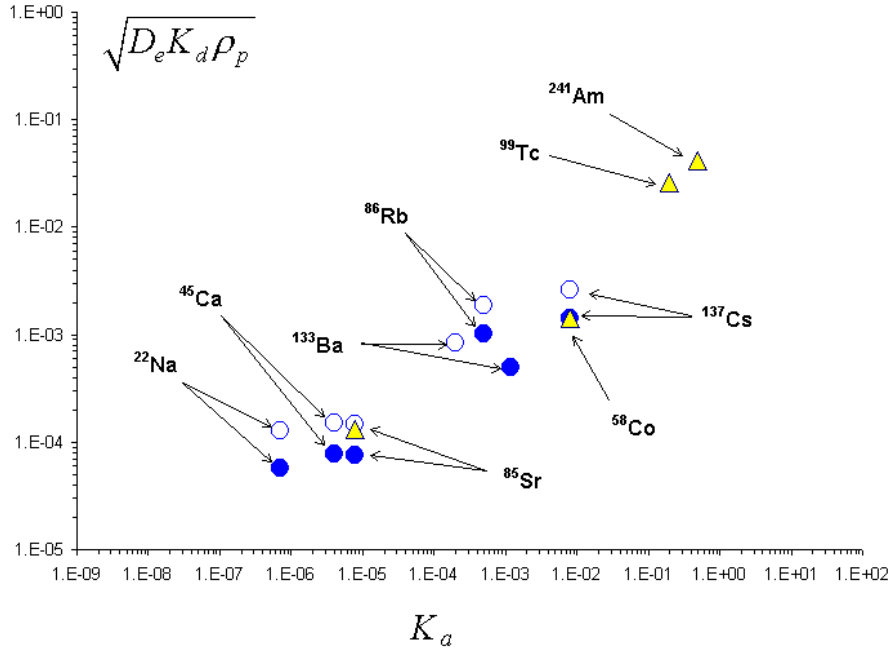

Figure 8 *"Parameter space" diagram indicating relative matrix diffusion and sorption properties of different tracers. Y-axis has units [m/y^{½}]; X-axis has units [m]. The triangular markers indicate values for ^{85}Sr, ^{58}Co, ^{99}Tc, and ^{241}Am based upon the data given in the task specification. Filled circles indicate data for Feature A rock samples. Non-filled circles correspond to Äspö diorite.*

3.4 Tracer Injection Data

The radionuclide tracers Hto (tritiated water), ^{131}I, ^{58}Co, ^{85}Sr, ^{99}Tc were injected passively using the flowrate through the injection section in borehole KXTT1-R2. The flowrate was induced by pumping water from the recovery borehole KXTT3-R2 at a rate of 0.401 l/min to achieve a radially converging flow field.

After four hours, the tracer in the injection section was exchanged with unlabeled water, thus giving an injection pulse of finite duration. The induced flowrate in the injection section was estimated to be 41.9 ml/h during the first four hours and 58.1 ml/h during the period from 20-151 hours. Owing to the flushing of the injection section, no flow estimates were available for the period from 4-20 hours.

Figure 9 below shows the injection time history for the tracers used in the STT1b experiments. The injection data is given as the activity (Bq/kg $_{H2O}$) in the injection section as a function of time.

For the simulations, the injection time history of ^{241}Am was taken to be the same as for ^{58}Co. In accordance with the task specifications, radioactive decay was not considered in the modelling work.

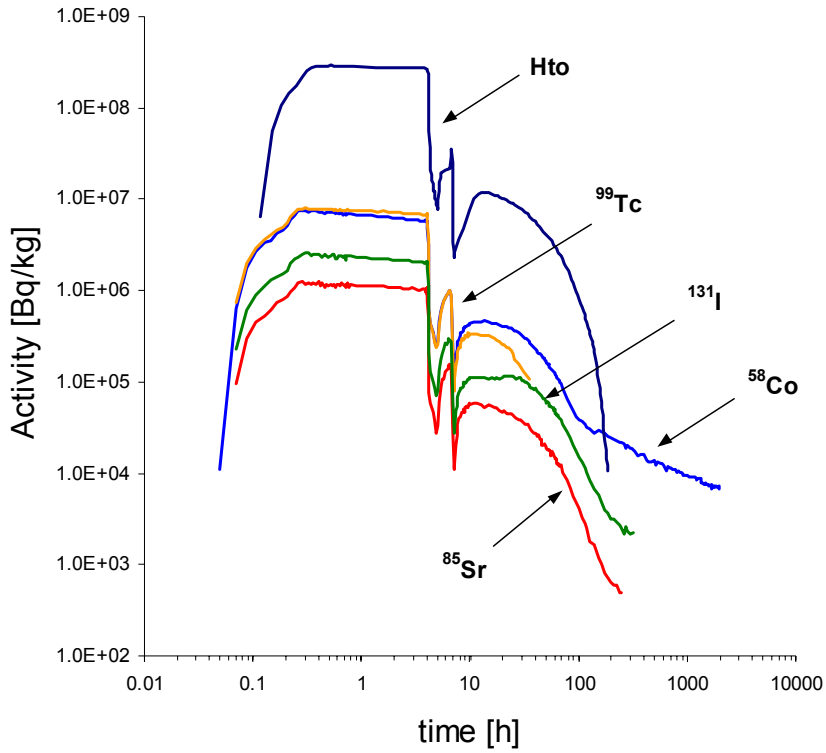

Figure 9 *Tracer concentration at the injection borehole as a function of time for the STT1b experiment. Concentration is expressed as activity [Bq/kg$_{H2O}$].*

4 Task 6A Simulations

In Winberg et al. (2000) the typical range of transmissivity estimated from hydraulic tests for Feature A is 8×10^{-9} – 4×10^{-7} m^2/s. Taking the upper value of this estimate, the transmissivity is roughly one order of magnitude greater than the mean transmissivity estimated for the surrounding rock volume (4×10^{-8} m^2/s). Although the hydraulic data suggest that most of the flow should occur in the plane of Feature A there is some uncertainty as to whether the transport of tracers in the STT1b test occurs solely in the plane of Feature A, or in a pseudo-spherical (3-dimensional) flow structure.

One of the reasons for suspecting a 3-dimensional flow structure is that the residence time measured for conservative (non-sorbing) tracers requires a fracture aperture larger than that which is observed for the system.

For a 2-dimensional flow structure, the water flows in a radial direction from the injection borehole to the recovery section in the plane of Feature A as shown in Figure 10 below:

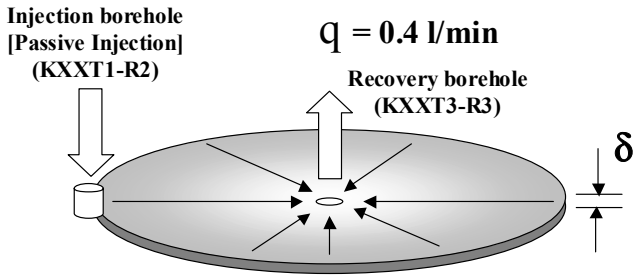

Figure 10 *Schematic of 2-dimensional flow system envisaged for Feature A. The circular disk defines the region of Feature A that is within a radius of 5 m from the recovery section. The water flow is assumed to occur radially in the plane of the disk only.*

The mean residence time for water (t_w) in the circular disk above is defined as:

$$t_w = \frac{\pi r^2 \overline{\delta}}{q} \tag{17}$$

Where r is the radius of the disk, q is the pumping flowrate, and $\overline{\delta}$ is the average aperture of Feature A. The mean residence time is also equal to the first moment of the residence time distribution (RTD) function, or E-curve for the system. The E-curve can be obtained by deconvolution of the tracer concentration-time, breakthrough profile with the injection time history of the tracer. Based upon visual "best fit" of the simulated system with the measured breakthrough curves, the water residence time is estimated to be 6.1 h.

For a disk radius of 5 m and a pumping flowrate of 2.4×10^{-2} m^3/h (0.40 l/min), the effective mean aperture of Feature A is thereby estimated to be roughly 2 mm.

For a 3-dimensional flow structure, the water flows in a radially converging direction within the spherical volume enclosing Feature A as shown in Figure 11 below:

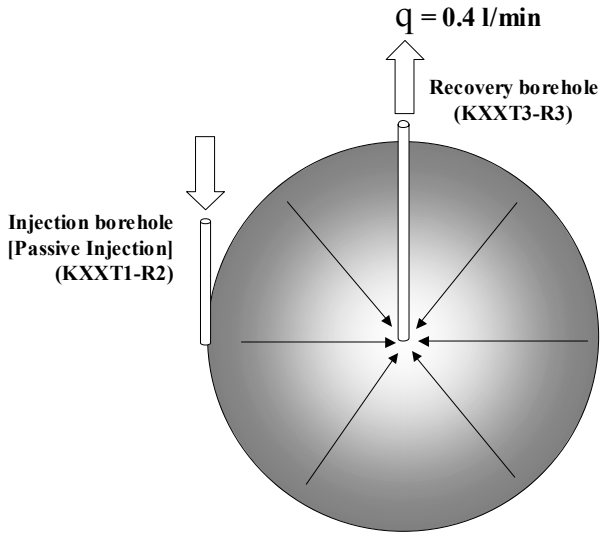

Figure 11 *Schematic of 3-dimensional flow system envisaged for Feature A. The spherical volume defines the region enclosing Feature A that is within a radius of 5 m from the recovery section. In this case the water flow is assumed to occur in a radial direction throughout the volume of the sphere.*

The mean residence time for water (t_w) in the spherical volume is defined as:

$$t_w = \frac{4\pi r^3 \varepsilon_f}{3q} \tag{18}$$

Where ε_f is the flow porosity of the system. The flow porosity is related to the average channel aperture and the flow-wetted surface by:

$$\bar{\delta} = \frac{2\varepsilon_f}{a_R} \tag{19}$$

It should be noted here, that the 3D flow structure is not considered to be a homogeneous porous medium as the equations above may suggest, but rather a set of more or less evenly distributed flow-channels in a non-specific 3D arrangement. The channels do not necessarily correspond to single or multiple fractures, but rather represent paths of preferential flow in the heterogeneously fractured rock.

By visual curve fitting of the simulated system with the experimental breakthrough curves and an estimated specific flow-wetted surface of $a_R \approx 7$ m^2/m^3, the water residence time is found to be on the order of 5.7 h. This gives an average fracture aperture of 0.07 mm.

If tracer tests are performed using different travel distances, but the same extraction flowrate, it is expected that the travel times increase with r^3 for a 3-D and with r^2 for a 2-D system. So, to distinguish whether the system is best described with a 2D or 3D flow structure requires measurements to be made over different length scales. As the

STT1b experiment considers only one transport length scale (5 m), it is not possible to distinguish which flow regime best describes the actual situation.

Owing to the uncertainty of the actual flow dimension of the system, both flow geometries (2D and 3D) have been initially considered for the Task 6A simulations. There is also the possibility that the flow system is essentially 3D in nature, but with some preferential flow in Feature A (i.e., the hydraulic conductivity of Feature A is higher than in the surrounding rock volume). This will give a system that has characteristics intermediate to those of the 2D and 3D flow descriptions.

4.1 Simulations for a 3D Flow System

This is the limiting 3D assumption where we consider that Feature A as a distinctive hydraulic feature does not exist as such, and the conductivity of Feature A is thereby the same as the surrounding rock.

For the transport calculations, injection nodes 5 m distant from the recovery section were randomly selected during each realisation. If the net flowrate through the selected node corresponded to the average mean flowrate (±20%) that would be expected for spherical flow at a radius of 5 metres then it was used for the simulation. If the net flowrate through the selected node was outside this window, then the node was rejected and another node was tested. The average flow that would be expected at a distance of 5 m from the pumping node, was estimated with the formula:

$$F_m \approx Z^2 \left(\frac{q}{4\pi r^2} \right) \tag{20}$$

Where Z is the channel length, q is the pumping flowrate, and r is the distance from the injection node to the pumping node. Equation 20 is based upon the premise that each node distributed on the surface of a virtual sphere of radius r, subtends an area roughly corresponding to Z^2. The average flowrate that would be expected through the node is then equal to the radial water flux multiplied by the area subtended by an individual node. For a channel length of 0.5 m, a transport distance of 5 m, and a pumping flowrate of 0.401 l/min, the expected flowrate (F_m) is 19 ml/h.

As Feature A was assumed to have the same stochastic properties as the rest of the rock volume, it was not required for the injection nodes to necessarily lie in the hypothetical Feature A plane. The locations of a number of injection nodes used for the simulations are illustrated in Figure 12 below:

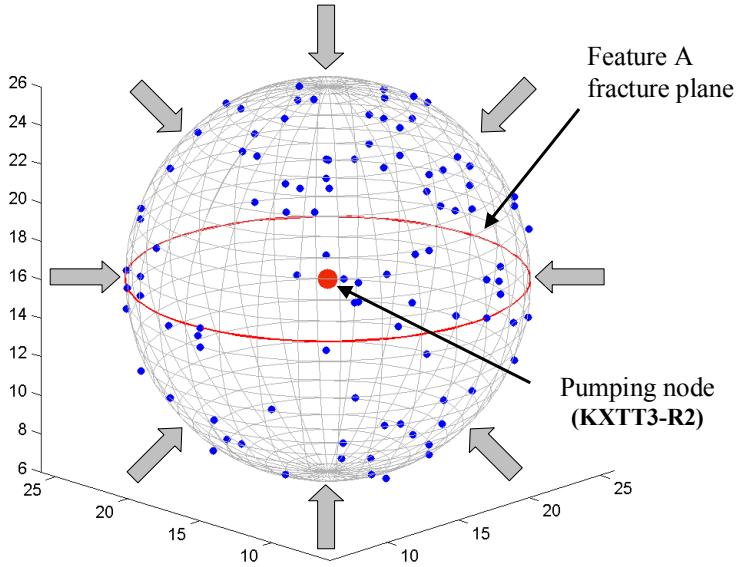

Figure 12 *Visualisation of injection locations for 3D simulations where the Feature A channels have identical stochastic properties to the rest of the rock volume. Injection locations are visualised as blue markers on the sphere surface.*

Figure 13 below shows the results of 100 realisations for Hto transport using the estimated flow porosity for 3D flow, $\varepsilon_f \approx 2.6\times10^{-4}$, and the appropriate matrix interaction parameter for Hto, $G_0 = 6.1\times10^{-5}$ my$^{-½}$.

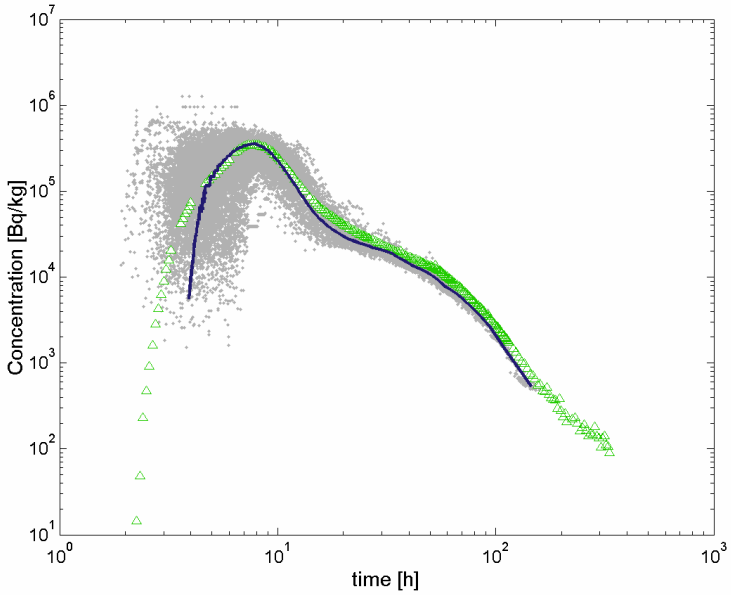

Figure 13 *Breakthrough concentration-time profile (BTC) for tritiated water (Hto). The simulated results are shown as a probability density map (composite of 100 realisations). Mean of simulated results is shown as a blue curve. Triangular markers indicate experimental data for the STT1b test.*

The estimated flow porosity is a calibration parameter based upon the experimental Hto breakthrough curve and therefore the data shown in Figure 13 cannot be taken as being indicative of agreement between experiment and simulation as these curves should always coincide.

As the injection nodes are placed within a regular grid, the linear distance from the injection node to the pumping node is only approximately 5 m and there is some small variation between runs. Owing to the stochastic nature of the simulations, the average path length taken by particles when travelling from the injection node to the pumping node also varies. The mean linear distance from the injection node to the pumping node, mean flowrate at the injection node, and mean path length for particle transport were:

Mean linear distance from injection to pumping node	5.1±0.1 m
Mean net flowrate at injection node	19± 2 ml/h
Mean path length for particle transport	9.24±0.6 m

Most of the injected particles follow a direct route from the injection node to the pumping node. Some particles, however, take a more indirect route and sample a much larger sub-region of the simulation volume.

The mean path length taken by particles from the injection node to the pumping node is roughly 80% longer than the linear distance. Owing to the regular structure of the channel grid, the particles generally must take a zigzag route when traversing the distance from the injection node to the pumping node.

The simulated mean net flowrate at the injection node is dependent upon the channel length and is therefore not directly comparable to the experiment. To ascertain whether the injection node flowrate (assumed to be equal to the mean flow expected at that distance from the recovery borehole) may influence the result, additional simulations were performed where the net flowrate criterion calculated by equation 20 was multiplied by a factor of 3. This means that potential injection nodes were accepted only if they had a net flowrate that was 3 times the expected average flowrate for spherical flow (±20%) at a distance of 5 m.

It was found that the mean arrival times estimated for 5%, 50%, and 95% of the injected tracer were less than those estimated using the initial injection node criterion. These differences, although statistically significant, are very difficult to discern in breakthrough concentration-time profiles (BTC plots) owing both to the spread of data and the log-log scaling of the plots. The simulations made with the original injection node-selection criterion were given the serial number *3DQ1*. The simulations made with the modified node-selection criterion were given the serial number *3DQ1b*. Comparison curves for the 3DQ1 and 3DQ1b simulations are given Appendix 2.

Using the same flow porosity, but different values for the matrix interaction parameter, G_0 allows for simulations of the various other sorbing and non-sorbing tracers. BTC plots for these other tracers are shown in Appendix 2 for the *3DQ1* simulation series. To summarise the results, the simulated breakthrough times for 5%, 50%, and 95% of the injected tracer have been calculated. These breakthrough times are referred to as t_{05}, t_{50}, and t_{95}. As the results are based upon 100 realisations for each tracer, the times estimated for t_{05}, t_{50}, and t_{95} are found to vary within a range. To give an idea of the variability of the results, the 5%, 50% (median), and 95% percentiles are given for each estimated breakthrough time. These results are given below (and also in Appendix 2):

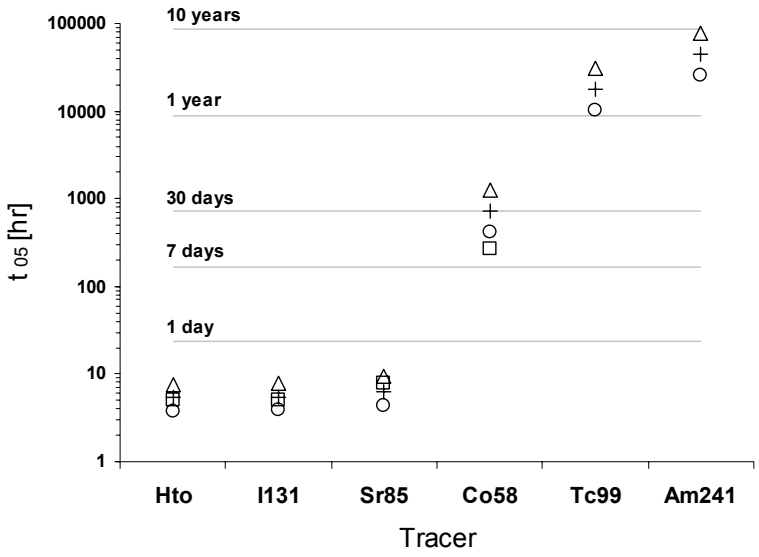

Figure 14 *Breakthrough times for 5% (t_{05}) of the injected tracer (3DQ1). 5% (circles), 50% (+ symbols), and 95% (triangles) percentile levels are shown for the simulated results. Experimental results (squares) are shown for Hto, ^{131}I, ^{85}Sr, and ^{58}Co.*

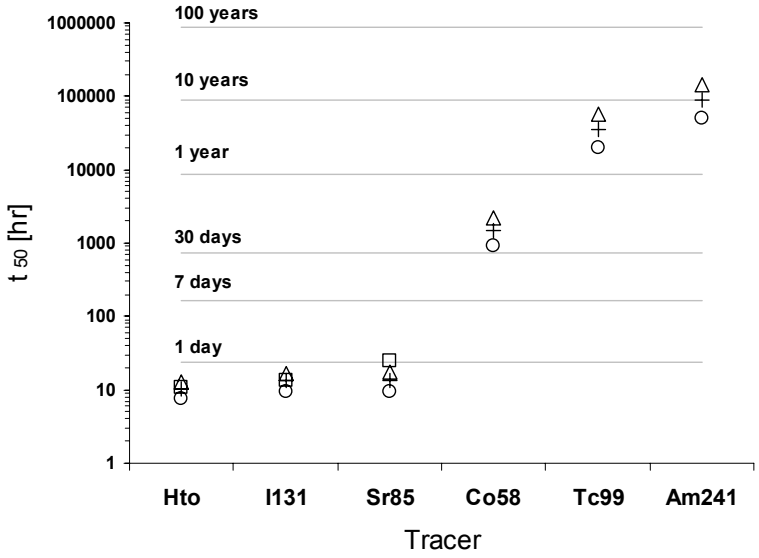

Figure 15 *Breakthrough times for 50% (t_{50}) of the injected tracer (3DQ1). 5% (circles), 50% (+ symbols), and 95% (triangles) percentile levels are shown for the simulated results. Experimental results (squares) are shown for Hto, ^{131}I, ^{85}Sr, and ^{58}Co.*

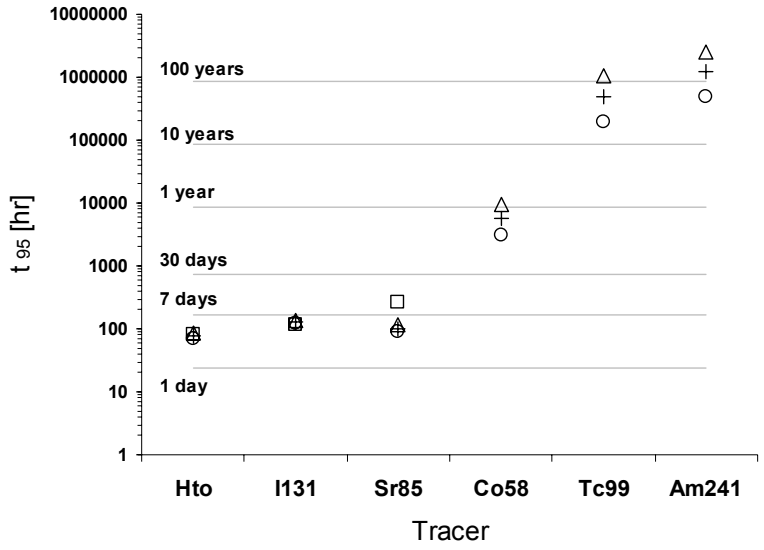

Figure 16 *Breakthrough times for 95% (t_{95}) of the injected tracer (3DQ1). 5% (circles), 50% (+ symbols), and 95% (triangles) percentile levels are shown for the simulated results. Experimental results (squares) are shown for Hto, ^{131}I, ^{85}Sr, and ^{58}Co.*

4.2 Simulations for a 2D Flow System

For the 2D flow system, the flow porosity was determined by approximately fitting the BTC for Hto to the experimental data in the same way as was done for the 3D flow system. As discussed previously, the channels in the plane of Feature A were given conductivities 50 times greater than those in the remaining rock volume in order to obtain preferential flow in Feature A.

For the transport calculations, injection nodes 5 m distant from the recovery section (in the plane of Feature A) were randomly selected during each realisation. If the net flowrate through the selected node corresponded to the average mean flowrate (±20%) that would be expected for 2D radial flow at a distance of 5 metres then it was used for the simulation. If the net flowrate through the selected node lay outside this window, then the node was rejected and another node was tested. The average flow that would be expected at a distance of 5 m from the pumping node was estimated with the formula:

$$F_m \approx Z\left(\frac{q}{2\pi r}\right) \tag{21}$$

Where Z is the channel length, q is the pumping flowrate, and r is the distance from the injection node to the pumping node (5 m). Equation 21 is based upon the premise that each node distributed on the perimeter of a virtual disk of radius r, subtends an arc length roughly corresponding to the distance Z. The average flowrate that would be expected through the node is then equal to the radial water flux multiplied by the arc length subtended by an individual node. For a channel length of 0.5 m, a transport distance of 5 m, and a pumping flowrate of 0.401 l/min, the expected flowrate (F_m) is 382 ml/h.

As the Feature A fracture was assumed to have different properties to the rest of the rock volume, it was necessary for the injection nodes to lie in the plane of Feature A. The locations of a number of injection nodes used for the simulations are illustrated in Figure 17 below:

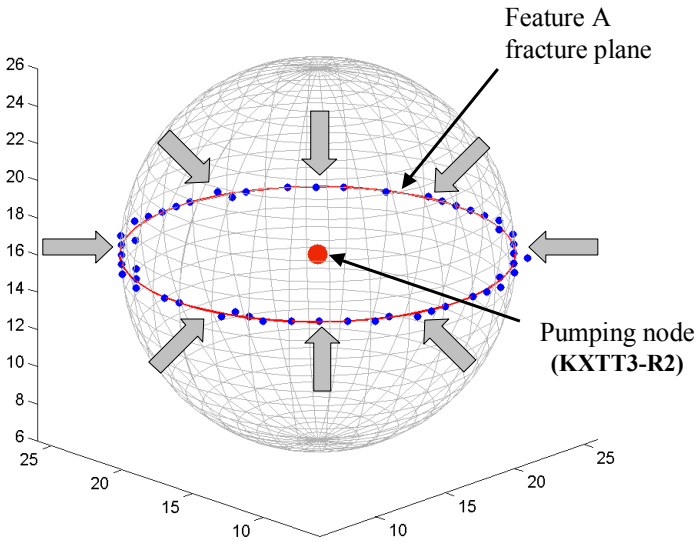

Figure 17 *Visualisation of injection locations for 2D simulations where the Feature A channels have conductivities 50 times that of channels in the remaining rock volume. Injection locations are visualised as blue markers on the disk perimeter.*

Figure 18 below shows the results of 100 realisations for Hto transport using the estimated flow porosity for 2D flow, and the appropriate matrix interaction parameter for Hto, $G_0 = 6.1\times10^{-5}$ $my^{-½}$.

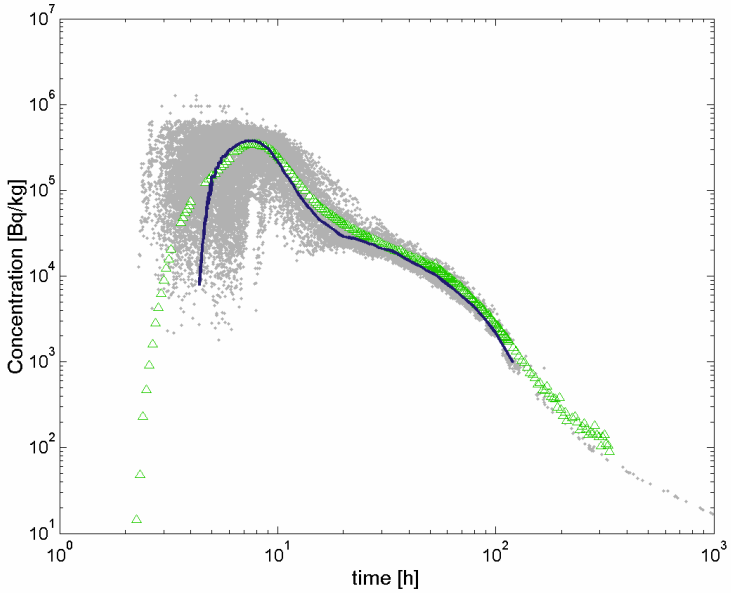

Figure 18 *Breakthrough concentration-time profile (BTC) for tritiated water (Hto). The simulated results are shown as a probability density map (composite of 100 realisations). Mean of simulated results is shown as a blue curve. Triangular markers indicate experimental data for the STT1b test.*

As discussed previously for the 3D case, the estimated flow porosity is a calibration parameter based upon the experimental Hto breakthrough curve and therefore the data shown in Figure 18 cannot be taken as being indicative of agreement between experiment and simulation. The known flowrate and water residence time (estimated from the calibration simulations) allows us to calculate an average fracture aperture of 2 mm for the 2D scenario.

The results for non-sorbing tracers are, for all practical purposes, identical in the 2D and 3D simulations.

The mean linear distance from the injection node to the pumping node, the mean flowrate at the injection node, and the mean path length for particle transport for these simulations were:

Mean linear distance from injection to pumping node	5.0±0.1 m
Mean net flowrate at injection node	380± 40 ml/h
Mean path length for particle transport	7.57± 0.61 m

As found previously, most of the injected particles follow a direct route from the injection node to the pumping node. Some particles, however, take a more indirect route and sample a much larger sub-region of the simulation volume.

In the 2D simulations only a very small fraction of the nodes visited by particles were outside of the plane of Feature A and the simulations are therefore considered to be representative of pure 2D transport. Similarly to what was observed for the 3D simulations, the mean path length taken by particles from the injection node to the pumping node is roughly 50% longer than the linear distance.

As discussed previously in the context of the 3D simulations, the simulated mean net flowrate at the injection node is dependent upon the channel length and is therefore not directly comparable to the experiment. To ascertain whether the injection node flowrate (assumed to be equal to the mean flow expected at that distance from the recovery borehole) may influence the result, additional simulations were performed where the net flowrate criterion calculated by equation 21 was multiplied by a factor of 2. This means that potential injection nodes were accepted only if they had a net flowrate that was 2 times the expected average flowrate for spherical flow (±20%) at a distance of 5 m. The reason why a value of 2 was chosen here rather than the factor 3 used in the corresponding 3D simulations was that it was generally not possible to find a sufficient number of injection nodes to make a comparison. This is primarily due to the smaller number of possible injection nodes existing in the 2D case.

It was found that the mean arrival times estimated for 5%, 50%, and 95% of the injected tracer were less than those estimated using the initial injection node criterion. These differences, although statistically significant, are very difficult to discern in breakthrough concentration-time profiles (BTC plots) owing both to the spread of data and the log-log scaling of the plots. The simulations made with the original injection node-selection criterion were given the serial number *2DQ1*. The simulations made with the modified node-selection criterion were given the serial number *2DQ1b*. Comparison curves for the 2DQ1 and 2DQ1b simulations are given Appendix 2.

Using the same flow porosity, but different values for the matrix interaction parameter, G_0 allows for simulations of the various other sorbing and non-sorbing tracers. These realisations were given the serial number *2DQ1*. BTC plots for these other tracers are shown in Appendix 2. To summarise the results, the simulated breakthrough times t_{05}, t_{50}, and t_{95} were calculated as was done for the 3D simulations. To give an idea of the variability of the results, the 5%, 50% (median), and 95% percentiles are given for each estimated breakthrough time. These are based upon the results of 100 realisations and are given below as well as in Appendix 2:

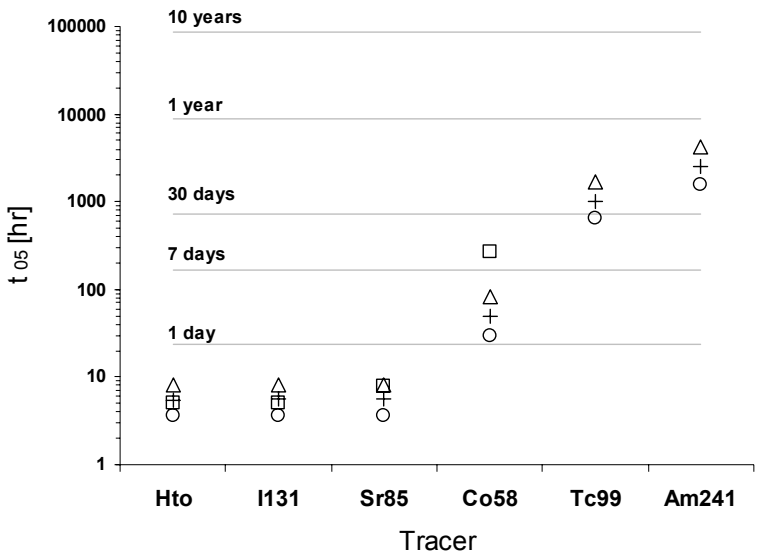

Figure 19 *Breakthrough times for 5% (t_{05}) of the injected tracer (2DQ1). 5% (circles), 50% (+ symbols), and 95% (triangles) percentile levels are shown for the simulated results. Experimental results (squares) are shown for Hto, ^{131}I, ^{85}Sr, and ^{58}Co.*

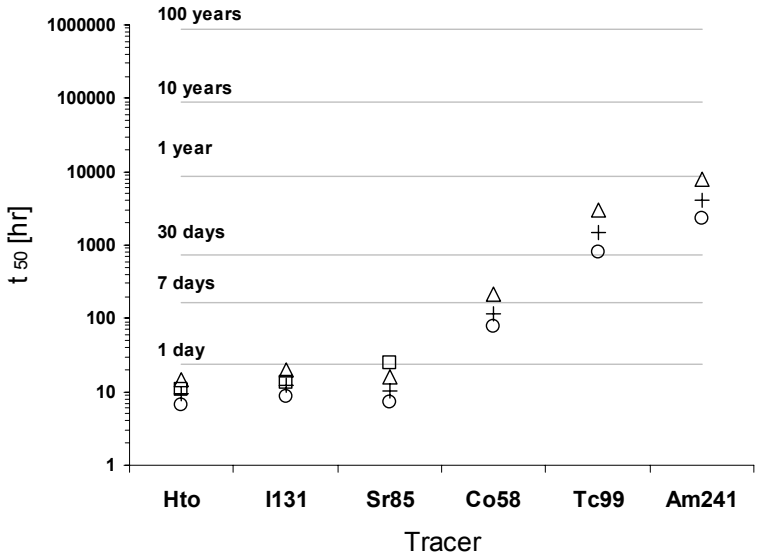

Figure 20 *Breakthrough times for 50% (t_{50}) of the injected tracer (2DQ1). 5% (circles), 50% (+ symbols), and 95% (triangles) percentile levels are shown for the simulated results. Experimental results (squares) are shown for Hto, ^{131}I, ^{85}Sr, and ^{58}Co.*

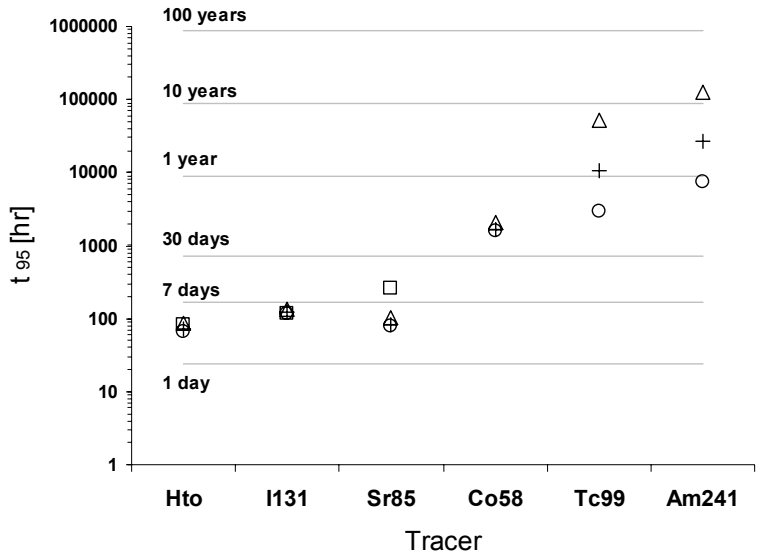

Figure 21 *Breakthrough times for 95% (t_{95}) of the injected tracer (2DQ1). 5% (circles), 50% (+ symbols), and 95% (triangles) percentile levels are shown for the simulated results. Experimental results (squares) are shown for Hto, ^{131}I, ^{85}Sr, and ^{58}Co.*

5 Task 6B Simulations

The hydraulic boundary conditions for Task 6B were identical to Task 6A with the exception that the pumping flowrate in KXTT3-R2 was 1000 times smaller than that used for the actual STT1b tracer tests. The pumping flowrate used for the simulations was thus on the order of 210 l/year (4.01×10^{-4} l/min). In addition to the simulation of a Dirac pulse injection boundary condition, a constant release injection of 1 MBq/y was also requested in the task specification.

5.1 Simulations for a 3D Flow System

The BTC plots for both Dirac pulse and constant injection boundary conditions are given in Appendix 3 as well as calculated maximum release rates for each of the tracers. The 3D simulations using the reduced pumping flowrate specified for Task 6B were given the serial number *3DQ2*. The recovery times t_{05}, t_{50}, and t_{95} and their corresponding 5%, 50% (median), and 95% percentiles are given in the figures below. These are also given in Appendix 3 along with a comparison of tracer arrival times for Task 6A and Task 6B simulations.

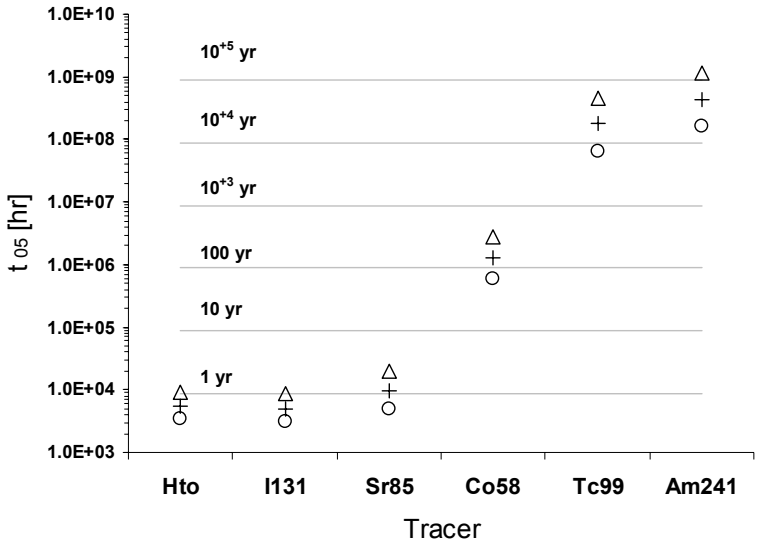

Figure 22 *Breakthrough times for 5% (t_{05}) of the Dirac pulse injected tracer (3DQ2). 5% (circles), 50% (+ symbols), and 95% (triangles) percentile levels are shown for the simulated results.*

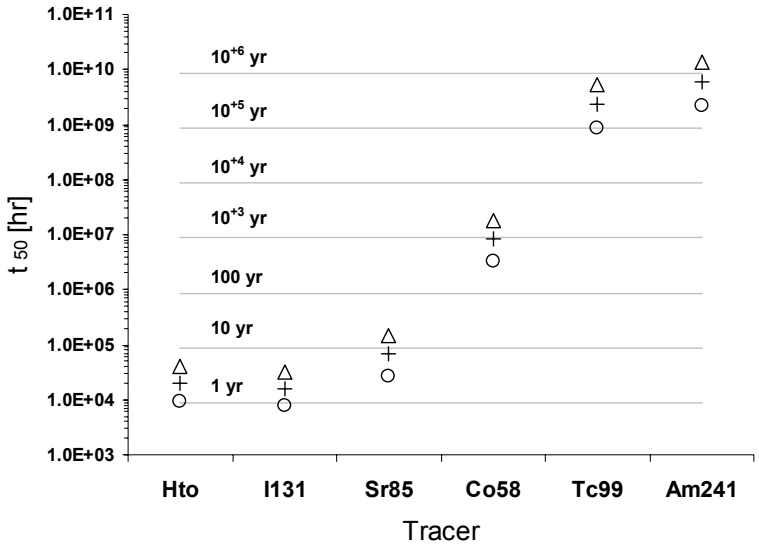

Figure 23 *Breakthrough times for 50% (t_{50}) of the Dirac pulse injected tracer (3DQ2). 5% (circles), 50% (+ symbols), and 95% (triangles) percentile levels are shown for the simulated results.*

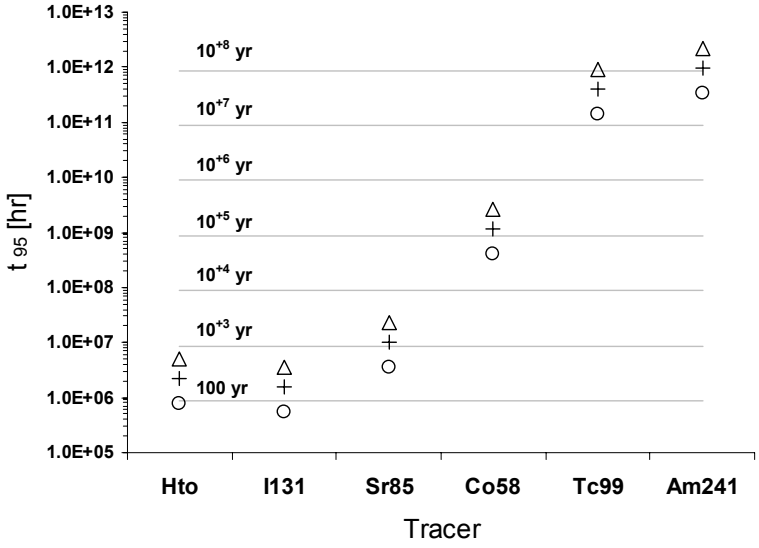

Figure 24 *Breakthrough times for 95% (t_{95}) of the Dirac pulse injected tracer (3DQ2). 5% (circles), 50% (+ symbols), and 95% (triangles) percentile levels are shown for the simulated results.*

Figure 25 and Figure 26 below illustrate the differences between Task 6A (*3DQ1*) and Task 6B (*3DQ2*) results for tritiated water (Hto) and ^{241}Am.

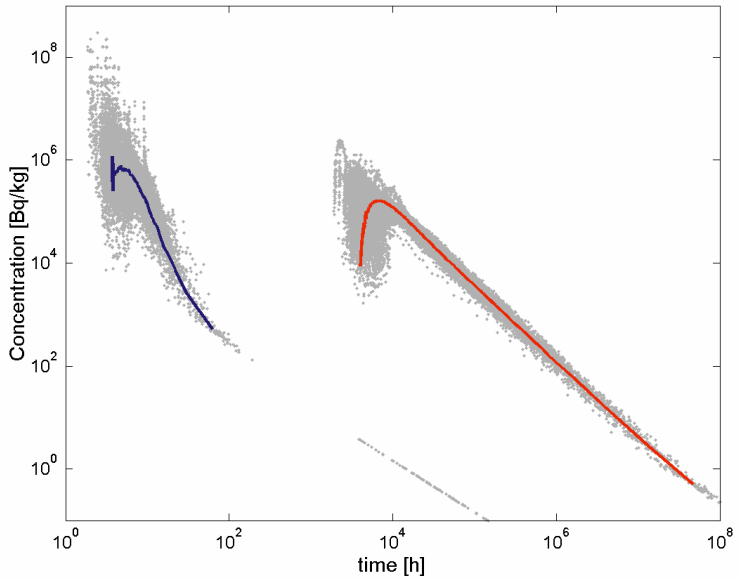

Figure 25 *Comparison of breakthrough concentration-time profiles for Hto Dirac pulse. The blue curve and associated probability density map show simulation data for Task 6A (3DQ1). The red curve and associated probability density map indicate data for Task 6B (3DQ2).*

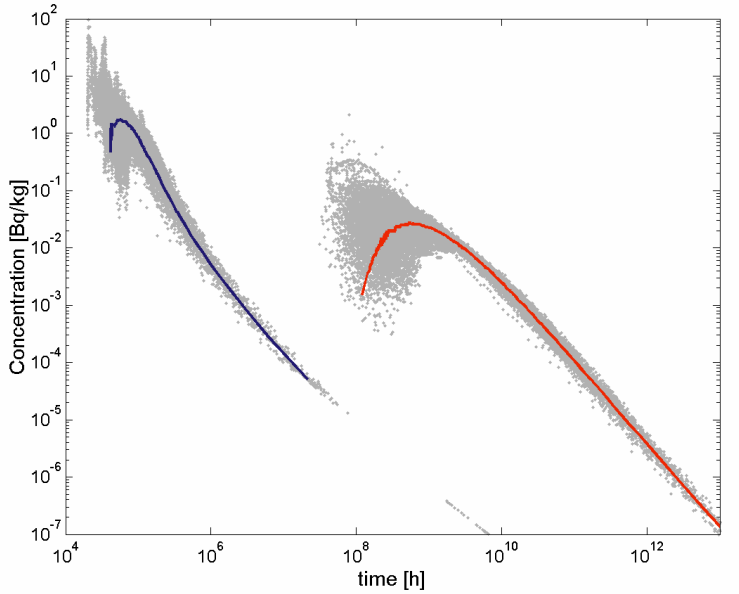

Figure 26 *Comparison of breakthrough concentration-time profiles for ^{241}Am Dirac pulse. The blue curve and associated probability density map show simulation data for Task 6A (3DQ1). The red curve and associated probability density map indicate data for Task 6B (3DQ2).*

5.2 Simulations for a 2D Flow System

The BTC plots for both Dirac pulse and constant injection boundary conditions are given in Appendix 3 as well as calculated maximum release rates for each of the tracers. The 2D simulations using the reduced pumping flowrate specified for Task 6B were given the serial number *2DQ2*. The recovery times t_{05}, t_{50}, and t_{95} and their corresponding 5%, 50% (median), and 95% percentiles given in the figures below. These are also given in Appendix 3 along with a comparison of tracer arrival times for Task 6A and Task 6B simulations.

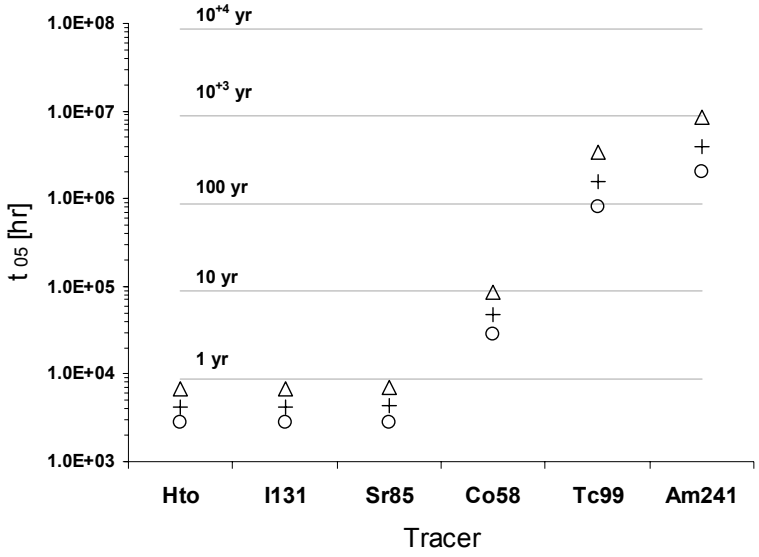

Figure 27 *Breakthrough times for 5% (t_{05}) of the Dirac pulse injected tracer (2DQ2). 5% (circles), 50% (+ symbols), and 95% (triangles) percentile levels are shown for the simulated results.*

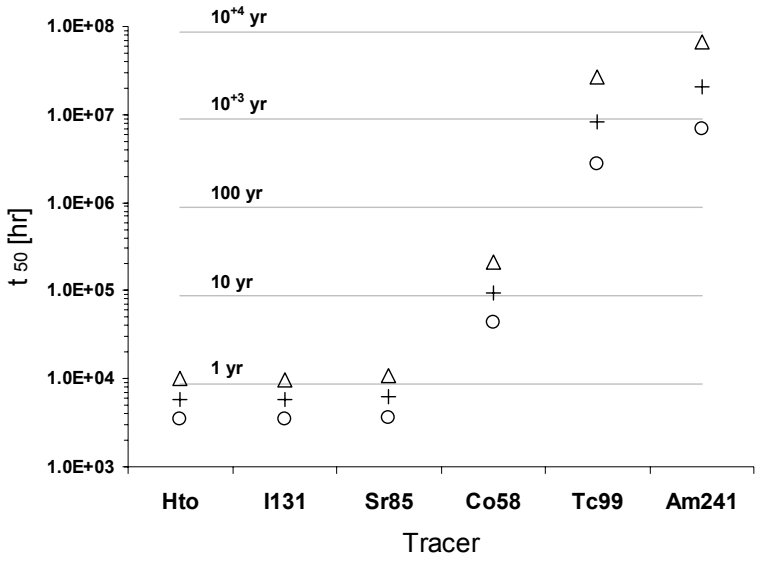

Figure 28 *Breakthrough times for 50% (t_{50}) of the Dirac pulse injected tracer (2DQ2). 5% (circles), 50% (+ symbols), and 95% (triangles) percentile levels are shown for the simulated results.*

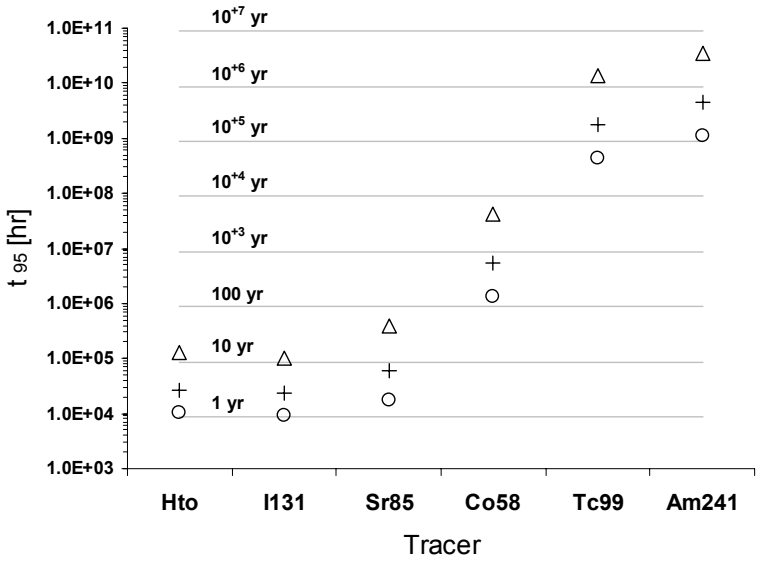

Figure 29 *Breakthrough times for 95% (t_{95}) of the Dirac pulse injected tracer (2DQ2). 5% (circles), 50% (+ symbols), and 95% (triangles) percentile levels are shown for the simulated results.*

Figure 30 and Figure 31 below illustrate the differences between Task 6A (*2DQ1*) and Task 6B (*2DQ2*) simulation results for tritiated water (Hto) and ^{241}Am.

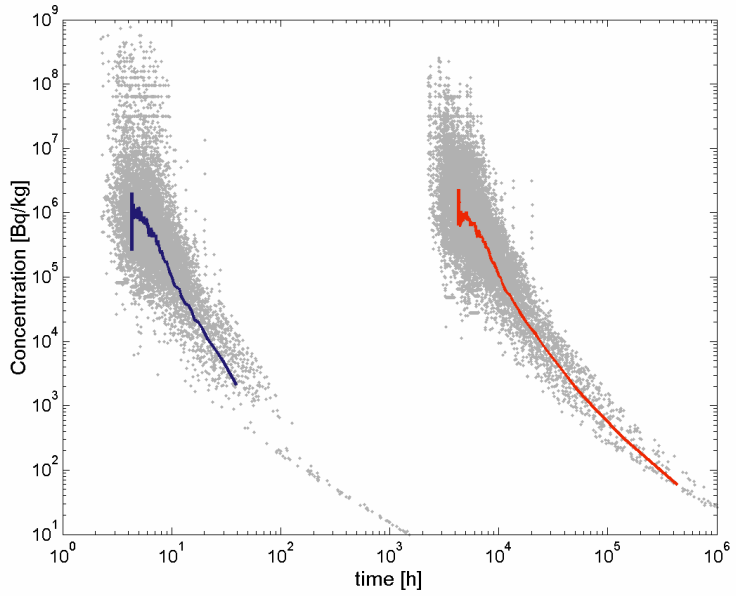

Figure 30 *Comparison of breakthrough concentration-time profiles for Hto Dirac pulse. The blue curve and associated probability density map show simulation results for Task 6A (2DQ1). The red curve and associated probability density map indicate results for Task 6B (2DQ2).*

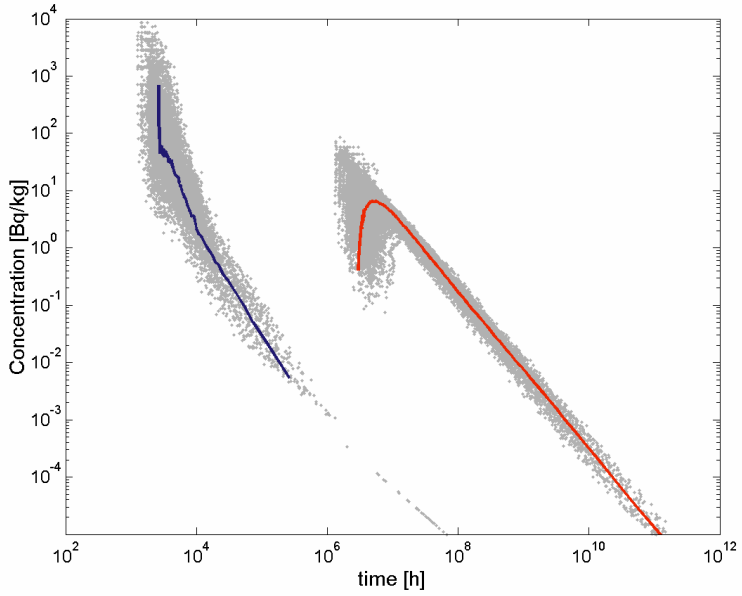

Figure 31 *Comparison of breakthrough concentration-time profiles for ^{241}Am Dirac pulse. The blue curve and associated probability density map show simulation results for Task 6A (2DQ1). The red curve and associated probability density map indicate results for Task 6B (2DQ2).*

6 Task 6B2 Simulations

In the Task 6B2 simulations, a scenario was studied in which the transmissivity of channels lying in the plane of Feature A were varied relative to the assumed mean background transmissivity. The same flow porosity was used as for the 3D Task 6A and 6B studies. The specific FWS and FWS per channel were the same as those used previously in the Task 6A and 6B studies.

Based upon the results of various hydraulic tests, the transmissivity of Feature A has been estimated to be typically in the range of 8×10^{-9} to 4×10^{-7} m^2/s. This is roughly 10 to 40 times the mean transmissivity of the background fractures in the surrounding rock volume. As the actual transmissivity of Feature A is quite uncertain, a number of case studies were carried out to observe the sensitivity of the model predictions to this uncertainty.

For the cases modelled previously (2D flow structure), it was assumed that Feature A had a transmissivity that was much larger than the surrounding rock. In the Task 6B2 simulations, the transmissivity in Feature A was assumed in different case studies to be 10, 20, and 40 times the background transmissivity value. In the present context, the mean value of the background transmissivity will be referred to as the "reference transmissivity".

In CHAN3D, individual channel volumes are added to obtain a total volume which, when divided by the conceptual simulation volume, gives the total flow porosity for the system being modelled. The volume of a channel is equal to the product of half the flow-wetted surface per channel and the channel aperture. As the FWS per channel is assumed to be constant, channels with different conductances have different apertures.

Using a cubic law relation between fracture aperture and conductance, the average fracture apertures for the channels lying within Feature A and those lying outside the plane of Feature A were calculated for the assumed total flow porosity. The total flow porosity in the system is made up of a contribution from the channels in the plane of Feature A and those lying in the remainder of the rock volume.

For channels lying in the plane of Feature A with transmissivity 10 times that of the reference transmissivity, the cubic law relation gives channel apertures that are $10^{1/3} \approx 2.15$ times larger than the background channel apertures. For 20 times the background transmissivity, the average channel aperture in Feature A is 2.7 times greater; For 40 times greater transmissivity, the channels should be 3.42 times larger.

For the assumed flow porosity ($\varepsilon_f = 2.6\times10^{-4}$), a FWS equal to 7 m^2/m^3, a channel length of 0.5 m and a cubic simulation volume of 15 m^3, the channel apertures are as given in Table 2 below:

Table 2 Average fracture apertures (mm) calculated for channels lying within Feature A and for channels in the rock volume outside of the plane of Feature A.

Feature A transmissivity	Background Fractures	Feature A
10× background value	0.0632	0.136
20× background value	0.0625	0.170
40× background value	0.0616	0.211

In addition to the simulations where flow and transport were allowed to occur outside the plane of Feature A within background channels, a series of simulations were also made without any background channels. In these simulations, the channels outside the plane of Feature A were assigned zero transmissivity and volume. For the channels lying in the plane of Feature A, however, the same transmissivities and average fracture apertures were used as in Table 2 above.

It should be noted that, although the ratio of channel apertures will always be the same, the absolute value of the channel apertures will depend upon the assumed flow porosity and the shape of the simulation volume upon which the definition of flow porosity is based. The channel apertures as given in Table 2 cannot therefore be compared with "real" fracture apertures without more detailed information about the actual flow porosity for the simulated flow geometry. The flow porosity used for the Task 6A and 6B simulations was calibrated to give the same breakthrough characteristics as a non-sorbing tracer in the field experiments. For the flow geometry used in Task 6B2, this flow porosity may not be appropriate for the reasons outlined above.

6.1 Simulations of Solute Transport with Background Fracturing

The simulations differed from those carried out in Task 6A and 6B in respect of the fact that a deterministic Feature A was introduced. For the 3D cases modelled previously, it was assumed that Feature A had a transmissivity that was indistinguishable from the surrounding rock. In the Task 6B2 simulations, the transmissivity in Feature A was assumed in different case studies to be 10, 20, and 40 times the background transmissivity value.

The routes for particle transport from the injection location to the recovery plane are plotted in Figure 32 below for a typical simulation:

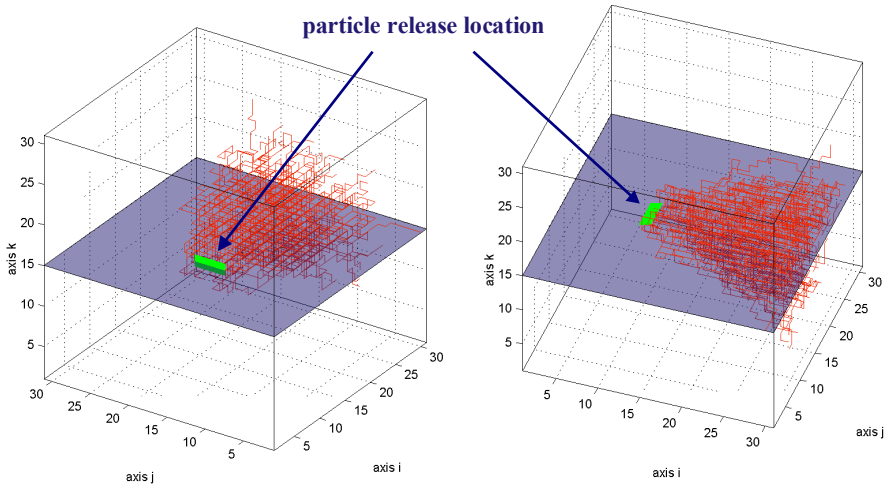

Figure 32 *Visualisation of the particle capture field in the 3D simulations seen from two different perspectives. The pathways taken through the channel network by 500 particles (out of 5000 injected) is plotted in red. The green marker in the figure indicates the tracer injection location. The channels lying in the plane of Feature A have a transmissivity equal to 10 times the reference transmissivity.*

Figure 33 below, shows results obtained for a Dirac pulse injection of tritiated water (Hto) for different Feature A transmissivities:

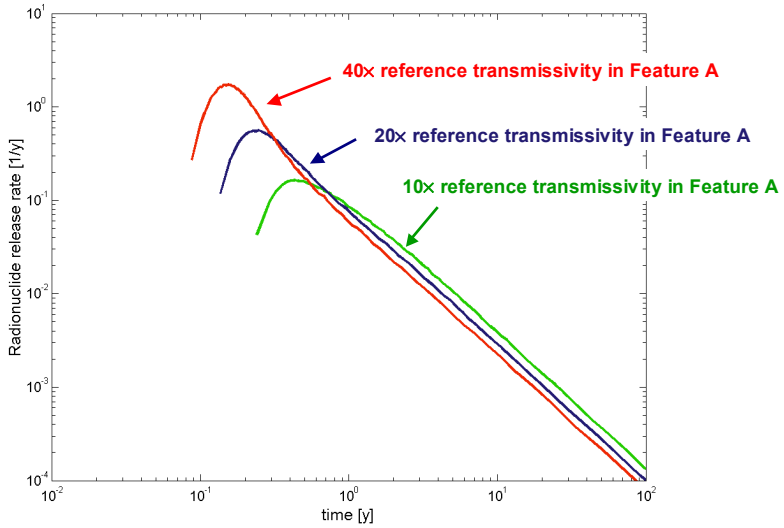

Figure 33 *Breakthrough data for tritiated water (Hto). The breakthrough profiles are given as a flux [1/y] rather than concentrations. Owing to the differing flowrates obtained with different Feature A transmissivities, this facilitates comparison between the different cases.*

Figure 34 below, shows results obtained for a Dirac pulse injection of ^{241}Am for different Feature A transmissivities:

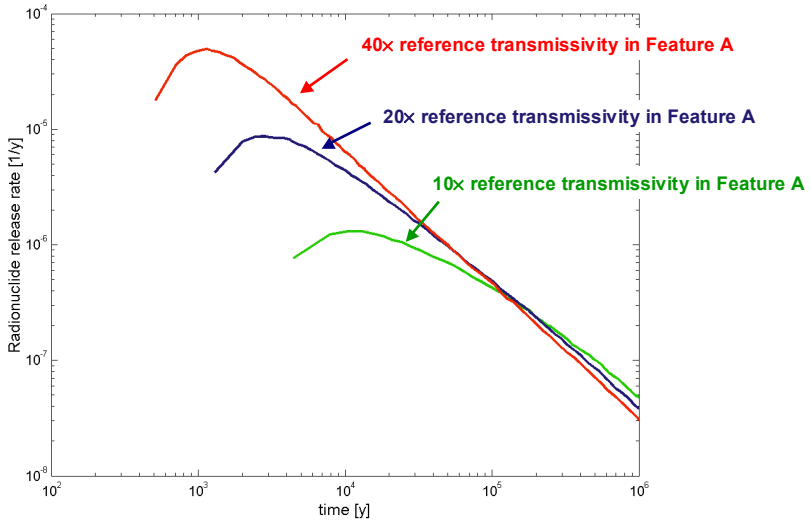

Figure 34 *Breakthrough data for ^{241}Am. The breakthrough profiles are given as a flux [1/y] rather than concentrations. Owing to the differing flowrates obtained with different Feature A transmissivities, this facilitates comparison between the different cases.*

The recovery times t_{05}, t_{50}, and t_{95} and their corresponding 5%, 50% (median), and 95% percentiles are given in Appendix 4 for each of the cases studied.

One of the most important results of the Task 6B2 simulations is the demonstration that flow porosity has little or no influence on the transport of strongly interacting tracers over the distances and timescales considered. For non-sorbing tracers, however, the flow porosity is very important in determining the tracer residence time. This is illustrated in Figure 35 (Hto) and Figure 36 (^{241}Am) below:

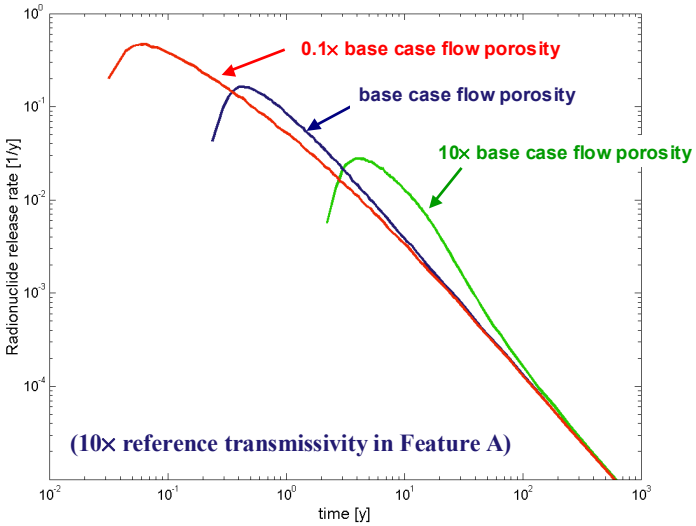

Figure 35 *Breakthrough flux data for tritiated water (Hto). In this case, the transmissivity of Feature A was assumed to be 10 times the background transmissivity and only the flow porosity was altered. As the transmissivity of the system has not been altered, the total flowrate is therefore the same in each case.*

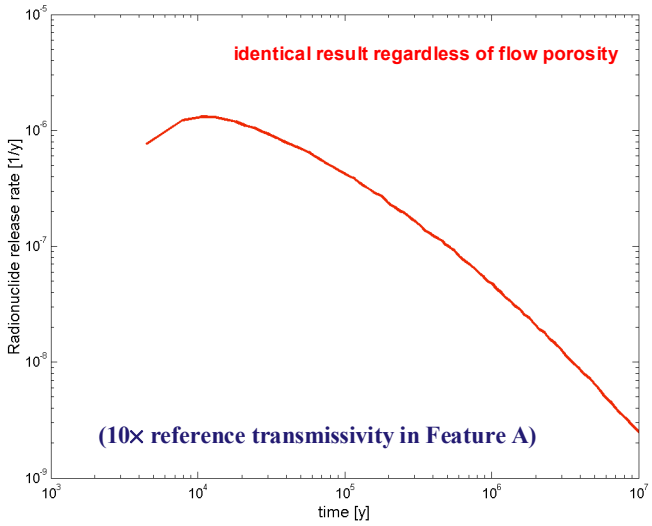

Figure 36 *Breakthrough flux data for ^{241}Am. In this case, the transmissivity of Feature A was assumed to be 10 times the background transmissivity and only the flow porosity was altered. As the transmissivity of the system has not been altered, the total flowrate is therefore the same in each case. The results were identical for each of the 3 cases; 0.1, 1.0, and 10.0 times the base case flow porosity.*

6.2 Simulations of Solute Transport in the Absence of Background Fracturing

Similarly to the previous case studies, the transmissivity in Feature A was assumed in different case studies to be 10, 20, and 40 times the reference transmissivity value. In this case however, the transmissivity of channels outside the plane of Feature A were set to zero, thus forcing the fluid flow and tracer transport to occur purely in the plane of Feature A. The channels in the plane of Feature A, however, have the same aperture and volume as in the 3D cases described in the previous section.

The route for particle transport from the injection location and the recovery plane are plotted in Figure 37 below:

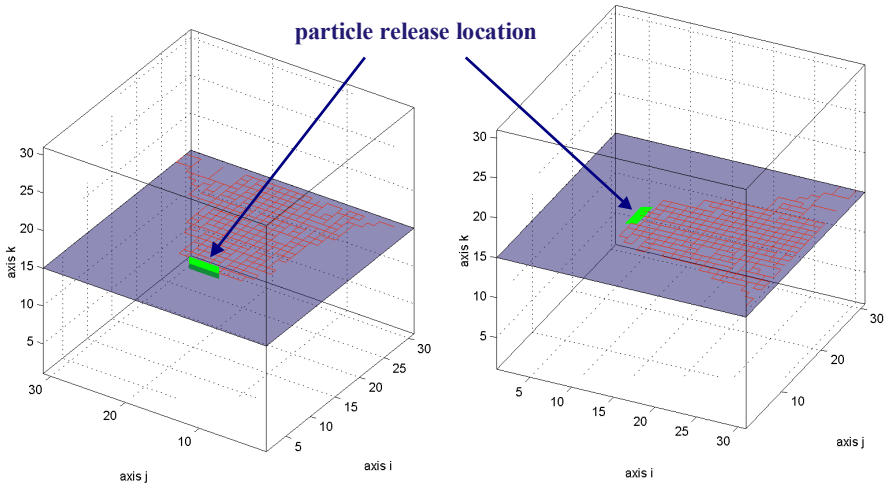

Figure 37 *Visualisation of the particle capture field in the 2D simulations seen from two different perspectives. The pathways taken through the channel network by 500 particles (out of 5000 injected) is plotted in red. The green marker in the figure indicates the tracer injection location.*

Figure 38 below, shows results obtained for a Dirac pulse injection of tritiated water (Hto) for different Feature A transmissivities:

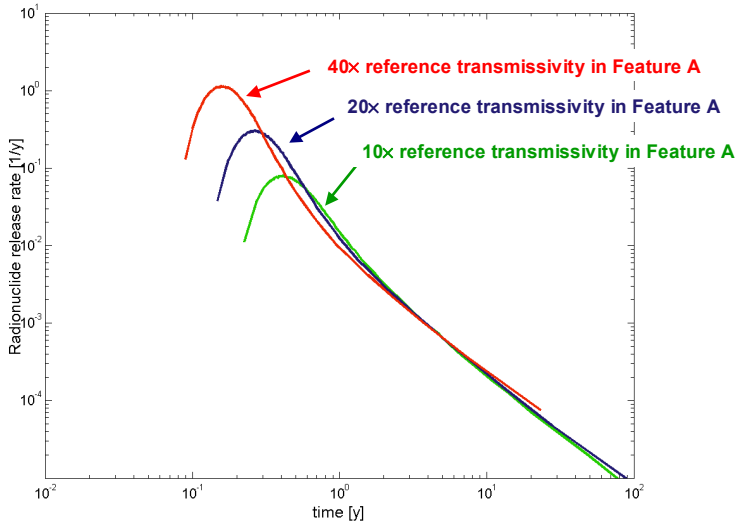

Figure 38 *Breakthrough data for tritiated water (Hto). The breakthrough profiles are given as a flux [1/y] rather than concentrations. Owing to the differing flowrates obtained with different Feature A transmissivities, this facilitates comparison between the different cases.*

Figure 47 below, shows results obtained for a Dirac pulse injection of ^{241}Am for different Feature A transmissivities:

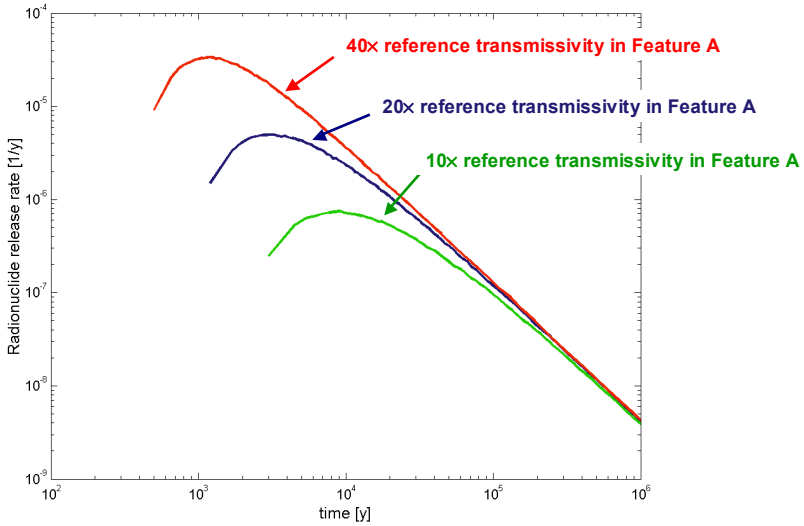

Figure 39 *Breakthrough data for ^{241}Am. The breakthrough profiles are given as a flux [1/y] rather than concentrations. Owing to the differing flowrates obtained with different Feature A transmissivities, this facilitates comparison between the different cases.*

The recovery times t_{05}, t_{50}, and t_{95} and their corresponding 5%, 50% (median), and 95% percentiles are given in Appendix 4 for each of the cases studied.

As discussed already in light of the simulations including background channels, one of the most important results of the Task 6B2 simulations is the demonstration that flow porosity has little or no influence on the transport of strongly interacting tracers over the distances and timescales considered. For non-sorbing tracers, however, the flow porosity is very important in determining the tracer residence time. This is illustrated in Figure 40 (Hto) and Figure 41 (^{241}Am) below:

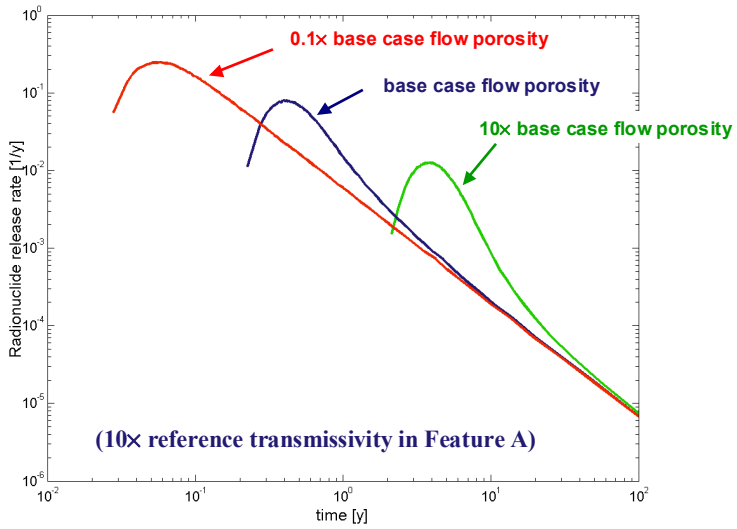

Figure 40 *Breakthrough flux data for tritiated water (Hto). In this case, the transmissivity of Feature A was assumed to be 10 times the background transmissivity and only the flow porosity was altered. As the transmissivity of the system has not been altered, the total flowrate is therefore the same in each case.*

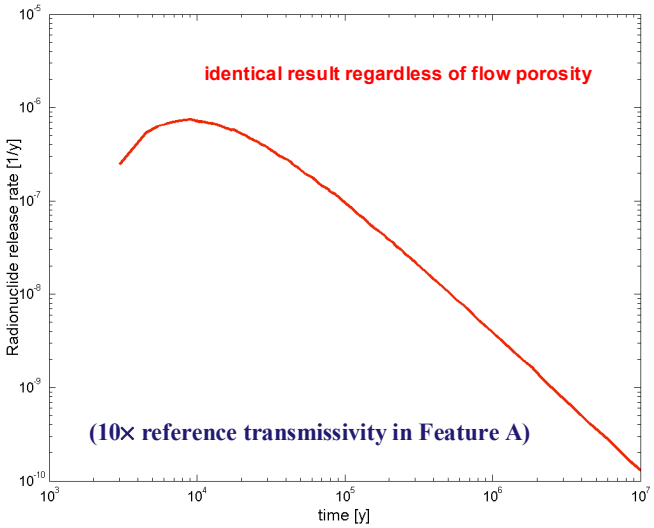

Figure 41 *Breakthrough flux data for ^{241}Am. In this case, the transmissivity of Feature A was assumed to be 10 times the background transmissivity and only the flow porosity was altered. As the transmissivity of the system has not been altered, the total flowrate is therefore the same in each case. The results were identical for each of the 3 cases 0.1, 1.0, and 10.0 times the base case flow porosity.*

7 Discussion

7.1 Transport through a 2D or 3D flow structure?

The impact of using a 2D or 3D flow description is determined by the extent of the interaction with the rock matrix. As discussed previously, the value of the quotient *FWS/q* (and FWS_{tot}/Q) is much higher for the 3D flow structure. So, for non-sorbing or slightly sorbing tracers the effect of the flow structure (2D or 3D) would be small. On the other hand, for strongly sorbing tracers the flow structure would have a very large impact.

In our simulations, owing to the low level of interaction with the rock matrix, there was very little observable difference between the 2D and 3D simulation results for the non-sorbing (^{131}I) or poorly sorbing tracers (^{85}Sr). Figure 42 below shows breakthrough concentration-time profiles for Hto. As indicated in the figure, the results are essentially identical for both the 2D and 3D flow assumptions:

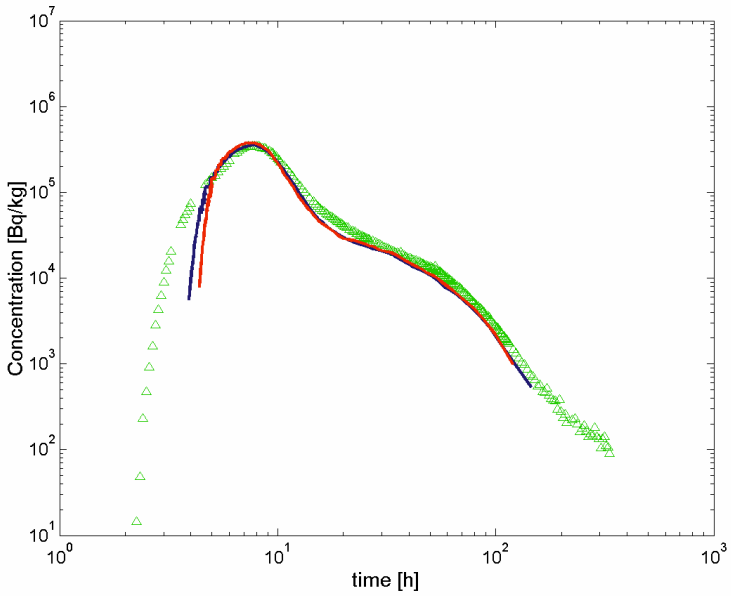

Figure 42 *Breakthrough concentration-time profiles for tritiated water (Hto). The blue curve shows data for 3D simulations (3DQ1). The red curve indicates data for 2D simulations (2DQ1). Triangular, green markers indicate experimental data for the STT1b test.*

There is a slight discrepancy in the arrival times for the non-sorbing tracers, but this is likely to be related to the different flow porosities defined for 2D and 3D cases. The flow porosity was determined by visually matching the simulated breakthrough curves for the Hto tracer with the experimentally measured breakthrough data. For this reason we conclude that the mismatch between the recovery times for ^{131}I, and ^{85}Sr relate to small inaccuracies in the calibration procedure used. The recovery times for mildly- (^{58}Co) and strongly sorbing tracers (^{99}Tc, ^{241}Am), on the other hand, differ by a factor of 10-30 when comparing the 2D and 3D simulations. This discrepancy may have a critical impact when the transport of radionuclides is modelled. For certain radionuclides, this

difference may mean the difference between them having- and not having sufficient time to decay to low levels of activity. Figure 43 below shows breakthrough concentration-time profiles for ^{58}Co where the impact of the 2D and 3D flow assumption is clearly apparent:

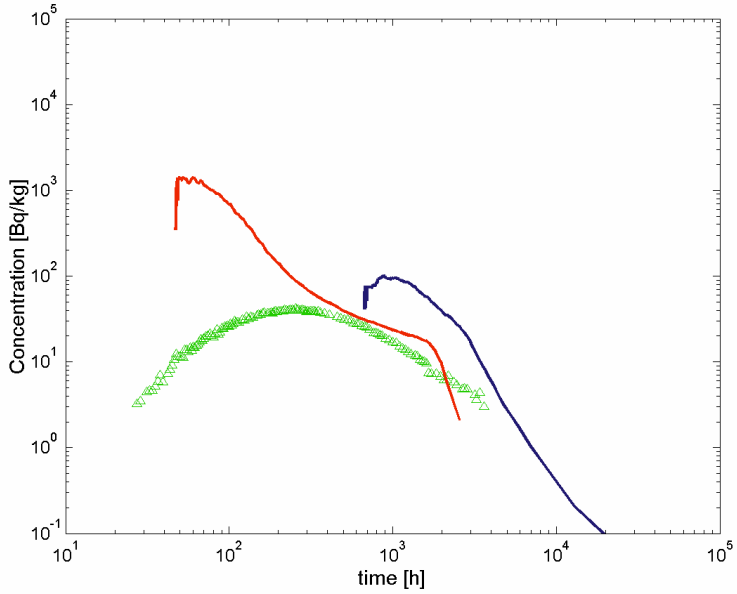

Figure 43 *Breakthrough concentration-time profile for ^{58}Co. The blue curve shows data for 3D simulations (3DQ1). The red curve indicates data for 2D simulations (2DQ1). Triangular, green markers indicate experimental data for the STT1b test.*

It is not possible, based upon the tracers modelled to conclude whether the system is best represented as an essentially 3D structure or a 2D fracture plane. The simulations for the non-sorbing or weakly sorbing tracers give a reasonable match to the experimental data for both the 2D and 3D scenarios. The shape of the breakthrough curves for ^{131}I, and ^{85}Sr (both experimental and simulated) are dominated strongly by the shape of the injection concentration-time history and do not give any clues as to whether the modelled structures match the true flow structure.

The shape of the experimentally measured breakthrough curve for ^{58}Co, however, indicates that neither the 2D or 3D flow systems as modelled, give results that are entirely consistent with the experimental data. It would appear from the simulations for ^{58}Co that the simply connected 2D and 3D structures used for these simulations do not exactly capture the fundamental nature of the flow-path structures that may exist in the system. Another reason why the simulated results for both the 2D and the 3D simulations are not consistent with the experimental data is the possibility that the sorption processes for ^{58}Co are to some extent, non-linear and partially irreversible. Another alternative is that the sorption is linear although kinetically hindered (Winberg et al., 2000).

Carbol and Engkvist (1997) suggest in their discussion, however, that Co exhibits sorption behaviour that is only weakly influenced by radionuclide concentration (i.e., the sorption of Co is relatively linear). It would therefore seem less likely that the shape of the ^{58}Co breakthrough curve is the result of a non-linear sorption process.

Almost 100% recovery was obtained for the tracers Hto, ^{131}I, and ^{85}Sr in the STT1b experiment. For ^{58}Co, however, only about 30% of the injected tracer was recovered and it is possible that a certain amount of the tracer was mineralised in the form of $Co(OH)_2$ precipitate (Carbol and Engkvist, 1997). This is an effect that the model does not consider. From the peaked shape of the ^{58}Co breakthrough curve, it appears that the main Co pulse has indeed broken through and the recovery time calculated based upon the injected mass of ^{58}Co probably does not reflect the true breakthrough time of the mobile fraction of the injected Co tracer.

Regarding the average fracture apertures required to match the collection flow rate and the arrival time it is found that a large aperture is required for the 2D flow structure. Using the estimated water residence time (6.1 h) and the recovery flow of 0.40 l/min a fracture of about 2 mm is required for the 2D flow structure. This average fracture aperture appears to be much larger than what is reasonable to expect. On the other hand, when the average fracture aperture is calculated assuming a 3D flow structure a value of about 0.07 mm is obtained. This is a much more reasonable value taking into account the values of fracture aperture observed in the field at these depths. This would indicate that the flow structure in the experiment STT1b is more likely to be 3D in nature.

That the 3D flow structure is a better representation of the TRUE-1 field is also supported by the results obtained by Neretnieks and Moreno in the analysis of the STT1 experiment (Neretnieks and Moreno, 2003). They predicted the tracer tests with sorbing tracers (Cs, Rb and Ba) using only independent data and found a better agreement when the 3D flow structure is used. When a 2D flow structure was simulated, they found that the quotient FWS/q has to be increased by a factor about 30 to obtain a reasonable fit to the experimental data.

If the 2D flow structure were a more accurate depiction of the actual flow system, we would expect that at least 50% or more of the injected ^{99}Tc would have been transported to the recovery section within a year. The fact that no ^{99}Tc was detected in the recovery section (during the experiment) is possible evidence that the tracers encounter a *FWS/q* ratio larger than the 2D flow scenario can account for. For the 3D flow structure, the quotient FWS/q is 23 times higher than that for the 2D scenario. Moreno (2001) also noted this in the Task 4E and 4F evaluation where the matrix interaction parameter needed to be about 30 times larger in order to explain the observed retardation in the experimental data if a 2D flow system was used.

For the 2D flow structure to be a good representation of the flow patterns found in the experiments, it is required to increase the product $D_e K_d$ (product of matrix effective diffusivity and matrix sorption coefficient) by a factor of 900 in the simulation model. An underestimation of the effective surface sorption coefficient (K_a) may also account for the discrepancy if a large amount of fine fault gouge material is present that is close to equilibrium with the water. Very coarse fault gouge material behaves more like the rock matrix and the effects should be indistinguishable from an increased flow-wetted surface. Tracers may also diffuse from the main flow paths into stagnant water in the plane of the fracture. This, however, is probably only important for narrow flow paths and large fracture apertures. In order to obtain a good match using a 2D flow structure, higher values of the matrix parameters and large amount of fault gouge material are needed.

In the Task 6B2 simulation case studies, the assumption of a 3D or 2D flow geometry has only a marginal influence upon the recovery times for the tracers under the PA-type flow conditions that were modelled. The reason for this lies in the way the hydraulic boundary conditions are specified. In Task 6A and 6B the total flowrate of water through the system is specified by the rate at which water is pumped from the extraction borehole.

The conceptual difference between the 2D and 3D simulations in the Task 6A and 6B cases then lies in whether this "fixed" water flow is assumed to occur entirely with the 2D plane of Feature A or spread out over a 3D network of fractures. For the simulations carried out within Task 6B2 we have not specified the total flow, but rather, the hydraulic head gradient over the simulation volume with given transmissivities for channels within Feature A and the background fractures. This means that the same flow occurs within Feature A with or without the inclusion of background channels. The total flow, however, is greater when background channels are included in the model as additional flow can then occur in these channels.

As most of the tracer transport occurs within Feature A, it is reasonable to expect that most of the tracer particles encounter channels with the same FWS/q ratio whether background channels are included in the simulation, or not. The slight differences between the results for the two scenarios (i.e., with and without background channels) are due to a small number of tracer "particles" leaving the plane of Feature A and travelling through background channels.

If we were to specify the total flowrate in the system instead of the hydraulic gradient, however, we should expect quite different results between the two scenarios as we would then find very different FWS/q ratios in the channels lying within Feature A.

The uncertainty in the actual transmissivity of Feature A relative to the background transmissivity field was found to have a very strong influence on tracer recovery times for all tracers. As observed previously in conjunction with the Task 6A and 6B case studies, the flow porosity has negligible influence upon the recovery times for sorbing tracers.

7.2 The impact of the criterion used to choose the injection flow rate

In the Task 6A simulations, the criterion used for choosing an injection node was found to have a small, but noticeable influence upon the mean recovery times (t_{05}, t_{50}, t_{95}) for the tracers.

In the simulations, the criterion for selecting the injection node was that the flowrate through the node should be in an interval around the mean flow rate that would be expected at a radius of 5 m from the recovery borehole. It is probable, however, that the flow rate at the injection hole was larger than the average flow rate. Simulations were therefore performed where the criterion for selecting the injection nodes was a higher flowrate than the mean value (three times for the 3D- and two times for the 2D structure). There are two principal reasons why the flowrate measured experimentally may be larger than that expected average value; these are:

– The injection hole was chosen on the basis of a good hydraulic connection with the recovery hole and this also may imply that the flow through the injection hole is greater than the average value (i.e., the tracers were injected in a more conductive region of the Feature A flow structure).

– The injection borehole influences the flow of water in the fractured rock, giving a flowrate through the injection section that is larger than the average for the Feature A flow structure.

Theoretically, if the transmissivity of the injection borehole is much higher than that of the surrounding rock, the water flux through the borehole section could be as much as double that in the rock (Holmén, 1997). This is because the highly transmissive borehole section has an influence on the piezometric head gradient and thus the flow of water in the surrounding rock. In terms of potential flow theory (Bird et al., 1960), we can also say that the borehole will "capture" flow streamlines at a distance of one borehole radius on each side of the borehole (perpendicular to the flow field).

In the simulations, injecting the tracer at a node with a low flowrate can have an impact on the travel time. Tracer particles are generally more likely to follow a flowpath through strongly conductive channels than those that are less conductive. If tracer injection occurs in a region with a low flowrate, the tracer may need to traverse one or more poorly conductive channels before finding a strongly conductive pathway to the recovery borehole. The travel time in the poorly conductive adjacent channels exiting from an injection node may then lengthen the total travel time for the particles significantly.

For the case of the 3D structure, the recovery times (t_{05}, t_{50}, t_{95}) obtained in simulations where the injection node flowrate was three times longer than the mean flowrate were 60-80% of the recovery times obtained when the flowrate was the around the mean value. The difference was greatest for the non-sorbing tracers and less pronounced for the strongly sorbing tracers, although on a log-log scale the differences are difficult to distinguish clearly in the breakthrough concentration-time curves (BTCs).

7.3 The Relative Importance of Surface Sorption and Matrix Interaction

From the simulation data, it is apparent that the bulk of the particles released into the channel network follow a more or less direct route to the pumping node. For the purpose of making scoping calculations we can therefore probably make the assumption that the particles traverse a single channel of equivalent distance and use the analytical equation for particle travel time to draw conclusions about the overall transport processes.

If we consider the very simple case of one channel, Equation 3 can be rearranged to give the recovery time for the injected tracer:

$$t = \left(1 + \frac{2K_a}{\delta}\right) t_w + \frac{\sqrt{D_e K_d \rho_p}}{4\left[erf^{-1}\left(1 - C/C_0\right)\right]^2} \left(\frac{FWS}{q}\right)^2 \qquad (22)$$

The residence time of water in the channel is equal to the volume of the channel divided by the flowrate through the channel. As the volume of the channel is equal to the channel aperture multiplied by half the FWS, we can write the water residence time as:

$$t_w = \frac{FWS \times \delta}{2q} \tag{23}$$

And consequently:

$$t = \left(\frac{\delta}{2} + K_a\right)\frac{FWS}{q} + \frac{D_e K_d \rho_p}{4\left[erf^{-1}\left(1 - C/C_0\right)\right]^2}\left(\frac{FWS}{q}\right)^2 \tag{24}$$

For a strongly sorbing tracer (i.e., $K_a \gg \delta/2$) it can be seen from Equation 24 that the arrival time of a particle will be independent of the fracture aperture and only dependent upon the FWS/q ratio. For a strongly sorbing tracer we can write:

$$t \approx K_a \frac{FWS}{q} + \frac{D_e K_d \rho_p}{4\left[erf^{-1}\left(1 - C/C_0\right)\right]^2}\left(\frac{FWS}{q}\right)^2 \tag{25}$$

For the 3D case in Task 6A, the average FWS/q ratio is on the order of 32 m^2y/m^3. For the 2D case it is 1.1 m^2y/m^3. Under these conditions (i.e., with a pumping flowrate of 0.401 l/min) and assuming the validity of our physical model, most of the retardation of the sorbing tracers should occur on the fracture surfaces and very little retardation should arise from matrix interaction processes. This can be checked by substituting the appropriate parameter values into Equation 25, for say $C/C_0 \approx 0.5$. In fact, a quick estimation indicates that in the case of ^{241}Am and ^{99}Tc, matrix interaction probably accounts for less than 10% of the retardation in the 3D simulations and less than 0.5% in the 2D simulations.

Three case studies were made where surface sorption only, matrix interaction only, and both surface sorption and matrix interaction were considered. In simulations carried out for ^{241}Am, it was found that surface sorption accounted for most of the retardation. Simulations were also performed for ^{58}Co. In these simulations, the retardation was even more strongly dominated by the surface sorption than in the case of ^{241}Am. The recovery times (t_{50}) for each of these cases are shown in Figure 44. It is not necessary to perform the corresponding test simulations for a 2D flow-field as we already know that the flow in individual channels will be higher in the 2D case than the 3D case. This will lead to an even smaller influence of matrix interaction upon the results.

For the Task 6B simulations, the pumping flowrate at the recovery section has been reduced by a factor of 1000. As the FWS/q ratio is then 1000 times larger, the influence of matrix interaction will be much more important for the retardation of both sorbing and non-sorbing tracers. Using Equation 25, it is estimated that matrix interaction probably accounts for something on the order of 90-100% of the retardation for strongly sorbing tracers (^{241}Am and ^{99}Tc) in a 3D flow-field under the hydraulic conditions specified for Task 6B. For ^{58}Co, the results are bit more mixed and we find that surface sorption still has some influence on the tracer retardation.

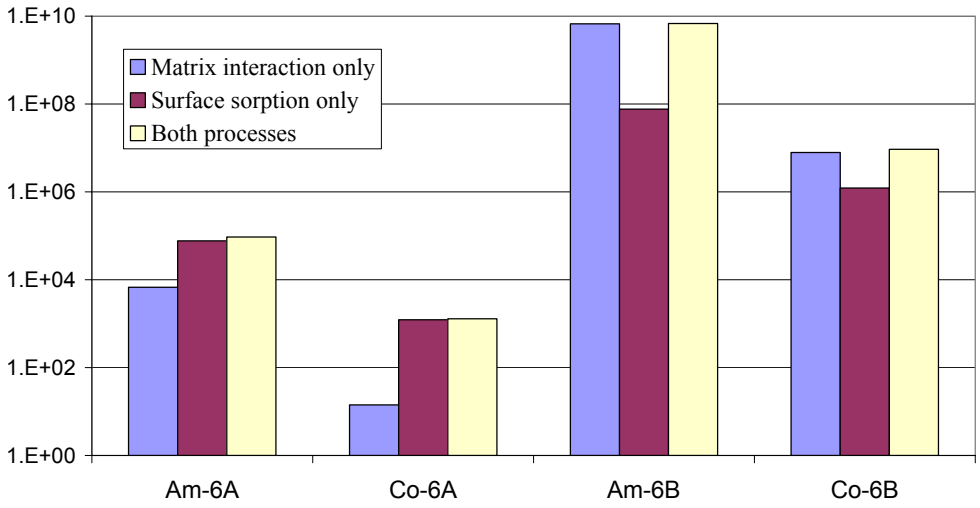

Figure 44 *Mean recovery times (t_{50}) for ^{241}Am and ^{58}Co for a Dirac pulse where the matrix interaction and surface sorption processes are considered both together and separately. Am-6A and Co-6A data refer to Task 6A results; Am-6B and Co-6B refer to Task 6B results.*

These predictions generally agree with simulations carried out for ^{241}Am. The results clearly identify matrix interaction as the dominant retardation mechanism for transport in a 3D flow-field configuration. For ^{85}Co, we find that surface sorption has some influence upon the tracer retardation. These results are also shown in Figure 44.

For non-sorbing tracers, the arrival time of the leading edge of the breakthrough curve is, in general, determined by the water residence time for the system. The trailing edge of the breakthrough curve, however, is strongly influenced by matrix interaction under the hydraulic conditions specified for Task 6B. Two additional simulations were made for ^{131}I. One of these considered the effects of matrix interaction while the other did not. For the case where matrix diffusion is included, the mean recovery time (t_{50}) was about 17 000 hours, which may be compared with about 5 400 hours for the case without matrix diffusion.

7.4 Influence of Channel Length in the Simulation Model

In the CHAN3D simulations it has been arbitrarily assumed that the channels have the same dimensions (0.5 m) as the packer distance used in the hydraulic characterisation experiments. To investigate how the choice of channel length used in the model impacts upon the simulation results, a sensitivity analysis has been performed for the Task 6A case where the channel length and thereby the number of channel elements has been varied from 0.25 m to 0.75 m. The conceptual simulation volume was 13 500 m^3 and only the length and number of channels were varied in the channel network. As the dimension of the channel influences both the channel conductance and the FWS per channel, these were adjusted appropriately.

The pumping flowrate was assumed to be the same as in the Task 6A evaluation (0.40 l/min), the tracer studied was ^{241}Am (Dirac pulse injection), and both a 3D and 2D flow configuration were modelled. The results of the sensitivity analysis are detailed in Appendix 3. It was found that the choice of channel length did have a minor, but statistically significant influence upon the mean recovery times for ^{241}Am in a 3D flow field. The standard deviation of the recovery times t_{05}, t_{50}, and t_{95} were found to decrease in the direction of increasing network size (i.e. number of nodes) in the 3D simulations. This is what would be expected if we consider the homogenising effect that increasing network size should have upon the particle transport times.

There was also a weak, systematic decrease in the mean recovery times with increasing network size. The estimated nominal FWS/q ratio also decreases with increasing network size, although the effect is very small. The nominal FWS/q ratio here is defined as the average total FWS encountered by each tracer "particle" divided by the expected mean channel flow (F_m) at a distance of 5m from the recovery borehole. As the particle recovery time decreases with decreasing FWS/q, this is possibly the source of the observed variation. As for the 3D case studies, the standard deviation of the recovery times in the 2D cases decreased with increasing network size as expected. In contrast to the 3D simulations, the mean recovery times were found to increase with increasing network size.

In the 2D simulations, the estimated nominal FWS/q ratio was roughly constant for all cases examined and it is not known why the mean recovery time increases. It is suspected that the discrepancy may relate to the increased level of heterogeneity in the 2D system compared with the 3D system (i.e. there are fewer active channels for particle transport in the 2D flow system than in the 3D flow system).

8 Conclusions

The simulation results for the non-sorbing (Hto, ^{131}I) and weakly sorbing (^{85}Sr) tracers contain no additional information that is useful for understanding the physics of the Feature A flow structure. This is because the breakthrough times for non-sorbing tracers are calibrated by adjusting the flow porosity to obtain a match with the experimental data and the shape of the breakthrough curves are dominated by the trailing edge of the tracer injection pulse.

The recovery times for all sorbing tracers under the Task 6A hydraulic conditions (i.e., a pumping rate of 0.40 l/min) are dominated by retardation due to surface sorption. For the high flowrates encountered in the flow structure, matrix interaction plays a very minor role for the estimated arrival times of 5% (t_{05}) and 50% (t_{50}) of the injected tracer mass. Only the trailing edge of the tracer pulse is influenced by matrix interaction processes.

Under the hydraulic conditions specified for Task 6B, surface sorption accounts for a much smaller proportion of the simulated tracer retardation and matrix interaction plays an overwhelming role for the transport time of the strongly sorbing tracer ^{241}Am. For the more weakly sorbing tracer ^{58}Co, surface sorption and matrix interaction may be equally important retardation mechanisms.

At present, it is not possible to conclude if the flow structure is 2D or 3D. However, there are several indications that a 3D flow structure is more probable. If a 2D flow structure is assumed, a mean fracture aperture of about 2 mm is required to match the flowrate pumped at the collection hole and the water residence time. Such large fracture apertures are not usually observed in the field. On the other hand, if it is assumed that the flow structure is 3D in nature, a more reasonable fracture aperture is obtained (0.07 mm). This fracture aperture is much closer to what would be expected, based upon previous experiences e.g., during the Stripa project (Birgersson et al., 1992). Moreover, predictions of the sorbing tracer tests STT1 using only independent data (Neretnieks and Moreno, 2003) have shown a good agreement with the experimental breakthrough curves. Finally, the tracer travel times predicted using the 2D flow structure are much shorter than the experimental values for the sorbing tracer used in STT1 experiment.

The sorbing tracer ^{99}Tc has not been detected in the STT1b experiment. However, the tracer should have been detectable in the recovery borehole within the time frame of the experiment according to the 2D simulation results. Breakthrough of tracer was predicted after 500 hours in the 2D simulations and after about 8000 hours in the 3D simulations. The “no-show” of ^{99}Tc is consistent with the 3D simulations although not in any way, conclusive.

The choice of injection node used in the simulations can have a small influence upon the results, although the differences are usually quite minor. The arbitrary choice of channel length used in the simulations appears to only have a minor influence on the consistency of the simulation results. The largest differences appear in very heterogeneous networks where there are only a few channels separating the injection and recovery nodes. Provided that there are at least 15-20 channels in the fastest route separating the injection node from the recovery node, the differences appear to be, for all practical purposes, negligible (at least for the cases studied in the present context).

The simulation results made in connection with the Task 6B2 case studies show that the uncertainty concerning the Feature A transmissivity relative to the background transmissivity field has a very strong influence upon the tracer recovery times. This was not fully explored in the Task 6A and 6B simulations as only the two limiting flow scenarios were studied (i.e., purely 2D flow, and 3D flow with no increased Feature A transmissivity).

9 References

"Äspö Hard Rock Laboratory – Annual Report 2000" (2001) Svensk Kärnbränslehantering AB, Technical Report TR-01-10.

Bird, R.B., Stewart, W.E., and Lightfoot, E.N. (1960) *Transport Phenomena*, John Wiley and Sons, New York. ISBN 0 471 07392.

Birgersson, L., Widén, H., Ågren, T., and Neretnieks, I. (1992) *"Tracer migration experiments in the Stripa Mine 1980-1991"*, SKB Technical Report TR 92-25.

Carbol, P. and Engkvist, I. (1997) *"Compilation of radionuclide sorption coeffiecients for performance assessment"*, SKB Report R-97-13, Swedish Nuclear Fuel and Waste Management Company.

Crawford, J. Moreno, L., and Neretnieks, I. (2003) "Determination of the flow-wetted surface in fractured media", *Journal of Contaminant Hydrology*, **61**: pp. 361-369.

Gylling, B. (1997) *"Development and Applications of the Channel Network Model for Simulation of Flow and Solute Transport in Fractured Rock"*, Ph.D. Thesis, Department of Chemical Engineering and Technology, Royal Institute of Technology.

Gylling, B., Birgersson, L., Moreno, L., and Neretnieks, I. (1998) "Analysis of a long-term pumping and tracer test using the Channel Network Model", *Journal of Contaminant Hydrology*, **32**: pp. 203-222.

Holmén, J.G. (1997) *"On the flow of groundwater in closed tunnels. Generic hydrogeological modelling of nuclear waste repository, SFL 3-5"*, Ph.D. Thesis, Institute of Earth Sciences, Uppsala University, SKB Technical Report TR 97-10.

Moreno, L. and Nerenieks, I. (1993) "Fluid and solute transport in a network of channels", *Journal of Contaminant Hydrology*, **14**: pp. 163-192.

Moreno, L., Tsang, Y.W., Tsang, C.F., Hale, F.V., and Neretnieks, I. (1988) "Flow and tracer transport in a single fracture. A stochastic model and its relation to some field observations", *Water Resources Research*, **24**: pp. 2033-3048.

Moreno, L., (2001) *"Evaluation of sorbing tracer tests using the channel network model. Äspö task force, Task 4E and 4F"*, SKB International Cooperation Report ICR-01-03, Swedish Nuclear Fuel and Waste Management Company.

Neretnieks, I., and Moreno, L., (2003) "Prediction of some in-situ tracer tests with sorbing tracers using independent data", *Journal of Contaminant Hydrology*, **61**: pp. 351-360

Neretnieks, I., (1980) "Diffusion in the rock matrix: An important factor in radionuclide migration", *Journal of Geophysical Research,* **85** No. B8: pp 4379-4397.

Ohlsson, Y. and Neretnieks, I. (1997) *"Diffusion data in granite. Recommended values"*, SKB Technical Report TR-97-20, Swedish Nuclear Fuel and Waste Management Company.

Robinson, P.C. (1984) *"Connectivity, flow and transport in network models of fractured media"*, Ph.D. Thesis, St. Catherine's College, Oxford University, Ref. TP 1072.

Selroos, J-O. and Elert, M. (2001) *"TASK 6A & 6B Modeling task specification - Version 1.0"*, Swedish Nuclear Fuel and Waste Management Company.

Vieno, T., and Nordman, H. (1999) *"Safety assessment of spent fuel disposal in Hästholmen, Kivetty, Olkiluoto and Romuvaara"*, TILA-99, Posiva 99-07, Posiva OY.

Winberg, A., Andersson, P., Hermanson, J., Byegård, J., Cvetkovic, V., and Birgersson, L., (2000) *"Äspö Hard Rock Laboratory – Final report of the first stage of the tracer retention understanding experiments"*, Technical Report TR-00-07, Swedish Nuclear Fuel and Waste Management Company

Yamashita, R. and Kimura, H. (1990) "Particle-tracking technique for nuclide decay chain transport in fractured porous media", *Journal of Nuclear Science and Technology*, 27: pp. 1041-1049.

Notation

a_R	$[L^2L^{-3}]$	specific flow-wetted surface
b	[L]	fracture half-width
C	$[L^2T^{-1}]$	fracture conductance
C_f	$[ML^{-3}]$	fracture fluid concentration
C_p	$[ML^{-3}]$	pore fluid concentration
C/C_0	[-]	dimensionless concentration
D_e	$[L^2T^{-1}]$	effective diffusivity
F_m	$[L^3T^{-1}]$	mean flow at node with distance r from pumping hole
FWS	$[L^2]$	flow-wetted surface
FWS_{tot}	$[L^2]$	total flow-wetted surface
G_0	$[LT^{-1/2}]$	matrix interaction parameter, $G_0 = \sqrt{D_e K_d \rho_p}$
H	[L]	difference in hydraulic head
K	$[LT^{-1}]$	hydraulic conductivity
K_a	[L]	linear surface sorption constant
K_d	$[L^3M]$	(bulk) linear partition coefficient coefficient
K_d'	$[L^3M]$	linear partition coefficient for matrix sorption
L	[L]	packer separation
n	[-]	number of measurements
P_0	[-]	estimated probability of packed-off section containing no hydraulically conductive fractures
P_U	[-]	upper confidence limit for P_0
P_L	[-]	lower confidence limit for P_0
Q	$[L^3T^{-1}]$	total pumping flowrate
q	$[L^3T^{-1}]$	advective flowrate
r	[L]	radius of sphere or disc
R_*	$[LL^{-1}]$	surface sorption retardation constant
t_w	[T]	hydraulic residence time
t	[T]	time
t_{05}	[T]	recovery time for 5% of the injected tracer
t_{50}	[T]	recovery time for 50% of the injected tracer
t_{95}	[T]	recovery time for 95% of the injected tracer
T	$[L^2T^{-1}]$	fracture transmissivity
W	[L]	fracture width
x	[L]	distance within rock matrix
z	[L]	distance along fracture
Z	[L]	channel length
$\bar{\delta}$	[L]	mean hydraulic aperture of fracture
ε_f	$[L^3L^{-3}]$	flow porosity
ε_p	$[L^3L^{-3}]$	matrix porosity
μ_{LC}	[-]	log-mean conductance
μ_{LK}	$[\log_{10}(LT^{-1})]$	log-mean hydraulic conductivity
ρ_p	$[ML^{-3}]$	bulk density of rock matrix (incl. porosity)
ρ_s	$[ML^{-3}]$	solid density (porosity-free) of rock matrix
σ_{LC}	[-]	standard deviation of log-mean conductance
σ_{LK}	$[\log_{10}(LT^{-1})]$	standard deviation of log-mean hydraulic conductivity

List of Figures (Appendices)

List of Tables (Appendices)

Appendix 1

Input Data: Some Theoretical Considerations

- **Estimation of the Channel Conductance Distribution**
- **Estimation of the Flow-Wetted Surface in Fractured Rock**

Estimation of the Channel Conductance Distribution

The conductances used in the CHAN3D program are derived based upon analogy with flow through a porous medium of unit cell volume as indicated in Figure 45.

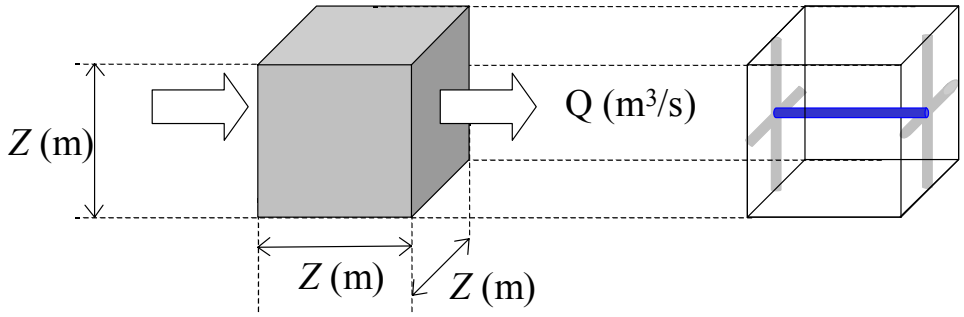

Figure 45 *Flow analogy for 1-dimensional flow in a porous medium of unit cell volume.*

For a cube with dimensions $Z \times Z \times Z$, the unidirectional flowrate is given by Darcy's law as:

$$Q = K Z^2 \frac{\Delta H}{Z} \tag{26}$$

The flowrate in CHAN3D is defined by definition as the conductance of a channel multiplied by the head differential over the channel (i.e., $Q = C\Delta H$). Combining this flow definition with Darcy's law gives for the channel conductance:

$$C = K Z \tag{27}$$

where Z is the channel length used in the CHAN3D simulation. If the experimental data is instead given in the form of a transmissivity (T) distribution (for experimental data with a packer separation of distance L), the conductance is:

$$C = \left(\frac{T}{L} \right) Z \tag{28}$$

To convert from hydraulic conductivity (m/s) to channel conductance (m^2/s) we therefore have:

$$\mu_{LC} = \log_{10}(Z) + \mu_{LK} \tag{29}$$

$$\sigma_{LC} = \sigma_{LK} \tag{30}$$

Where μ_{LK} is the $\log_{10}$-mean hydraulic conductivity and μ_{LC} is the mean $\log_{10}$ channel conductance; σ_{LK} and σ_{LC} are the corresponding $\log_{10}$ standard deviations of hydraulic conductivity and channel conductance.

These conversion formulae are only valid for channel lengths that are roughly the same size as the packer length used in the hydraulic tests. For channel lengths that differ markedly from the packer distance, the mean and standard deviation of the distribution must be scaled appropriately.

The channel conductances in CHAN3D are assigned by the formula:

$$\log_{10} C = \mu_{LC} + (randn) \times \sigma_{LC} \quad (31)$$

where *randn* is a random normal deviate (i.e., a normally-distributed, random number with mean 0, and standard deviation 1).

Estimation of the Flow-Wetted Surface in Fractured Rock

The flow-wetted surface is estimated from geometrical-statistical considerations, based upon the number of hydraulically conductive fractures (channels) intersected by a borehole drilled in the rock mass. We consider a rock volume with a number of channels randomly oriented in space. In this rock volume we also consider that the channels have some mean length (L), width (W), and area (A).

A borehole drilled through the rock mass will intersect a channel, on average, every H metres. To estimate the flow-wetted surface, we want to be able to relate the frequency with which channels are intersected by the borehole with the number of channels in a given volume of rock. We do not know a priori what the average dimensions (L and W) of the channels are. The only details we know are the borehole diameter (D) and the average distance between conductive fractures in the rock (H) obtained from hydraulic packer tests.

Given that the channels are randomly distributed in space they can be oriented parallel, perpendicular, or at some oblique angle relative to the borehole. Channels that are, or nearly, perpendicular to the borehole are more likely to be intersected than those having sharply oblique inclinations. For this reason, we consider the average area of the channels projected onto the plane perpendicular to the borehole rather than the actual average area of the channels.

As we are interested in the "average" properties of the rock volume, the projected areas are then redistributed over this plane with a separation between them equal to the borehole diameter. The separation between the projected channel areas is equal to the borehole diameter, as the borehole only has to touch the edge of a channel for a hydraulic test to indicate a conductive feature. This concept is illustrated in Figure 46 below where the variables W_p and L_p represent the average projected dimensions corresponding to the actual channel length and width.

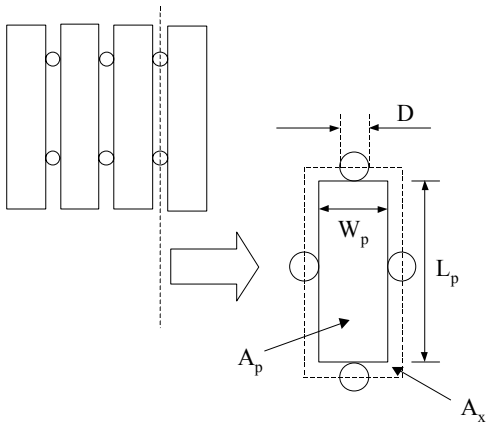

Figure 46 *Schematic diagram showing projected channel areas (A_p) distributed over the plane perpendicular to the borehole axis. The projected channels have length L_p and width W_p. and are separated by a distance equal to the borehole diameter. A_x is the area comprising the spaces between the channels. (Note that the projected areas are actually parallelograms and are not necessarily rectangular as shown in the figure).*

It should be noted that the average projected area is not equal to the product of the projected length and width, as would be the case for a rectangular shape such as that depicted in Figure 46 above. This is because the projected areas are not necessarily rectangular and are actually parallelograms. The perimeter of the projected area, however, is the same regardless of whether it is in the form of a rectangle or a parallelogram.

If we visualise a single channel of length *L* and width *W*, with centre fixed at the Cartesian origin, we can pivot the channel in any direction and it will trace out a spherical surface as shown schematically in Figure 47 below:

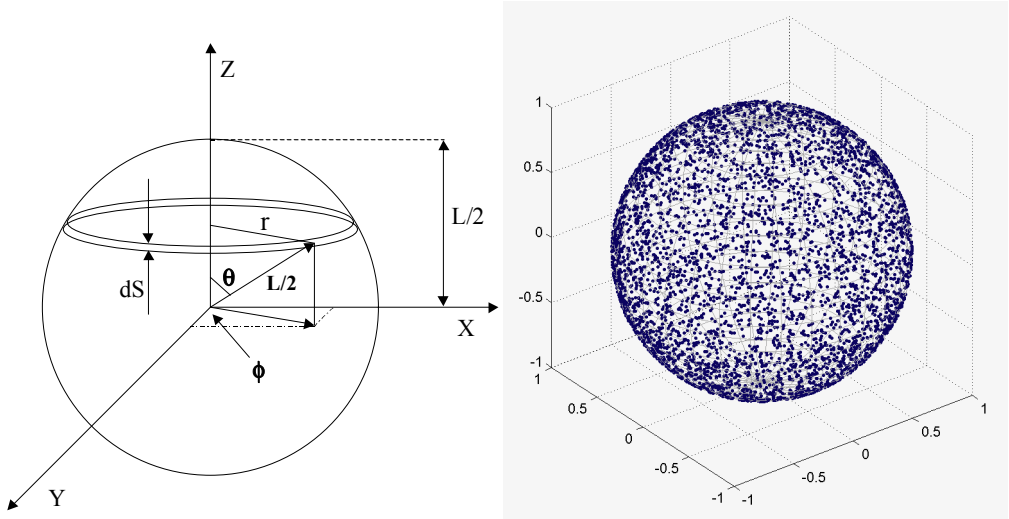

Figure 47 *Schematic diagram of a channel with centre fixed at the origin. The channel can be pivoted in any direction and it will trace out a spherical surface with diameter equal to the channel length (L). The z-axis corresponds to the axial direction of the borehole; x-y axis is the plane perpendicular to the borehole. The figure on the right-hand side shows the distribution of 4500 randomly oriented channels touching the surface of the sphere.*

If a large number of channels are randomly oriented in this fashion, the extremities of these channels should be randomly distributed over the surface of the sphere as shown in the diagram on the right-hand side of Figure 47. The projected length of the channel will be equal to the length vector projected onto the *x*-*y* plane and is dependent upon the inclination of the channel relative to the borehole axis (θ). As the channels are evenly distributed with reference to the surface of the sphere, this suggests that the average projected length should be calculated based upon the first moment of the projected length relative to the spherical surface.

From geometrical considerations, the differential area variable (*dS*) is given by:

$$dS = 2\pi r\left(L/2\right)d\theta = 2\pi\left(L/2\right)\sin\theta\left(L/2\right)d\theta \tag{32}$$

The length sum over all possible angles is then:

$$L_{sum} = 2\int_0^{\frac{\pi}{2}} r\, dS = \frac{\pi}{2}L^3\int_0^{\frac{\pi}{2}}\sin^2\theta\, d\theta$$

$$= \frac{\pi}{2}L^3\int_0^{\frac{\pi}{2}}1-\cos 2\theta\, d\theta = \frac{\pi}{2}L^3\left[\frac{\theta}{2}-\frac{\sin 2\theta}{4}\right]_0^{\frac{\pi}{2}} = \frac{\pi^2}{8}L^3 \tag{33}$$

The average projected length, L_p is then obtained by:

$$L_p = \frac{\frac{\pi}{2}\int_0^{\frac{\pi}{2}} r\, dA}{\frac{\pi}{2}\int_0^{\frac{\pi}{2}} dA} = \frac{L^3\int_0^{\frac{\pi}{2}}\sin^2\theta\, d\theta}{L^2\int_0^{\frac{\pi}{2}}\sin\theta\, d\theta} = L\frac{\pi}{4} \tag{34}$$

In the same fashion, the average projected width of the channel is found to be:

$$W_p = W\frac{\pi}{4} \tag{35}$$

The average projected perimeter is the same regardless of whether the projected shape is a rectangle or a parallelogram and is equal to twice the sum of W_p and L_p.

The projected area is obtained by taking the inner product of the area vector (perpendicular to the length vector) and the unit vector of the projection plane (the unit vector in the direction of the *z*-axis). Once again, we take the first moment of the projected area relative to the spherical surface to find the average projected area (A_p). The area sum over all possible angles is then:

$$A_{sum} = 2\int_0^{\frac{\pi}{2}} A\, dS = \frac{\pi}{2}AL^2\int_0^{\frac{\pi}{2}}\cos\theta\sin\theta\, d\theta$$

$$= \frac{\pi}{2}AL^2\int_0^{\frac{\pi}{2}}\frac{\sin 2\theta}{2}\, d\theta = \frac{\pi}{4}AL^2\left[-\cos 2\theta\right]_0^{\frac{\pi}{2}} = \frac{\pi}{4}AL^2 \tag{36}$$

The average projected area, A_p is then obtained by:

$$A_p = \frac{\frac{\pi}{2}\int_0^{\frac{\pi}{2}} A\cos\theta\, dA}{\frac{\pi}{2}\int_0^{\frac{\pi}{2}} dA} = \frac{AL^2\int_0^{\frac{\pi}{2}}\cos\theta\sin\theta\, d\theta}{L^2\int_0^{\frac{\pi}{2}}\sin\theta\, d\theta} = \frac{A}{2} = \frac{LW}{2} \tag{37}$$

The average projected area, A_0 required for a channel to be intersected by a borehole is equal to the average projected area of the channel (A_p) plus the area comprising the space between the channels (A_x) as illustrated in Figure 46. The area A_0 is given by:

$$A_0 = A_p + A_x \approx \frac{LW}{2} + D\left(L_p + W_p\right) + D^2$$

$$= \frac{LW}{2} + \frac{\pi}{4} D\left(L + W\right) + D^2 \tag{38}$$

If the average distance between channels intersected by the borehole is H, then the average rock volume containing one channel is equal to HA_0. The specific flow-wetted surface area, a_R (m^2/m^3) is the actual surface area of the channel ($2A$) divided by the rock volume HA_0. The specific flow-wetted surface is thus:

$$a_R = \frac{2A}{HA_0} \approx \frac{2LW}{H\left(\frac{LW}{2} + \frac{\pi}{4} D\left(W + L\right) + D^2\right)} \tag{39}$$

If the borehole diameter is sufficiently small in relation to the channel dimensions (L and W), equation 39 simplifies to:

$$a_R \approx \frac{4}{H} \tag{40}$$

If the exact number of conductive fractures in the rock is known, the value of H is equal to the borehole depth divided by the number of conductive fractures. The fracture frequency, λ (fractures/packer section) is equal to the packer spacing, L, divided by the average distance between fractures:

$$\lambda = L/H \tag{41}$$

The specific FWS can therefore be written as:

$$a_R = 4\lambda/L \tag{42}$$

If the distribution of fractures in a homogeneous rock mass can be assumed to be random, any hydraulic measurements performed to identify the locations of the fractures can be described with Poisson statistics for a sufficiently large number of measurements.

Whether, or not, the fracture distribution is truly random could be tested using a rigorous test for spatial randomness. If this test is based upon the hydraulic measurements, however, it will only indicate if the incidences of conductive sections are clustered, as there is no way of distinguishing which fractures within packed-off sections (i.e., those identified from the borehole core) are conductive or non-conductive.

If we consider as a working hypothesis, however, that the fractures are randomly distributed the probability of finding a given number, x of open (i.e., hydraulically conductive) fractures within a random packer section is then given by:

$$P\left(\lambda, x\right) = \frac{\lambda^x}{x!} e^{-\lambda} \tag{43}$$

It cannot be determined, on the basis of hydraulic measurements using packed-off borehole sections, whether a conductive interval contains only one fracture or multiple fractures. This means that if hydraulic measurements are used to estimate the frequency of open fractures in a borehole, the result will tend to underestimate the actual number.

Statistically, the fraction of undetected fractures, f_u is given by:

$$f_u = \frac{\lambda - \left(1 - P(\lambda, 0)\right)}{\lambda} = 1 - \frac{\left(1 - e^{-\lambda}\right)}{\lambda} \tag{44}$$

The probability of finding multiple fractures in a given packer section as well as the statistical fraction of undetected fractures is shown in Figure 48 as a function of the fracture frequency.

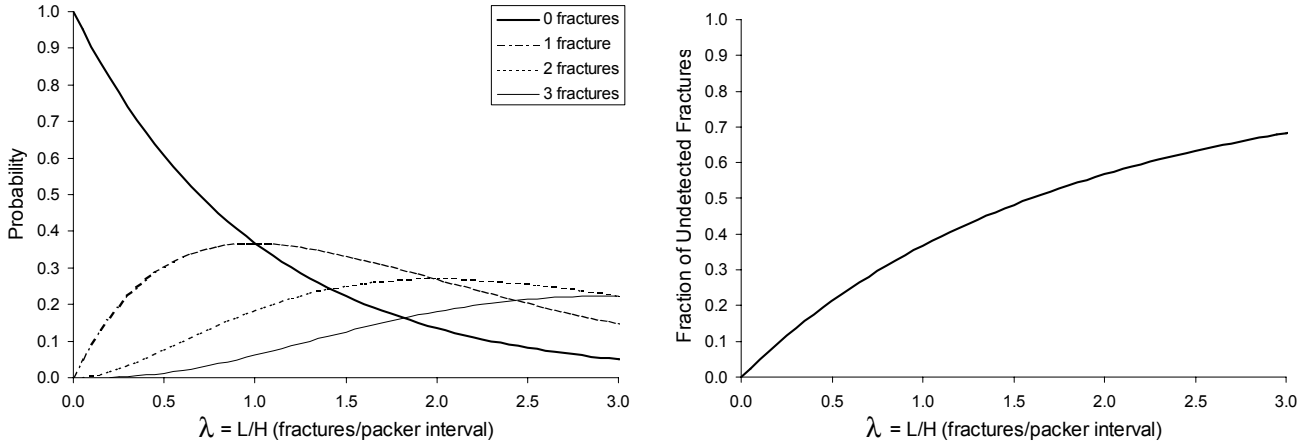

Figure 48 *Probability of finding multiple fractures in a given packer section as well as the statistical fraction of undetected fractures as a function of fracture frequency.*

The results indicate that for a packer distance of roughly the same size as the average fracture spacing ($\lambda = 1$), up to 40% of the fractures will remain undetected. The fraction of undetected fractures increases with increasing fracture frequency and the packer spacing used for measurements should preferably be smaller than, and certainly not larger than, the average fracture spacing.

In order to address the uncertainty of estimating the true number of fractures, the Poisson distribution can be used to estimate the "actual" fracture frequency from the proportion of non-conductive sections measured in hydraulic tests. The actual fracture frequency is estimated by:

$$\lambda = -\ln\left(P_0\right) \tag{45}$$

An estimate of the actual specific FWS, a_R is therefore given by:

$$a_R = -\frac{4}{L}\ln\left(P_0\right) \tag{46}$$

where P_0 is the probability of finding a non-conductive packer section during the borehole test. This is equal to the number of non-conductive sections identified, divided by the total number of sections tested. The estimated fracture frequency is plotted in Figure 49 as a function of the fraction of non-conductive packer intervals.

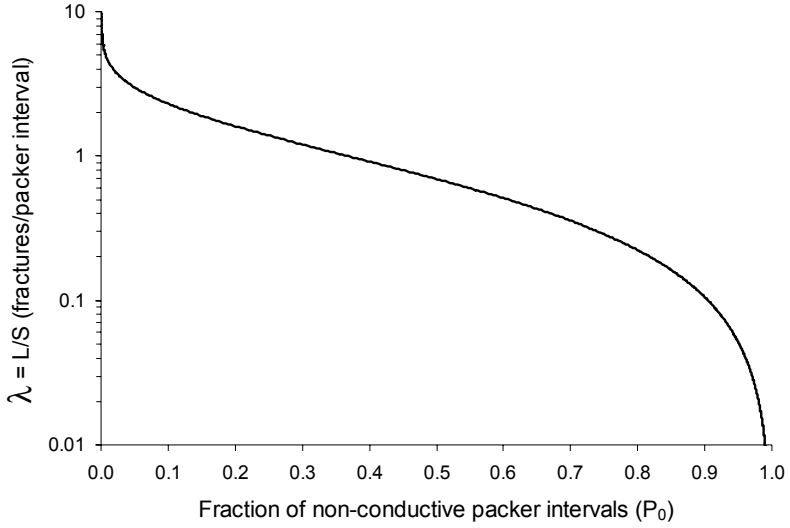

Figure 49 *Estimated fracture frequency as a function of the fraction of non-conductive intervals in a hydraulic packer test.*

From Figure 49 it can be seen that the most reliable estimate of the a_R will be obtained in the approximately linear portion of the curve when the fraction of non-conducting intervals is at least 20% and less than about 80%. As the fraction of non-conducting packer intervals is only an estimate of the true probability of finding a non-conducting interval, a confidence interval may be constructed for the estimated a_R. For a finite sample size, n, the probability of finding a non-conductive interval is given by the binomial distribution.

The $100(1-\alpha)\%$ binomial confidence interval for the estimated a_R may be calculated with the following expression:

$$-\frac{4}{L}\ln(P_U) \le a_R \le -\frac{4}{L}\ln(P_L) \tag{47}$$

For a data set consisting of n measurements, the two-sided confidence limits (P_U and P_L) are determined by solving the associated cumulative binomial probability equations:

$$\sum_{k=0}^{nP_0}\binom{n}{k}P_U^k\left(1-P_U\right)^{n-k} = \alpha/2 \tag{48}$$

$$\sum_{k=0}^{nP_0-1}\binom{n}{k}P_L^k\left(1-P_L\right)^{n-k} = 1-\alpha/2 \tag{49}$$

It should be noted that the confidence interval calculated in this manner is not symmetric about the estimated a_R given by equation 46 unless the sample size is large.

The confidence intervals calculated using equation 47 (or the normal approximation to the binomial distribution) only consider the possibility that more than one fracture will be found in any given packer section. The evaluation assumes that the hydraulic measurements are accurate (i.e., that they can detect low flow-rates, that individual fractures do not overlap adjacent packer sections, and that leaky packers do not corrupt the measurements).

If the method used to detect water flow within the packed-off section is not sufficiently sensitive, many fractures may remain undetected and thus lead to a significant underestimation of the FWS. Under field conditions, some or all of the above mentioned factors will reduce the accuracy of the estimation to some degree. For this reason, the confidence intervals calculated should be considered as the minimum degree of variation that can be expected to arise from purely statistical consideration of the fracture frequency.

It should also be remembered that conductive fractures identified using borehole tests might not be hydraulically conductive under natural conditions with different hydraulic gradients and boundary conditions.

The probability that a fracture with a random orientation will overlap adjacent packer sections increases with decreasing packer separation. Consequently, there is a lower limit to the practical size of a packer interval that can be used in a hydraulic test. This problem can be reduced somewhat by using longer packers, although there is also a practical limit to the dimensions of the packers that can be used efficiently.

Mechanically eroded borehole walls and loose debris can also cause problems by preventing the establishment of a tight seal over the packed-off section. This can also lead to short-circuiting of the packers and an overestimation of the FWS.

Appendix 2

Task 6A. Breakthrough Concentration-Time Curves (BTCs)

- **3D simulations using experimental tracer injection data (3DQ1)**
- **Breakthrough time summary for modelled tracers (3DQ1)**
- **Maximum nuclide release rate (3DQ1)**
- **Comparison of injection pulse data and Dirac pulse arrival times (3DQ1)**
- **Comparison of 3D simulations (using experimental tracer injection data) with high and low injection flow criterion – 3DQ1 & 3DQ1b**
- **Breakthrough time summary for modelled tracers (3DQ1b)**
- **2D simulations using experimental tracer injection data (2DQ1)**
- **Breakthrough time summary for modelled tracers (2DQ1)**
- **Maximum nuclide release rate (2DQ1)**
- **Comparison of injection pulse data and Dirac pulse arrival times (2DQ1)**
- **Comparison of 2D simulations (using experimental tracer injection data) with high and low injection flow criterion – 2DQ1 & 2DQ1b**
- **Breakthrough time summary for modelled tracers (2DQ1b)**
- **Comparison of 2D & 3D simulations (using experimental tracer injection data) – 3DQ1, 2DQ1**
- **Comparison of 2D & 3D simulations (Dirac pulse) – 3DQ1, 2DQ1**

3D Simulations using experimental tracer injection data (3DQ1)

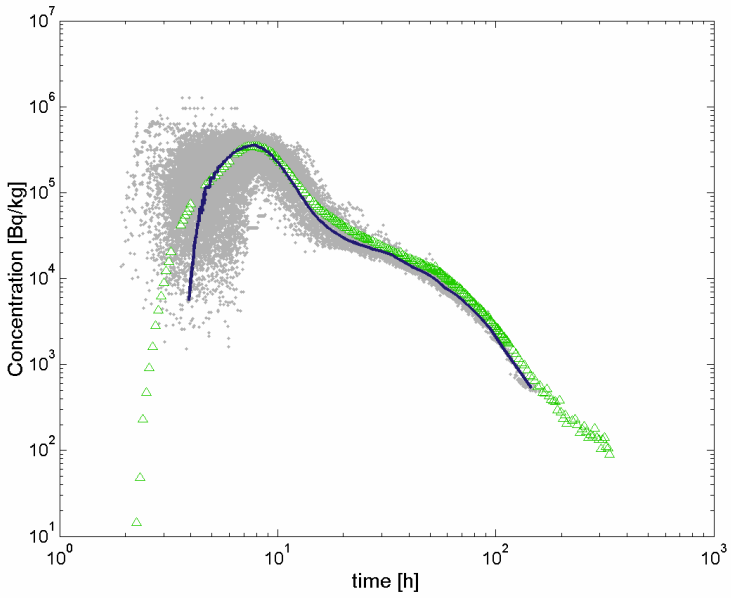

Figure 50 *Breakthrough concentration-time profile for Hto (3DQ1). The simulated results are shown as a probability density map (composite of 100 realisations). Mean of simulated results is shown as a blue curve. Triangular markers indicate experimental data for the STT1b test.*

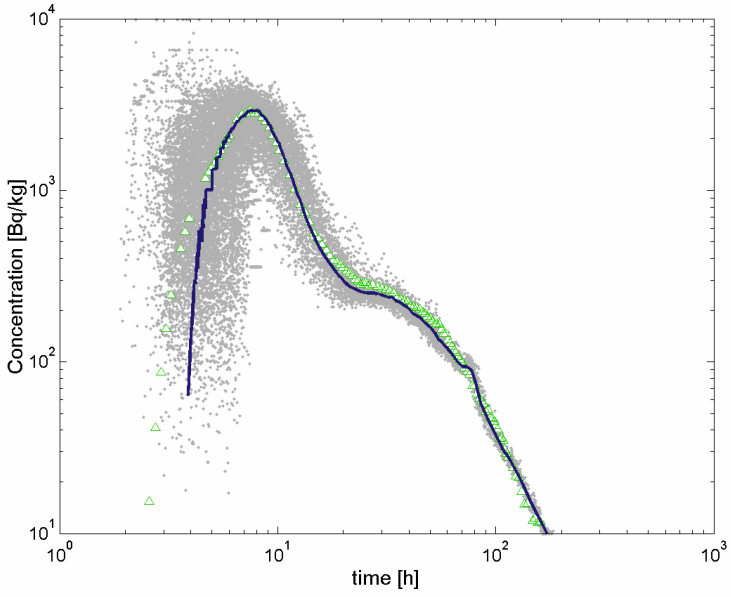

Figure 51 *Breakthrough concentration-time profile for ^{131}I (3DQ1). The simulated results are shown as a probability density map (composite of 100 realisations). Mean of simulated results is shown as a blue curve. Triangular markers indicate experimental data for the STT1b test.*

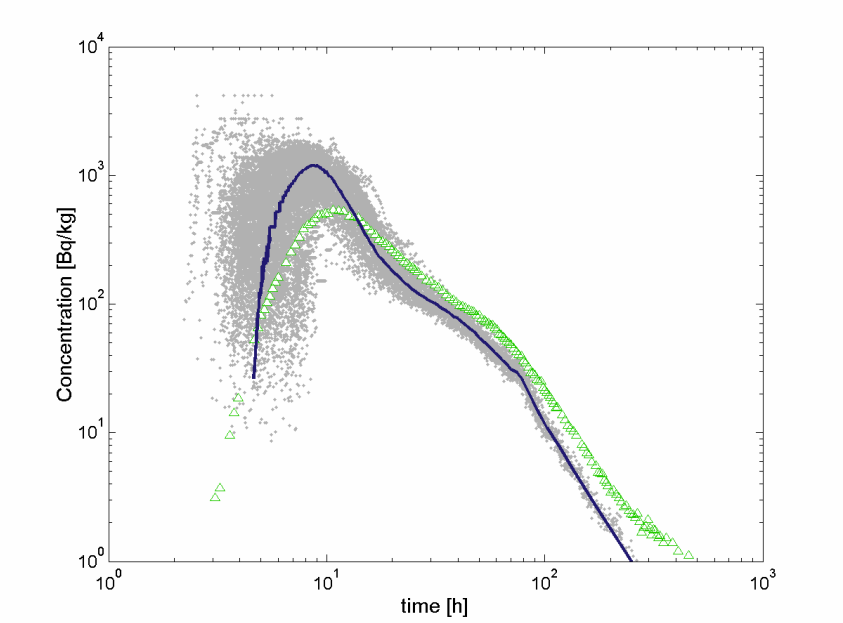

Figure 52 *Breakthrough concentration-time profile for ^{85}Sr (3DQ1). The simulated results are shown as a probability density map (composite of 100 realisations). Mean of simulated results is shown as a blue curve. Triangular markers indicate experimental data for the STT1b test.*

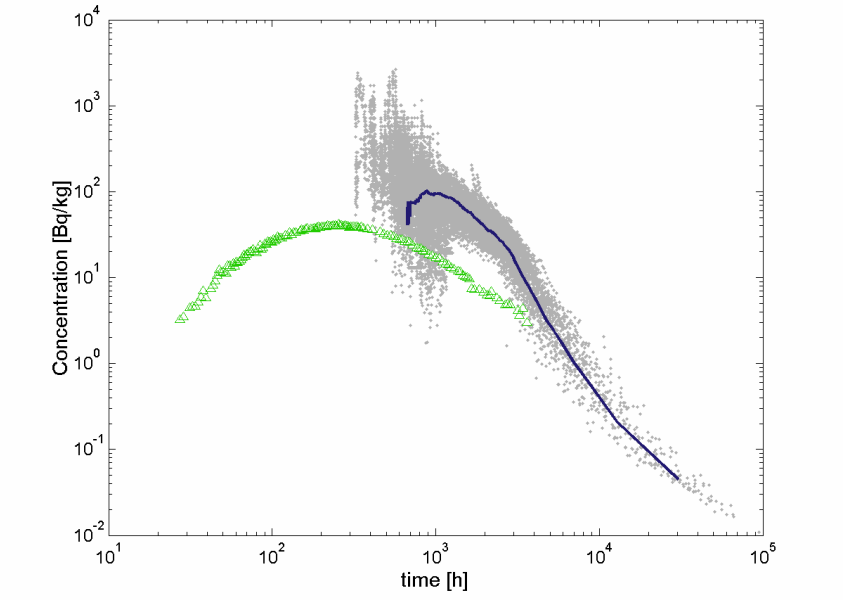

Figure 53 *Breakthrough concentration-time profile for ^{58}Co (3DQ1). The simulated results are shown as a probability density map (composite of 100 realisations). Mean of simulated results is shown as a blue curve. Triangular markers indicate experimental data for the STT1b test.*

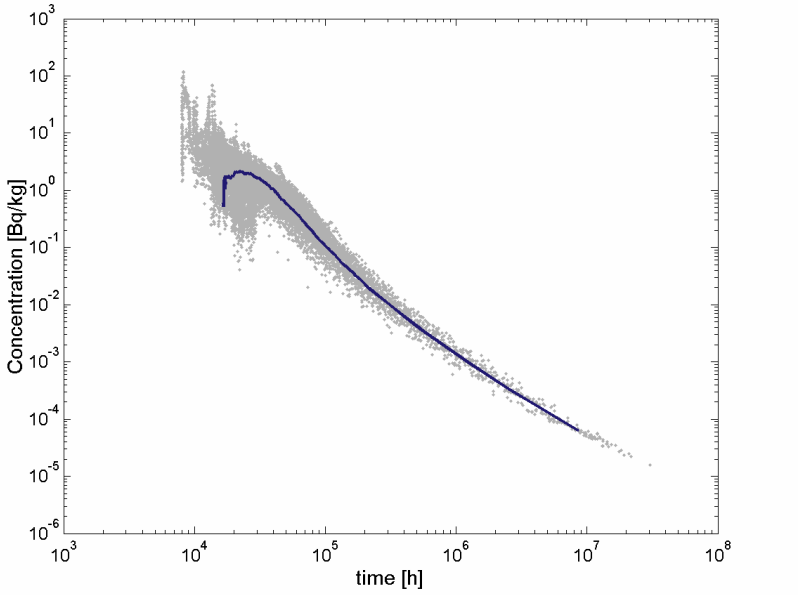

Figure 54 *Breakthrough concentration-time profile for ^{99}Tc (3DQ1). The simulated results are shown as a probability density map (composite of 100 realisations). Mean of simulated results is shown as a blue curve.*

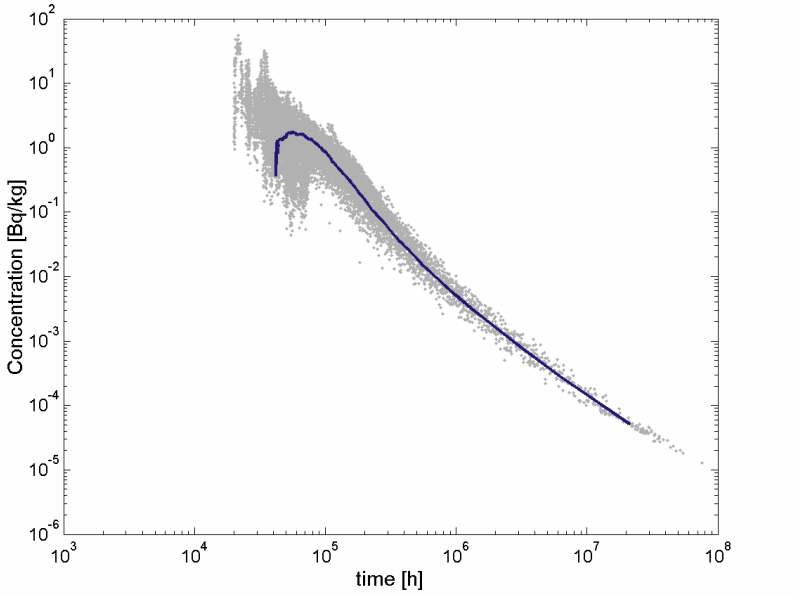

Figure 55 *Breakthrough concentration-time profile for ^{241}Am (3DQ1). The simulated results are shown as a probability density map (composite of 100 realisations). Mean of simulated results is shown as a blue curve.*

Breakthrough time summary for modelled tracers (3DQ1)

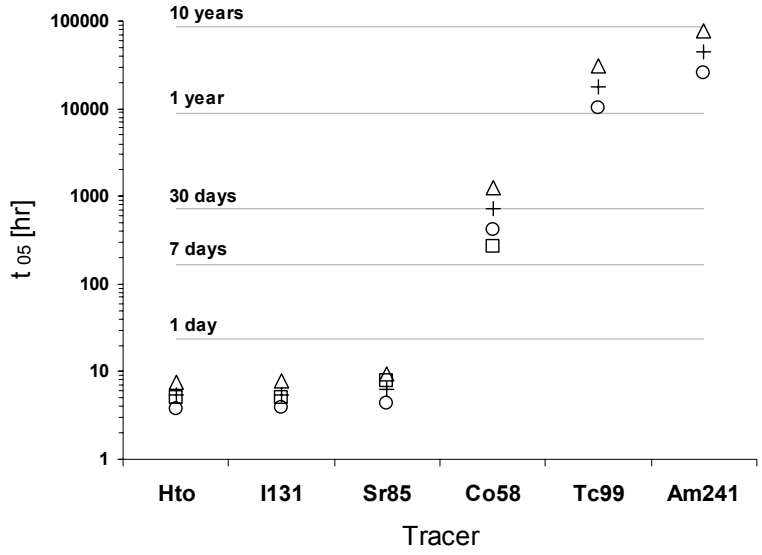

Figure 56 *Breakthrough times for 5% (t_{05}) of the injected tracer (3DQ1). 5% (circles), 50% (+ symbols), and 95% (triangles) percentile levels are shown for the simulated results. Experimental results (squares) are shown for Hto, ^{131}I, ^{85}Sr, and ^{58}Co.*

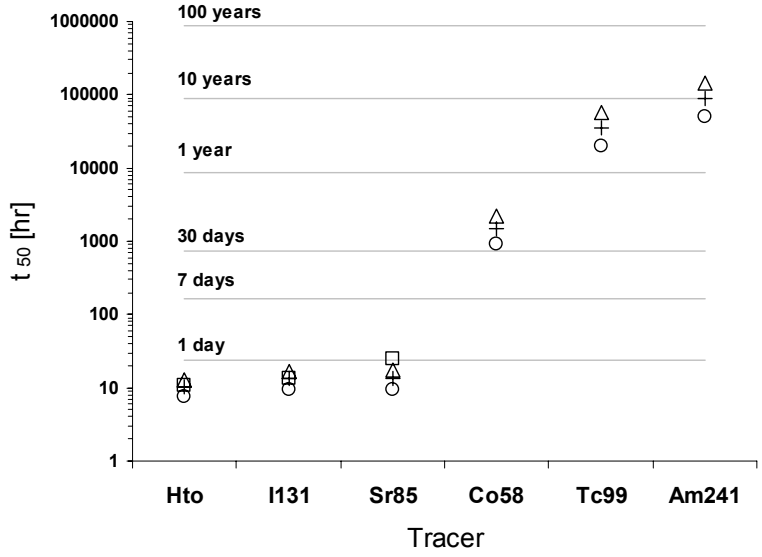

Figure 57 *Breakthrough times for 50% (t_{50}) of the injected tracer (3DQ1). 5% (circles), 50% (+ symbols), and 95% (triangles) percentile levels are shown for the simulated results. Experimental results (squares) are shown for Hto, ^{131}I, ^{85}Sr, and ^{58}Co.*

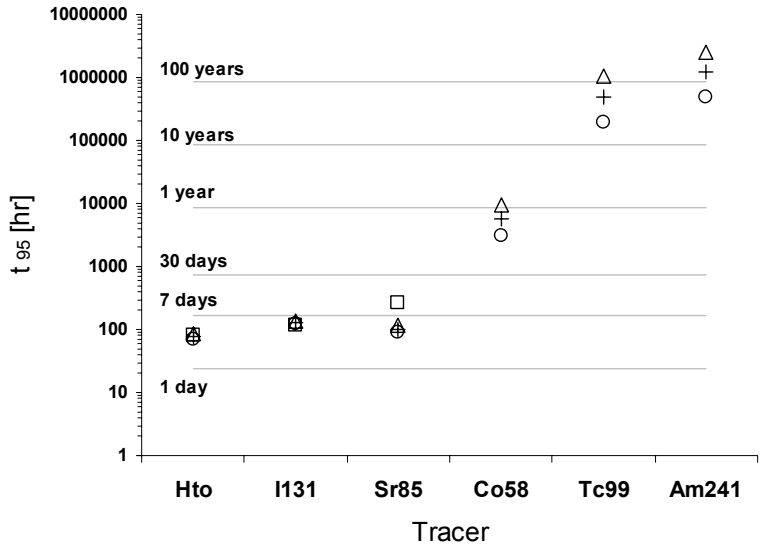

Figure 58 *Breakthrough times for 95% (t_{95}) of the injected tracer (3DQ1). 5% (circles), 50% (+ symbols), and 95% (triangles) percentile levels are shown for the simulated results. Experimental results (squares) are shown for Hto, ^{131}I, ^{85}Sr, and ^{58}Co.*

Maximum nuclide release rate (3DQ1)

Table 3 Maximum nuclide release rate [Bq/y] for simulation series 3DQ1. Results are given for experimental breakthrough data, simulated injection pulse data, and for Dirac pulse data. Simulation data is based upon mean peak breakthrough concentration for 100 realisations.

Tracer	Exp-M_R [Bq/y]	M_R [Bq/y]	Dirac-M_R [Bq/y]
Hto	7.31×10^{10}	3.58×10^{9}	7.76×10^{9}
^{131}I	6.14×10^{8}	2.83×10^{9}	7.75×10^{9}
^{85}Sr	1.13×10^{8}	2.76×10^{9}	5.89×10^{9}
^{58}Co	8.78×10^{6}	2.26×10^{7}	3.75×10^{7}
^{99}Tc	n/a	9.63×10^{5}	9.61×10^{5}
^{241}Am	n/a	3.84×10^{5}	3.84×10^{5}

Comparison of injection pulse data and Dirac pulse arrival times (3DQ1)

Table 4 **Mean travel time (t_{05}), standard deviation (σ_{t05}), and Z-statistic for comparison between experimental injection data and Dirac pulse boundary condition. Data is for 3DQ1 simulation series.**

Tracer	t_{05} [h]	σ_{t05}	Dirac-t_{05} [h]	Dirac-σ_{t05}	Z-statistic
Hto	5.5	1.2	4.0	1.1	8.7
^{131}I	5.7	1.3	4.0	1.1	9.7
^{85}Sr	6.5	1.5	4.9	1.3	8.2
^{58}Co	773	229	729	214	1.4
^{99}Tc	1.90×10^{4}	5.8×10^{3}	1.90×10^{4}	5.8×10^{3}	0.0
^{241}Am	4.78×10^{4}	14.5×10^{3}	4.76×10^{4}	14.5×10^{3}	0.1

Table 5 **Mean travel time (t_{50}), standard deviation (σ_{t50}), and Z-statistic for comparison between experimental injection data and Dirac pulse boundary condition. Data is for 3DQ1 simulation series.**

Tracer	t_{50} [h]	σ_{t50}	Dirac-t_{50} [h]	Dirac-σ_{t50}	Z-statistic
Hto	10.3	1.9	6.3	1.7	16.1
^{131}I	13.1	2.3	6.2	1.6	24.5
^{85}Sr	13.4	2.6	7.8	2.1	16.8
^{58}Co	1.55×10^{3}	413	1.29×10^{3}	387	4.6
^{99}Tc	3.73×10^{4}	1.19×10^{4}	3.73×10^{4}	1.19×10^{4}	0.0
^{241}Am	9.37×10^{4}	2.98×10^{4}	9.34×10^{4}	2.98×10^{4}	0.1

Table 6 **Mean travel time (t_{95}), standard deviation (σ_{t95}), and Z-statistic for comparison between experimental injection data and Dirac pulse boundary condition. Data is for 3DQ1 simulation series.**

Tracer	t_{95} [h]	σ_{t95}	Dirac-t_{95} [h]	Dirac-σ_{t95}	Z-statistic
Hto	77	4	17	5	98
^{131}I	129	5	16	5	171
^{85}Sr	102	9	28	10	56
^{58}Co	5.87×10^{3}	1.87×10^{3}	5.49×10^{3}	1.94×10^{3}	1.4
^{99}Tc	5.14×10^{5}	2.48×10^{5}	5.14×10^{5}	2.48×10^{5}	0.0
^{241}Am	1.28×10^{6}	6.15×10^{5}	1.28×10^{6}	6.15×10^{5}	0.0

Comparison of 3D simulations (using experimental tracer injection data) with high and low injection flow criterion – 3DQ1 & 3DQ1b

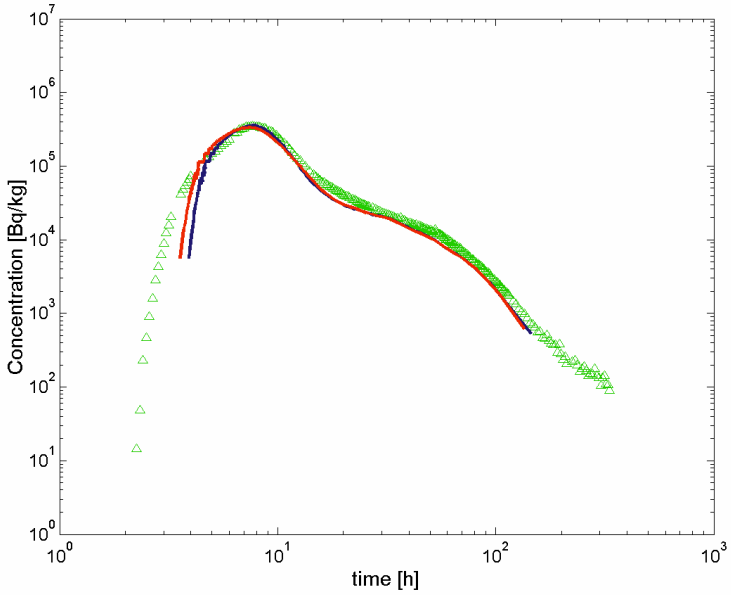

Figure 59 *Breakthrough concentration-time profile for Hto. The simulated results are given as the mean of 100 realisations. Results for 3DQ1 simulations are shown as a blue curve. Results for 3DQ1b simulations are shown as a red curve. Triangular markers indicate experimental data for the STT1b test.*

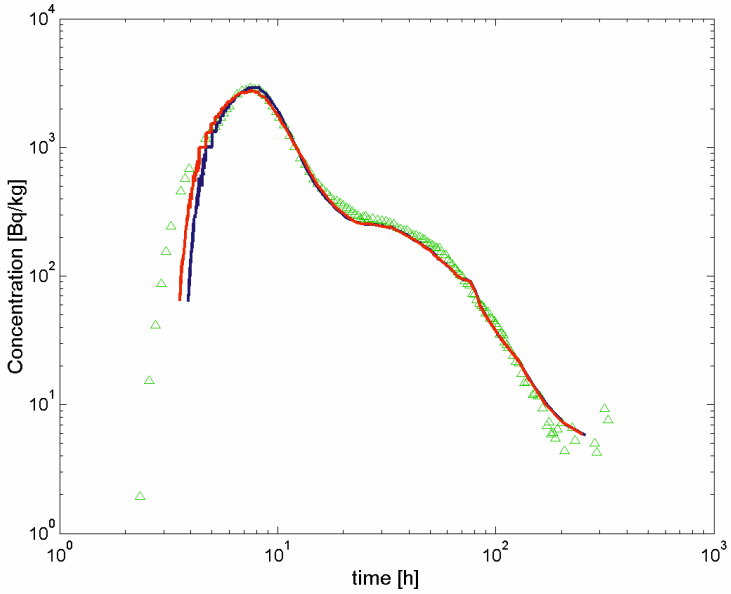

Figure 60 *Breakthrough concentration-time profile for ^{131}I. The simulated results are given as the mean of 100 realisations. Results for 3DQ1 simulations are shown as a blue curve. Results for 3DQ1b simulations are shown as a red curve. Triangular markers indicate experimental data for the STT1b test.*

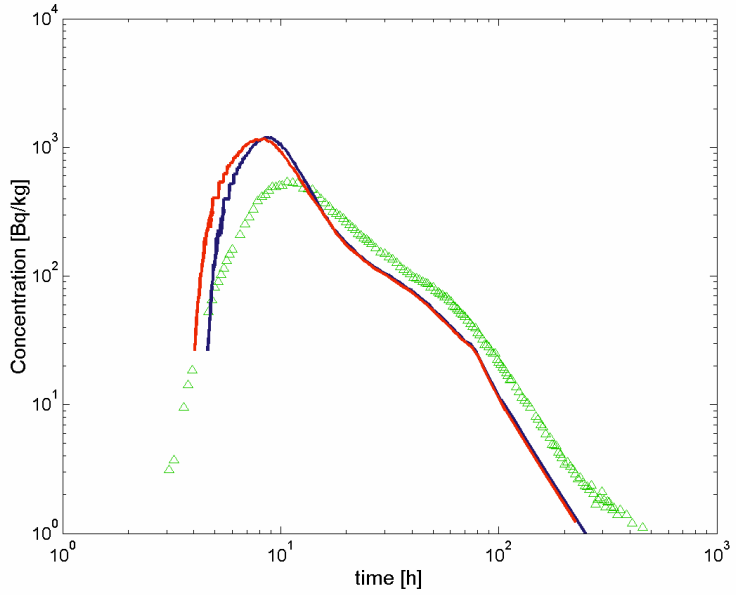

Figure 61 *Breakthrough concentration-time profile for ^{85}Sr. The simulated results are given as the mean of 100 realisations. Results for 3DQ1 simulations are shown as a blue curve. Results for 3DQ1b simulations are shown as a red curve. Triangular markers indicate experimental data for the STT1b test.*

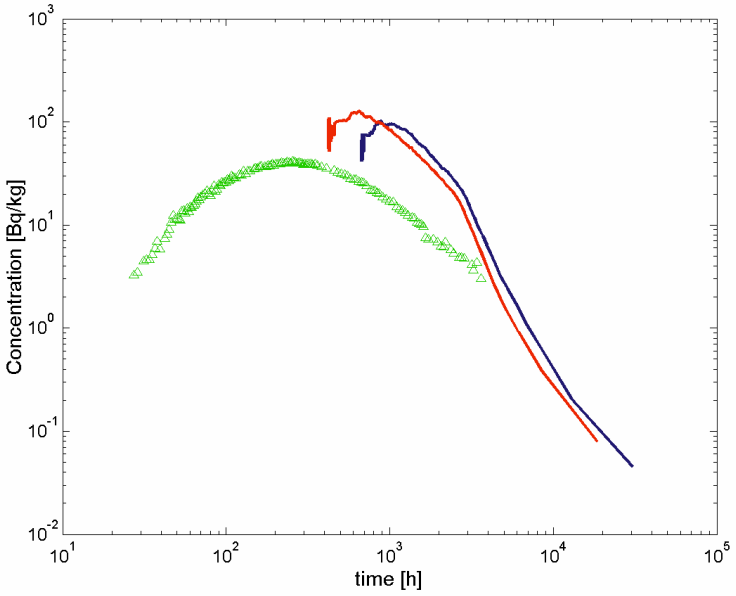

Figure 62 *Breakthrough concentration-time profile for ^{58}Co. The simulated results are given as the mean of 100 realisations. Results for 3DQ1 simulations are shown as a blue curve. Results for 3DQ1b simulations are shown as a red curve. Triangular markers indicate experimental data for the STT1b test.*

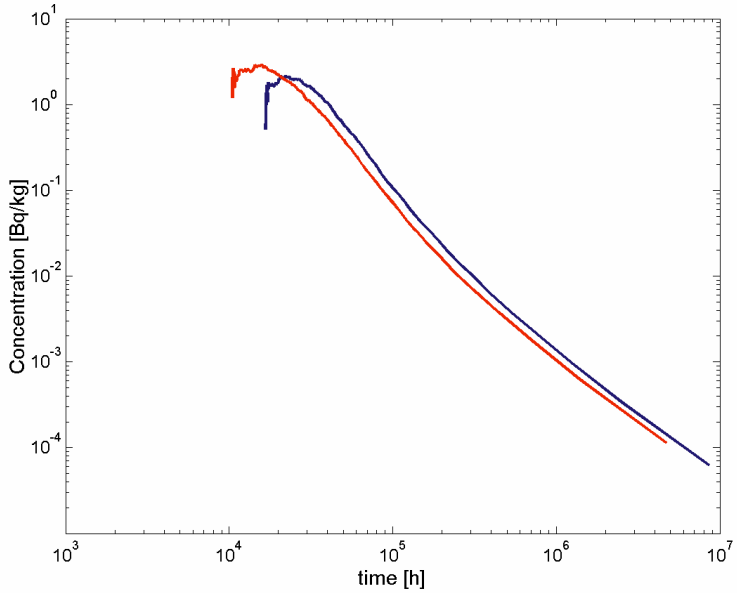

Figure 63 *Breakthrough concentration-time profile for ^{99}Tc. The simulated results are given as the mean of 100 realisations. Results for 3DQ1 simulations are shown as a blue curve. Results for 3DQ1b simulations are shown as a red curve.*

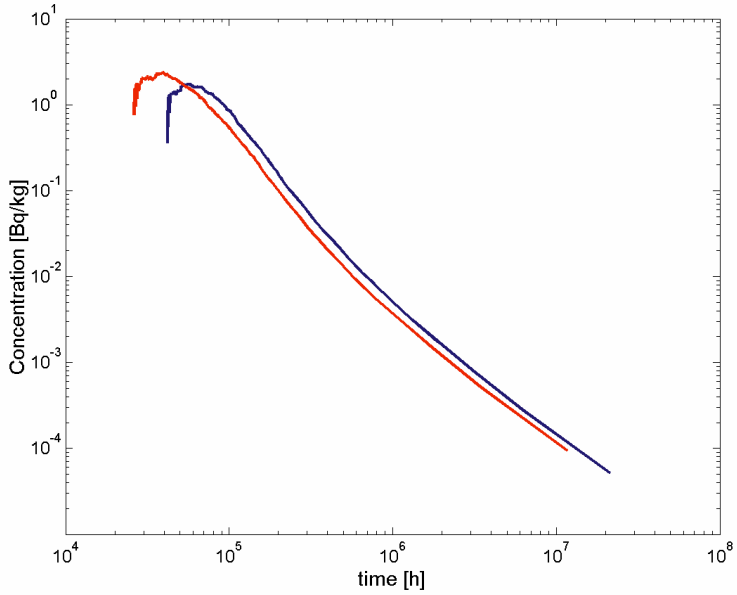

Figure 64 *Breakthrough concentration-time profile for ^{241}Am. The simulated results are given as the mean of 100 realisations. Results for 3DQ1 simulations are shown as a blue curve. Results for 3DQ1b simulations are shown as a red curve.*

Breakthrough time summary for modelled tracers (3DQ1b)

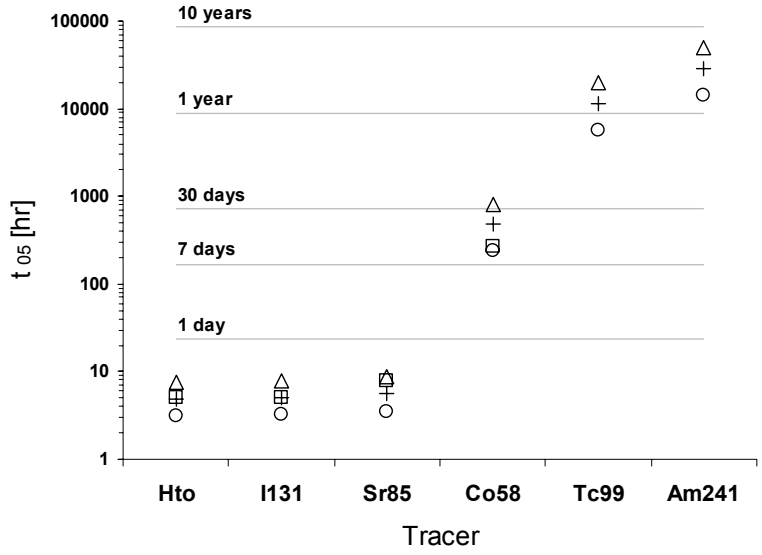

Figure 65 *Breakthrough times for 5% (t_{05}) of the injected tracer (3DQ1b). 5% (circles), 50% (+ symbols), and 95% (triangles) percentile levels are shown for the simulated results. Experimental results (squares) are shown for Hto, ^{131}I, ^{85}Sr, and ^{58}Co.*

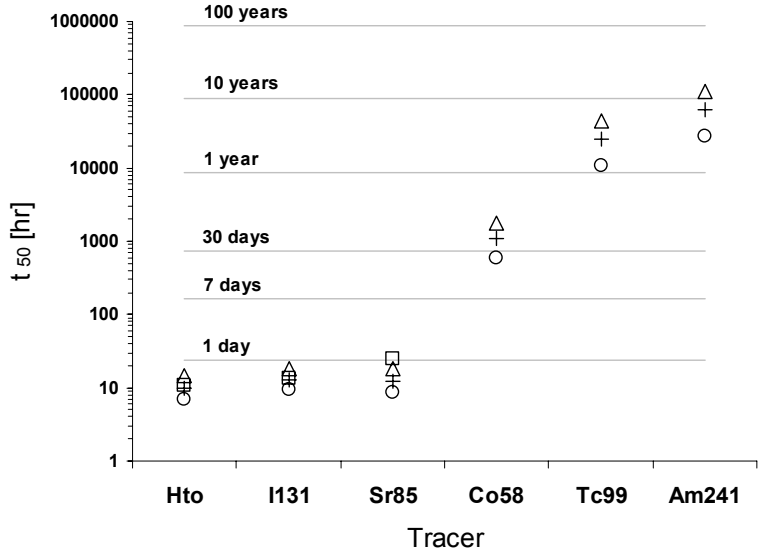

Figure 66 *Breakthrough times for 50% (t_{50}) of the injected tracer (3DQ1b). 5% (circles), 50% (+ symbols), and 95% (triangles) percentile levels are shown for the simulated results. Experimental results (squares) are shown for Hto, ^{131}I, ^{85}Sr, and ^{58}Co.*

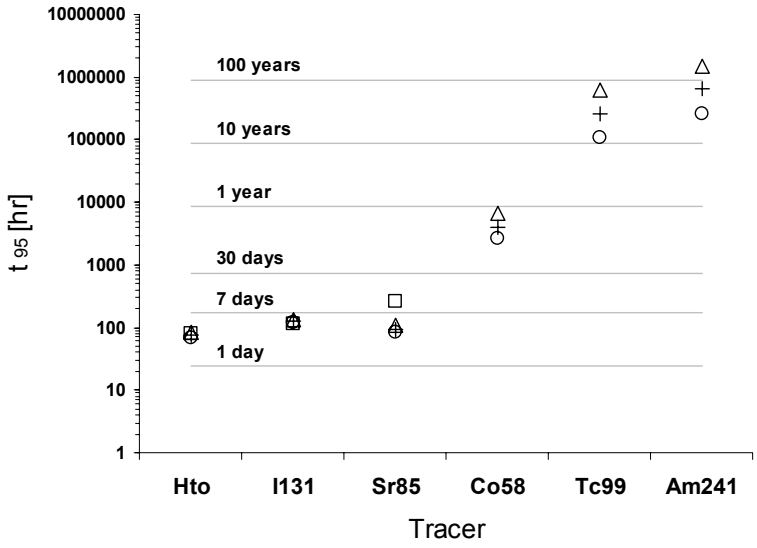

Figure 67 *Breakthrough times for 95% (t_{95}) of the injected tracer (3DQ1b). 5% (circles), 50% (+ symbols), and 95% (triangles) percentile levels are shown for the simulated results. Experimental results (squares) are shown for Hto, ^{131}I, ^{85}Sr, and ^{58}Co.*

2D simulations using experimental tracer injection data (2DQ1)

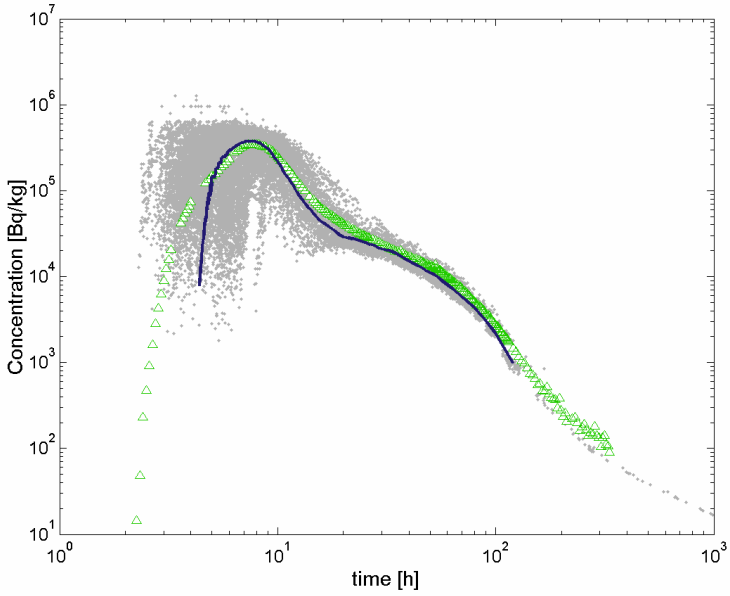

Figure 68 *Breakthrough concentration-time profile for Hto (2DQ1). The simulated results are shown as a probability density map (composite of 100 realisations). Mean of simulated results is shown as a blue curve. Triangular markers indicate experimental data for the STT1b test.*

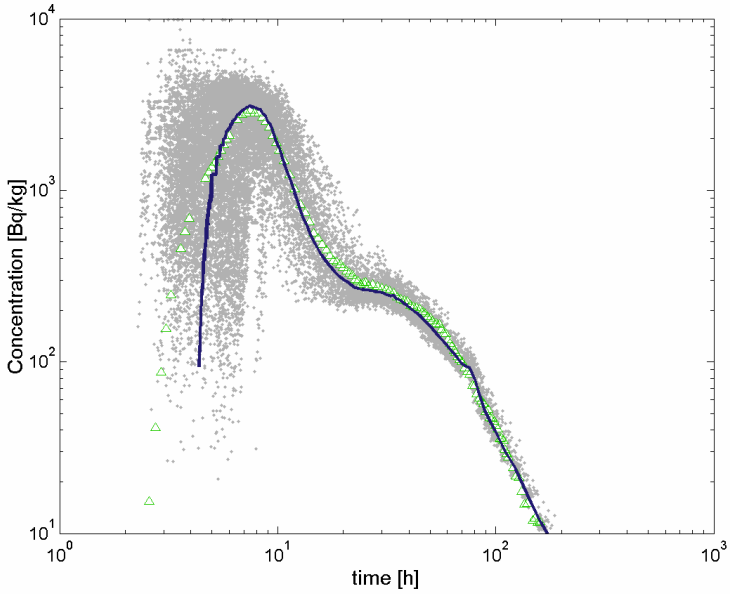

Figure 69 *Breakthrough concentration-time profile for ^{131}I (2DQ1. The simulated results are shown as a probability density map (composite of 100 realisations). Mean of simulated results is shown as a blue curve. Triangular markers indicate experimental data for the STT1b test.*

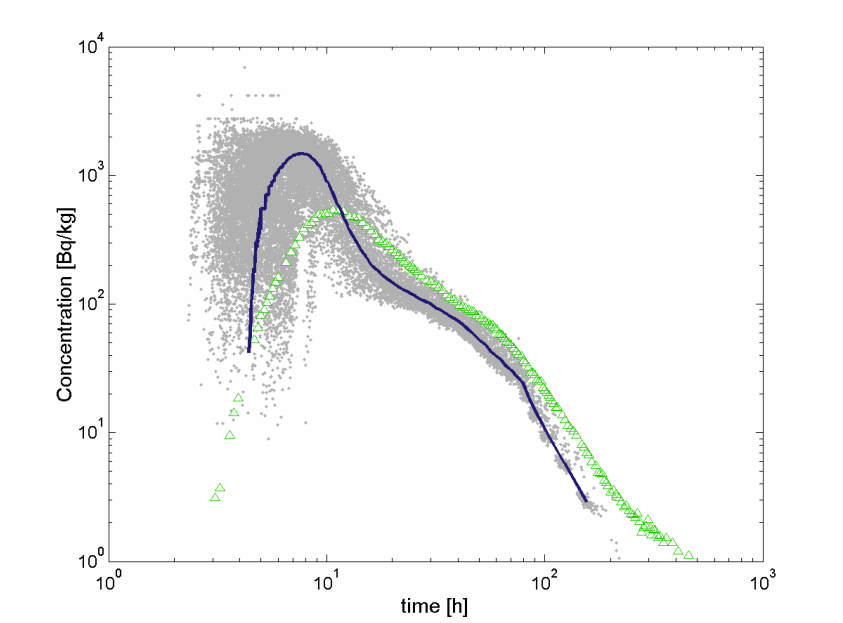

Figure 70 *Breakthrough concentration-time profile for ^{85}Sr (2DQ1). The simulated results are shown as a probability density map (composite of 100 realisations). Mean of simulated results is shown as a blue curve. Triangular markers indicate experimental data for the STT1b test.*

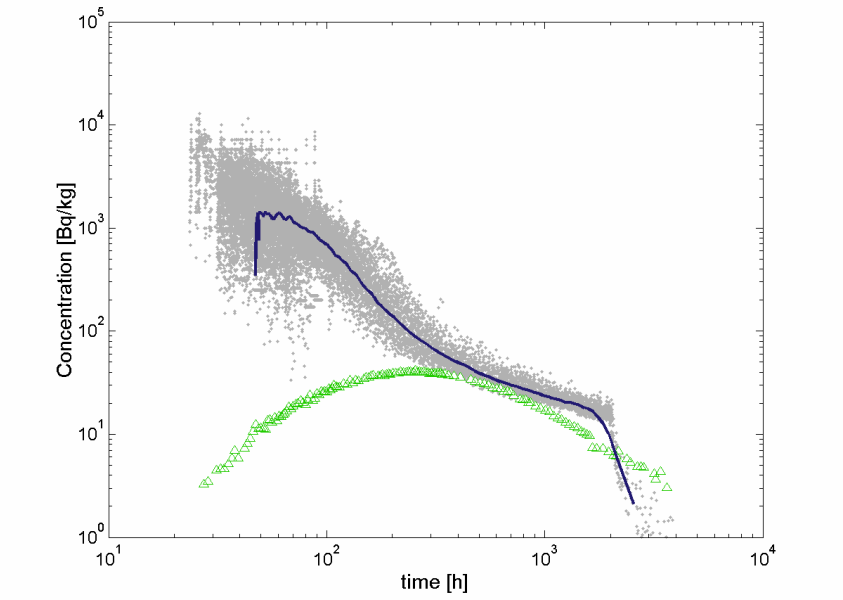

Figure 71 *Breakthrough concentration-time profile for ^{58}Co (2DQ1). The simulated results are shown as a probability density map (composite of 100 realisations). Mean of simulated results is shown as a blue curve. Triangular markers indicate experimental data for the STT1b test.*

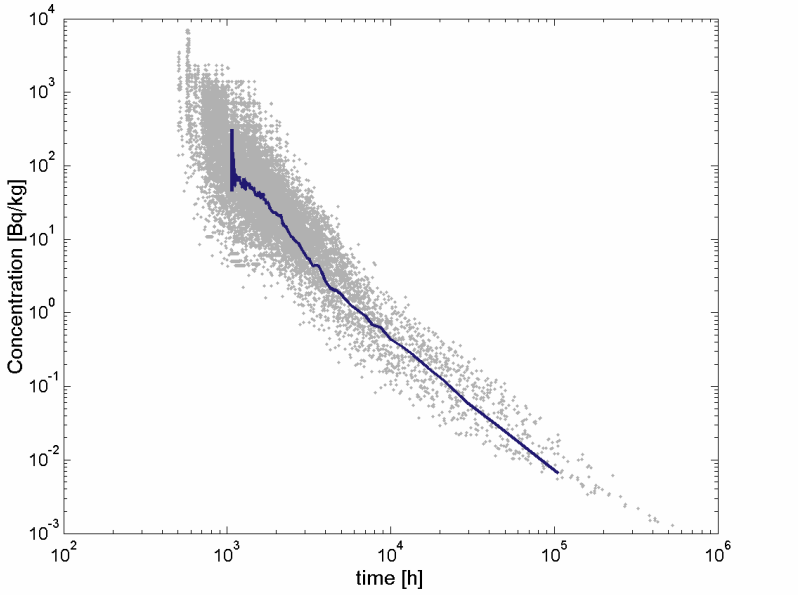

Figure 72 *Breakthrough concentration-time profile for ^{99}Tc (2DQ1). The simulated results are shown as a probability density map (composite of 100 realisations). Mean of simulated results is shown as a blue curve.*

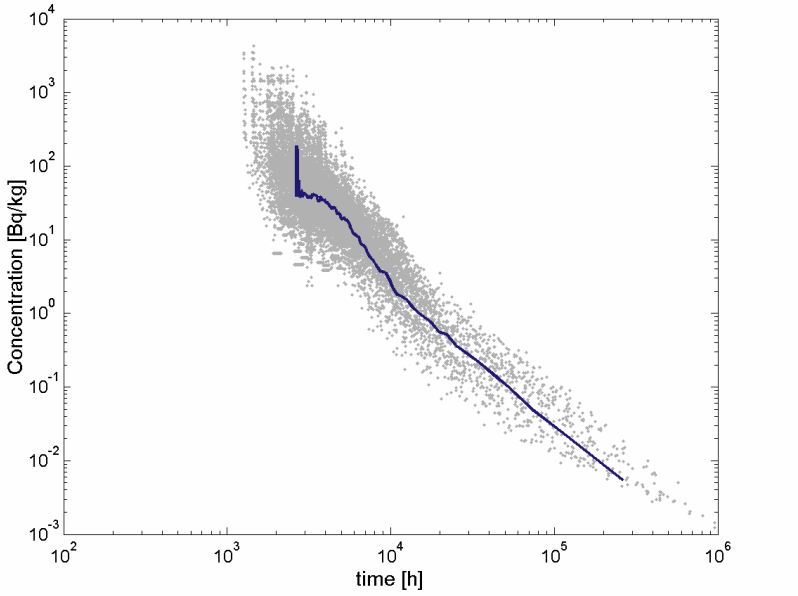

Figure 73 *Breakthrough concentration-time profile for ^{241}Am (2DQ1). The simulated results are shown as a probability density map (composite of 100 realisations). Mean of simulated results is shown as a blue curve.*

Breakthrough time summary for modelled tracers (2DQ1)

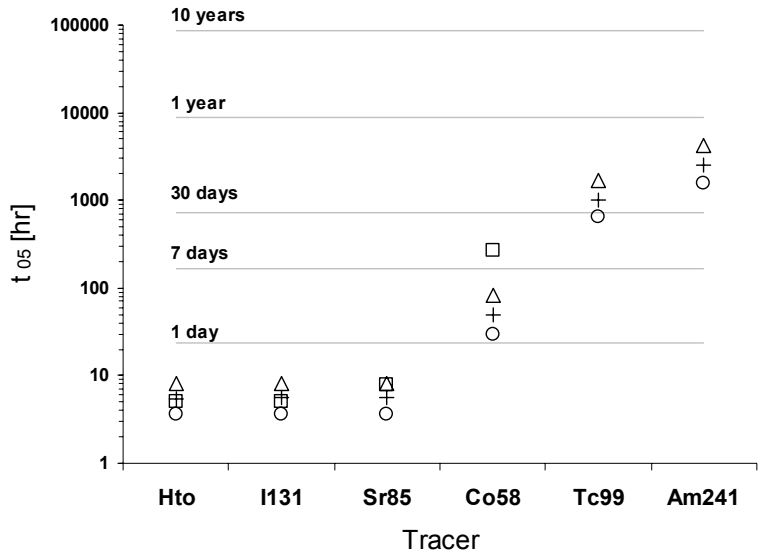

Figure 74 *Breakthrough times for 5% (t_{05}) of the injected tracer (2DQ1). 5% (circles), 50% (+ symbols), and 95% (triangles) percentile levels are shown for the simulated results. Experimental results (squares) are shown for Hto, ^{131}I, ^{85}Sr, and ^{58}Co.*

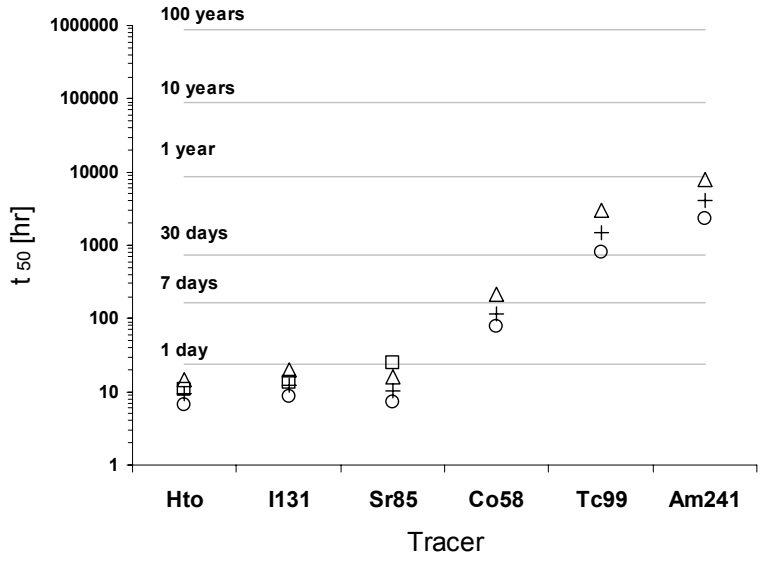

Figure 75 *Breakthrough times for 50% (t_{50}) of the injected tracer (2DQ1). 5% (circles), 50% (+ symbols), and 95% (triangles) percentile levels are shown for the simulated results. Experimental results (squares) are shown for Hto, ^{131}I, ^{85}Sr, and ^{58}Co.*

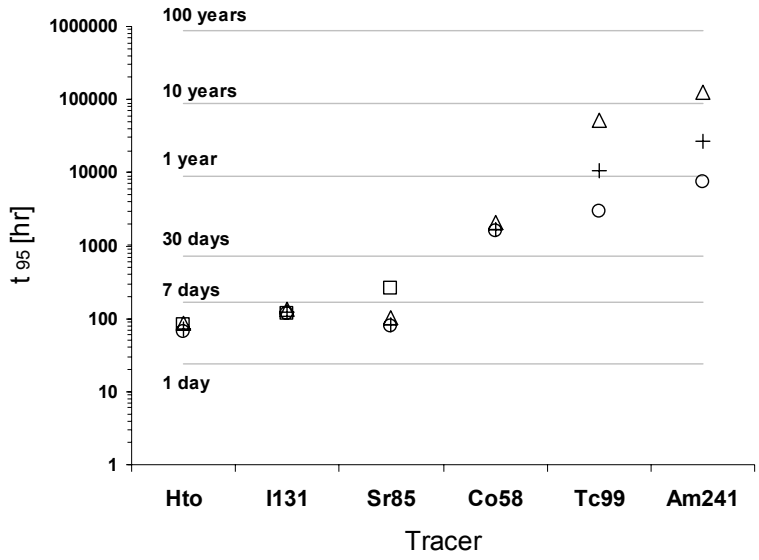

Figure 76 *Breakthrough times for 95% (t_{95}) of the injected tracer (2DQ1). 5% (circles), 50% (+ symbols), and 95% (triangles) percentile levels are shown for the simulated results. Experimental results (squares) are shown for Hto, ^{131}I, ^{85}Sr, and ^{58}Co.*

Maximum nuclide release rate (2DQ1)

Table 7 Maximum nuclide release rate [Bq/y] for simulation series 2DQ1. Results are given for experimental breakthrough data, simulated injection pulse data, and for Dirac pulse data. Simulation data is based upon mean peak breakthrough concentration for 100 realisations.

Tracer	Exp-M_R [Bq/y]	M_R [Bq/y]	Dirac-M_R [Bq/y]
Hto	7.31×10^{10}	3.78×10^{9}	1.37×10^{10}
^{131}I	6.13×10^{8}	3.02×10^{9}	1.32×10^{10}
^{85}Sr	1.13×10^{8}	3.42×10^{9}	2.54×10^{10}
^{58}Co	8.78×10^{6}	3.11×10^{8}	1.33×10^{10}
^{99}Tc	n/a	1.17×10^{8}	2.14×10^{8}
^{241}Am	n/a	2.79×10^{7}	9.32×10^{7}

Comparison of injection pulse data and Dirac pulse arrival times (2DQ1)

Table 8 **Mean travel time (t_{05}), standard deviation (σ_{t05}), and Z-statistic for comparison between experimental injection data and Dirac pulse boundary condition. Data is for 2DQ1 simulation series.**

Tracer	t_{05} [h]	σ_{t05}	Dirac-t_{05} [h]	Dirac-σ_{t05}	Z-statistic
Hto	5.6	1.5	4.4	1.3	6.2
^{131}I	5.8	1.5	4.4	1.3	6.9
^{85}Sr	5.8	1.5	4.5	1.3	6.4
^{58}Co	53	17	48	15	2.2
^{99}Tc	1.10×10^{3}	361	1.10×10^{3}	360	0.1
^{241}Am	2.79×10^{3}	929	2.72×10^{3}	896	0.5

Table 9 **Mean travel time (t_{50}), standard deviation (σ_{t50}), and Z-statistic for comparison between experimental injection data and Dirac pulse boundary condition. Data is for 2DQ1 simulation series.**

Tracer	t_{50} [h]	σ_{t50}	Dirac-t_{50} [h]	Dirac-σ_{t50}	Z-statistic
Hto	10.1	2.6	6.1	2.0	12.4
^{131}I	13.3	3.5	6.1	2.0	17.5
^{85}Sr	11.1	2.9	6.2	2.0	13.9
^{58}Co	130	42	73	28	11.5
^{99}Tc	1.73×10^{3}	687	1.73×10^{3}	688	0.1
^{241}Am	4.65×10^{3}	1.68×10^{3}	4.31×10^{3}	1.72×10^{3}	1.4

Table 10 **Mean travel time (t_{95}), standard deviation (σ_{t95}), and Z-statistic for comparison between experimental injection data and Dirac pulse boundary condition. Data is for 2DQ1 simulation series.**

Tracer	t_{95} [h]	σ_{t95}	Dirac-t_{95} [h]	Dirac-σ_{t95}	Z-statistic
Hto	74	6	19	11	44
^{131}I	123	6	19	11	84
^{85}Sr	85	7	20	12	47
^{58}Co	1.75×10^{3}	164	489	453	26
^{99}Tc	1.66×10^{4}	1.60×10^{4}	1.66×10^{4}	1.60×10^{4}	0.0
^{241}Am	4.17×10^{4}	4.00×10^{4}	4.15×10^{4}	4.00×10^{4}	0.0

Comparison of 2D simulations (using experimental tracer injection data) with high and low injection flow criterion – 2DQ1 & 2DQ1b

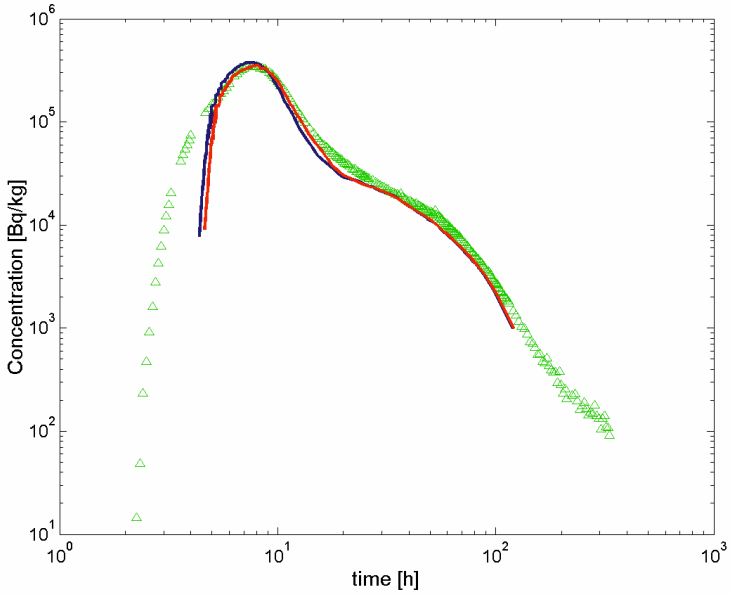

Figure 77 *Breakthrough concentration-time profile for Hto. The simulated results are given as the mean of 100 realisations. Results for 2DQ1 simulations are shown as a blue curve. Results for 2DF1b simulations are shown as a red curve. Triangular markers indicate experimental data for the STT1b test.*

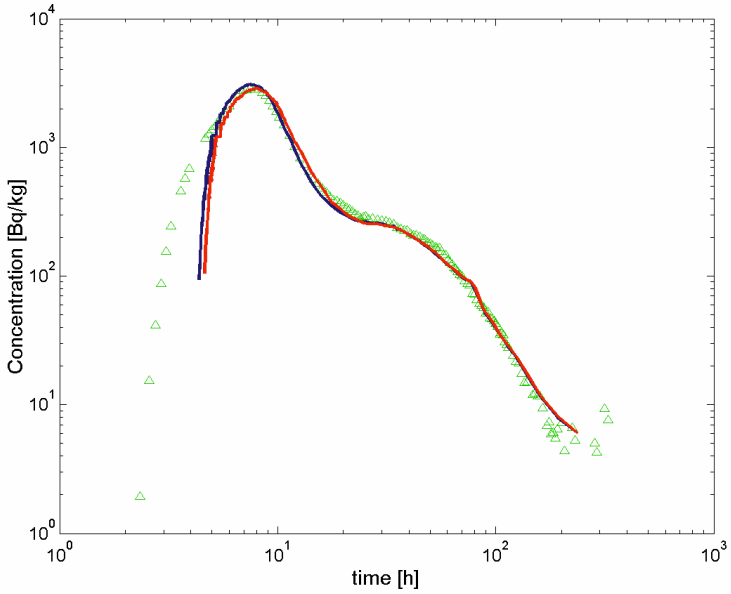

Figure 78 *Breakthrough concentration-time profile for ^{131}I. The simulated results are given as the mean of 100 realisations. Results for 2DQ1 simulations are shown as a blue curve. Results for 2DQ1b simulations are shown as a red curve. Triangular markers indicate experimental data for the STT1b test.*

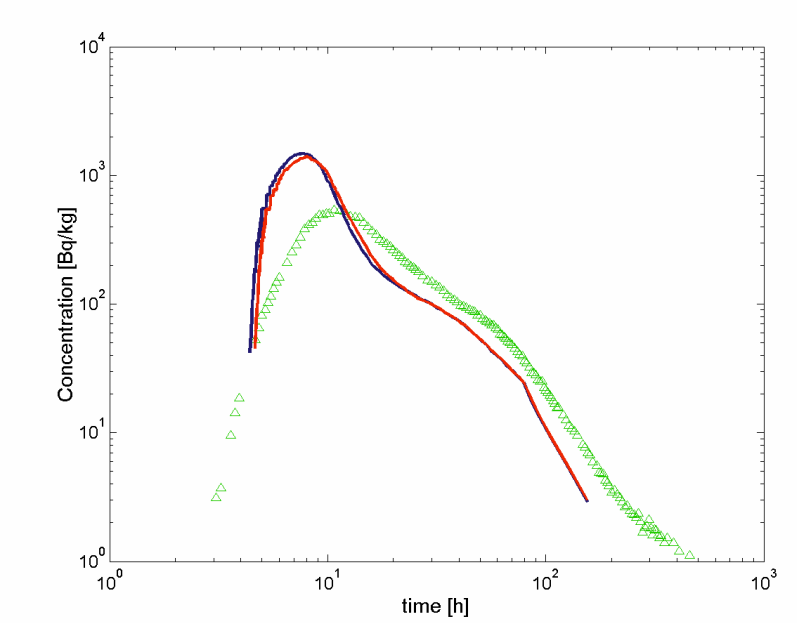

Figure 79 *Breakthrough concentration-time profile for ^{85}Sr. The simulated results are given as the mean of 100 realisations. Results for 2DQ1 simulations are shown as a blue curve. Results for 2DQ1b simulations are shown as a red curve. Triangular markers indicate experimental data for the STT1b test.*

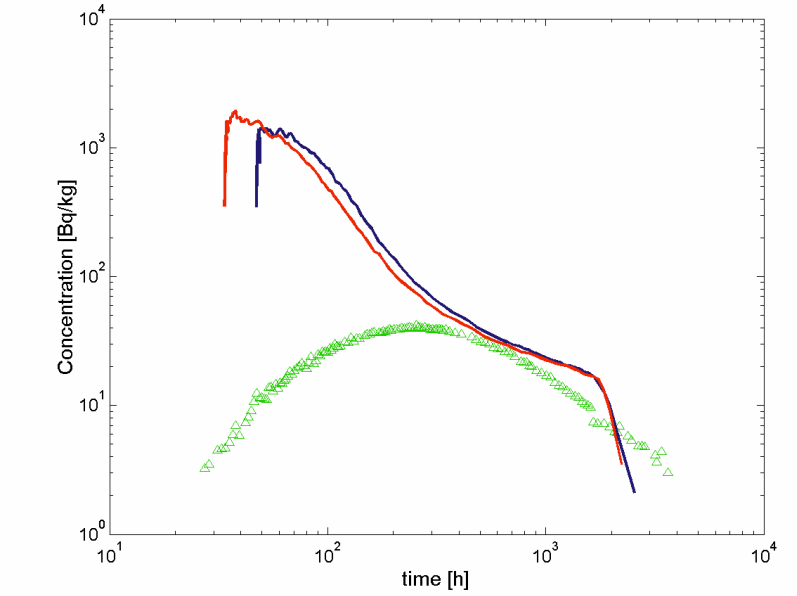

Figure 80 *Breakthrough concentration-time profile for ^{58}Co. The simulated results are given as the mean of 100 realisations. Results for 2DQ1 simulations are shown as a blue curve. Results for 2DQ1b simulations are shown as a red curve. Triangular markers indicate experimental data for the STT1b test.*

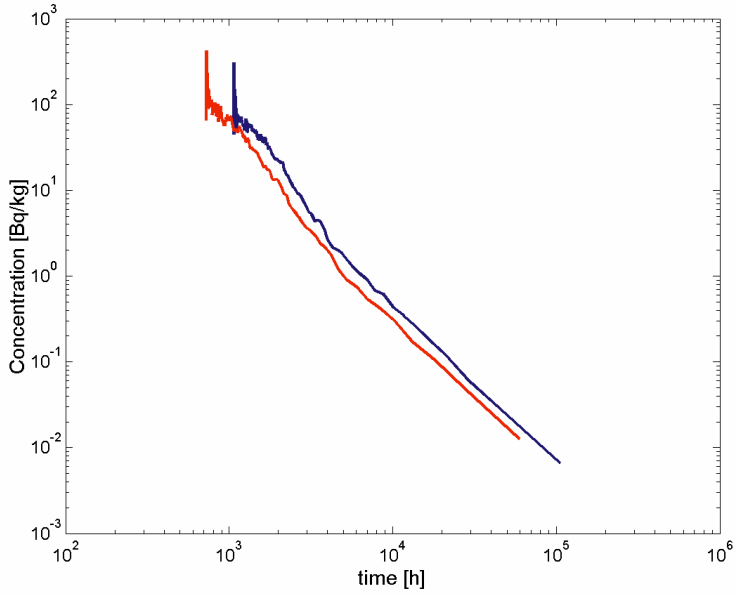

Figure 81 *Breakthrough concentration-time profile for ^{99}Tc. The simulated results are given as the mean of 100 realisations. Results for 2DQ1 simulations are shown as a blue curve. Results for 2DQ1b simulations are shown as a red curve.*

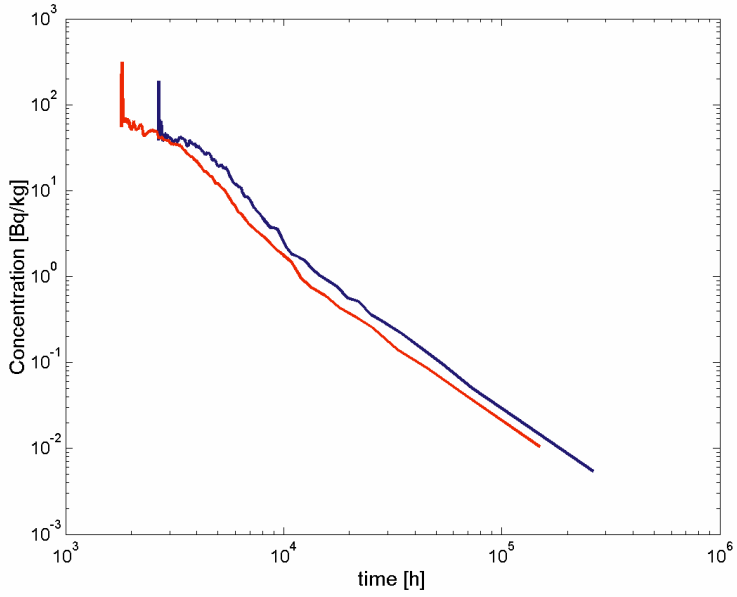

Figure 82 *Breakthrough concentration-time profile for ^{241}Am. The simulated results are given as the mean of 100 realisations. Results for 2DQ1 simulations are shown as a blue curve. Results for 2DQ1b simulations are shown as a red curve.*

Breakthrough time summary for modelled tracers (2DQ1b)

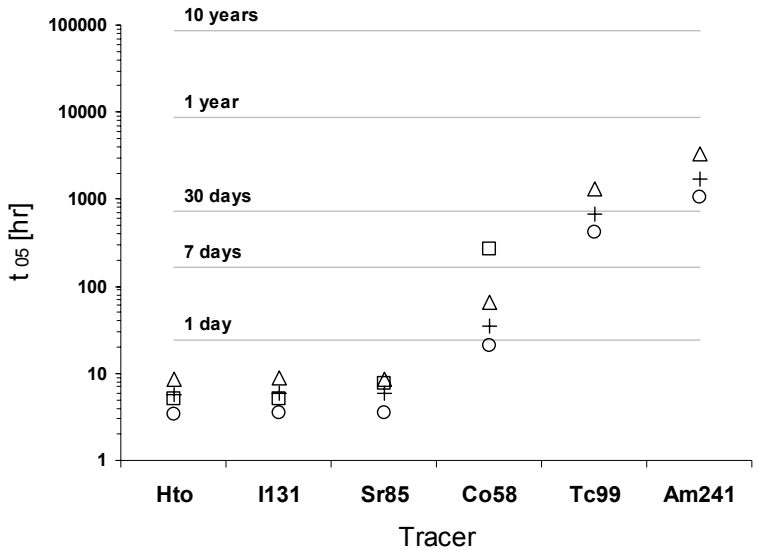

Figure 83 *Breakthrough times for 5% (t_{05}) of the injected tracer (2DQ1b). 5% (circles), 50% (+ symbols), and 95% (triangles) percentile levels are shown for the simulated results. Experimental results (squares) are shown for Hto, ^{131}I, ^{85}Sr, and ^{58}Co.*

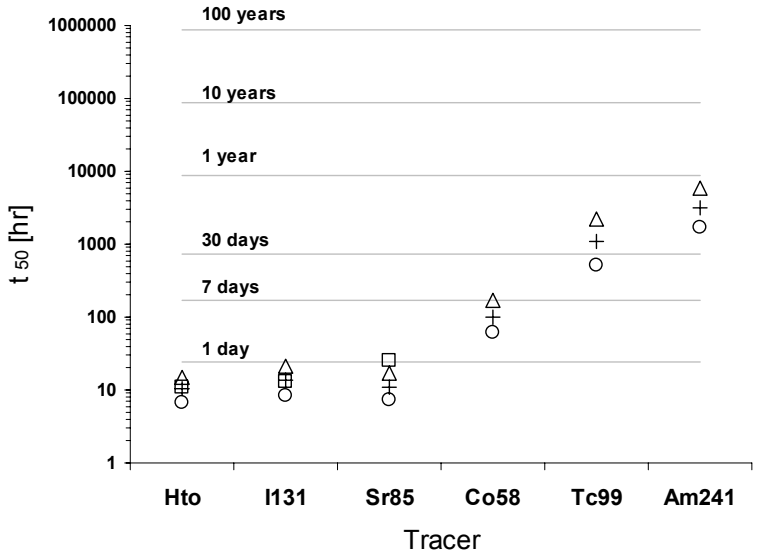

Figure 84 *Breakthrough times for 50% (t_{50}) of the injected tracer (2DQ1b). 5% (circles), 50% (+ symbols), and 95% (triangles) percentile levels are shown for the simulated results. Experimental results (squares) are shown for Hto, ^{131}I, ^{85}Sr, and ^{58}Co.*

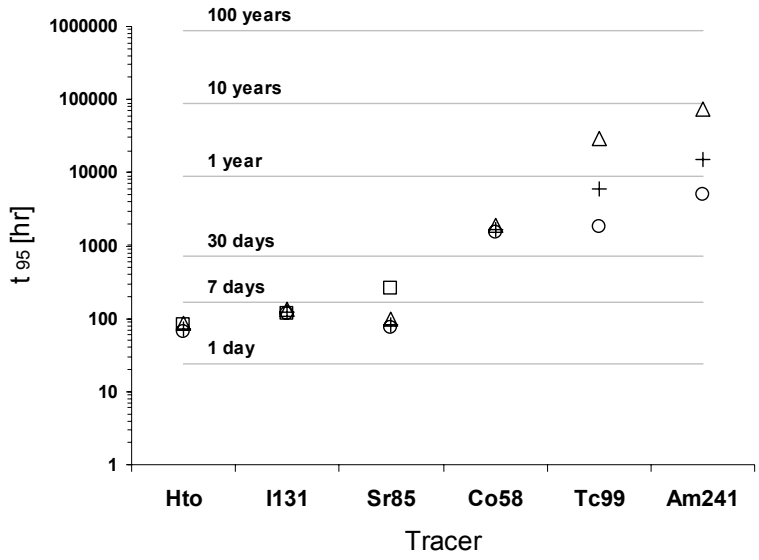

Figure 85 *Breakthrough times for 95% (t_{95}) of the injected tracer (2DQ1b). 5% (circles), 50% (+ symbols), and 95% (triangles) percentile levels are shown for the simulated results. Experimental results (squares) are shown for Hto, ^{131}I, ^{85}Sr, and ^{58}Co.*

Comparison of 2D & 3D simulations (using experimental tracer injection data) – 3DQ1, 2DQ1

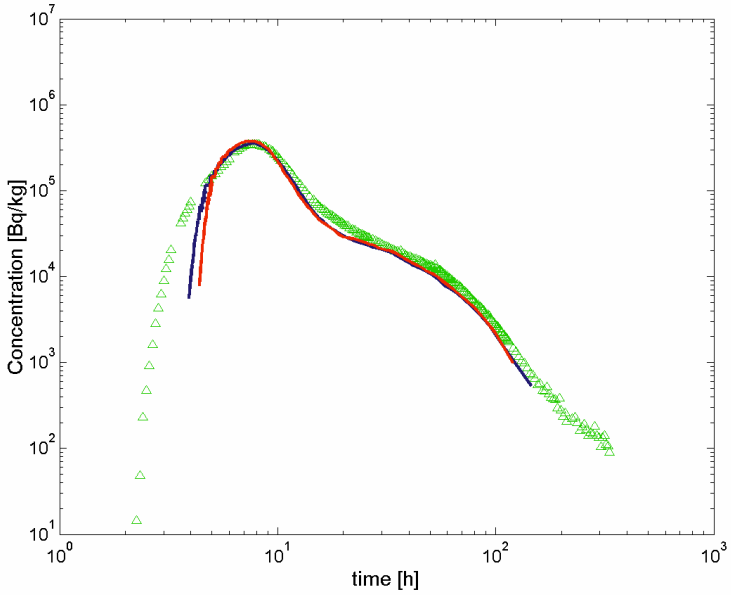

Figure 86 *Breakthrough concentration-time profiles for Hto. The blue curve shows data for 3D simulations (3DQ1). The red curve indicates data for 2D simulations (2DQ1). Triangular, green markers indicate experimental data for the STT1b test.*

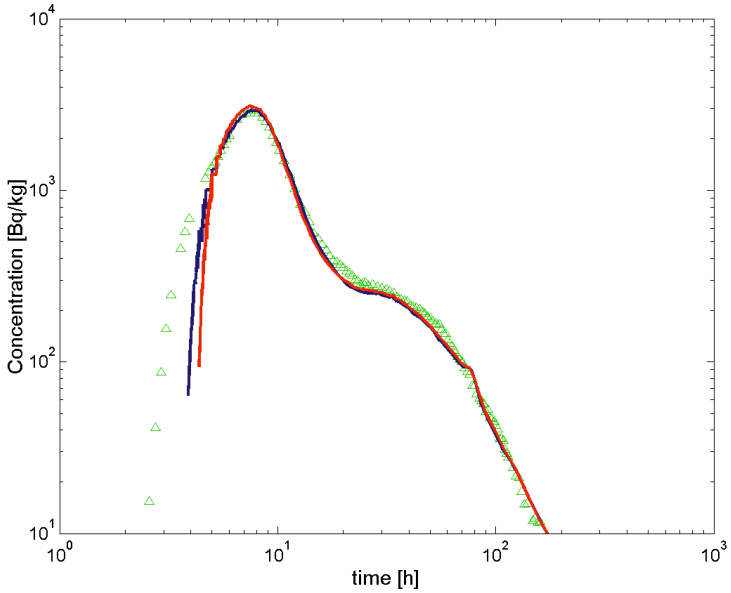

Figure 87 *Breakthrough concentration-time profile for ^{131}I. The blue curve shows data for 3D simulations (3DQ1). The red curve indicates data for 2D simulations (2DQ1). Triangular, green markers indicate experimental data for the STT1b test.*

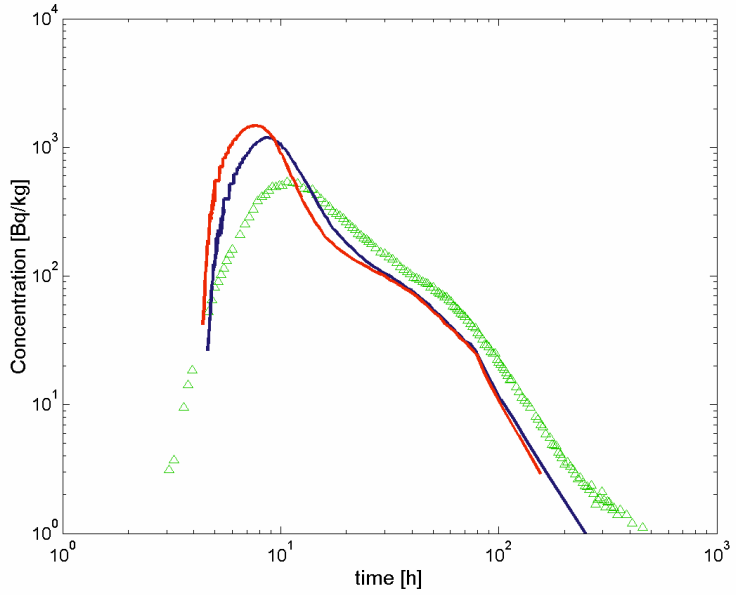

Figure 88 *Breakthrough concentration-time profile for ^{85}Sr. The blue curve shows data for 3D simulations (3DQ1). The red curve indicates data for 2D simulations (2DQ1). Triangular, green markers indicate experimental data for the STT1b test.*

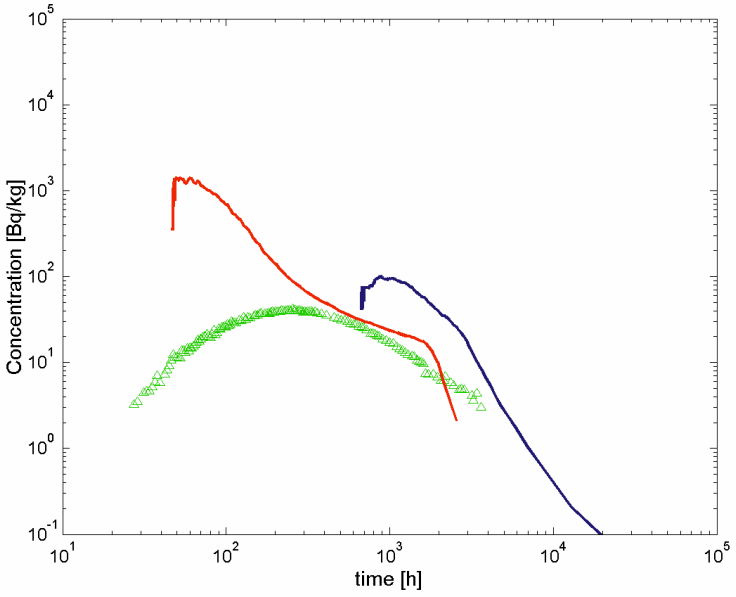

Figure 89 *Breakthrough concentration-time profile for ^{58}Co. The blue curve shows data for 3D simulations (3DQ1). The red curve indicates data for 2D simulations (2DQ1). Triangular, green markers indicate experimental data for the STT1b test.*

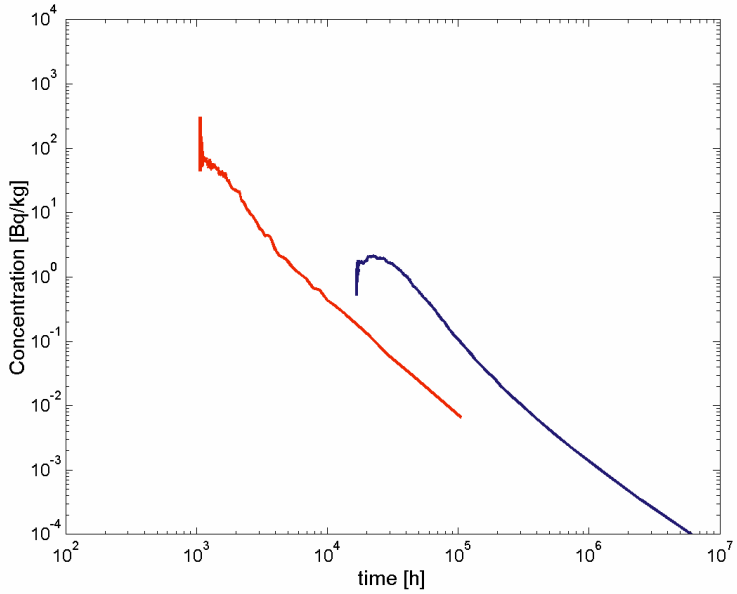

Figure 90 *Breakthrough concentration-time profile for ^{99}Tc. The blue curve shows data for 3D simulations (3DQ1). The red curve indicates data for 2D simulations (2DQ1).*

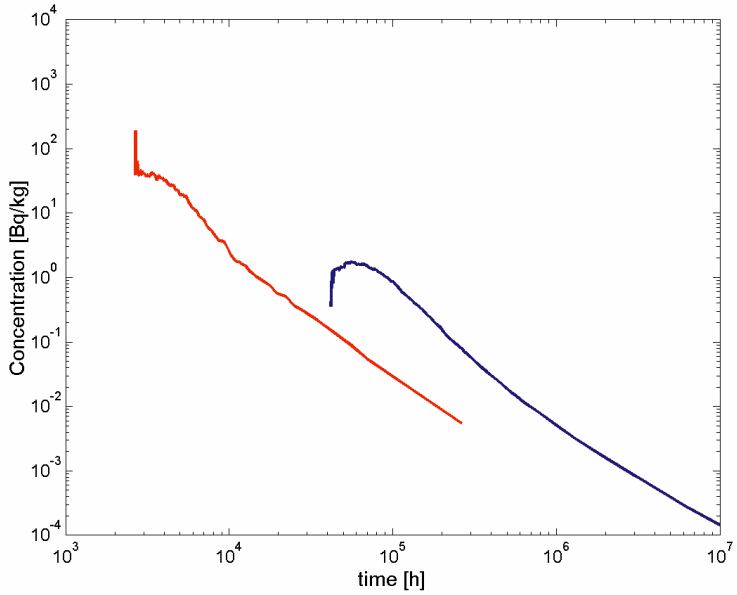

Figure 91 *Breakthrough concentration-time profile for ^{241}Am. The blue curve shows data for 3D simulations (3DQ1). The red curve indicates data for 2D simulations (2DQ1).*

Comparison of 2D & 3D simulations (Dirac Pulse) – 3DQ1, 2DQ1

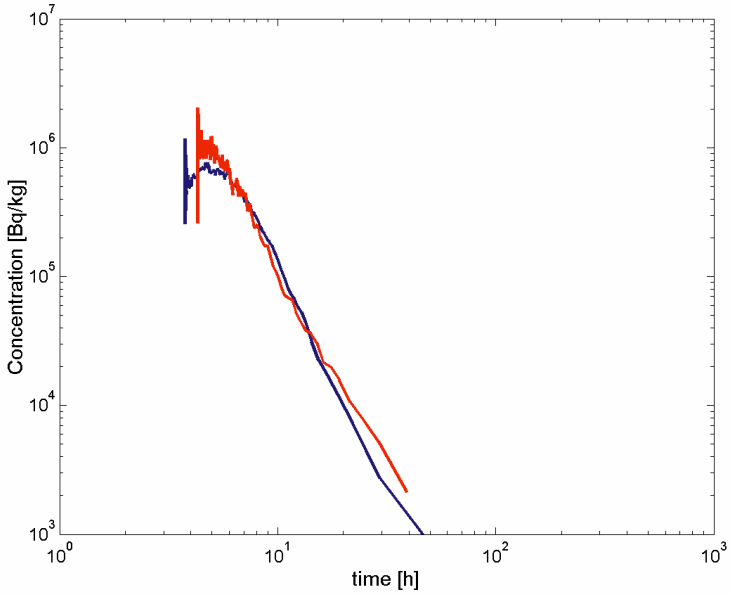

Figure 92 *Breakthrough concentration-time profile for Hto Dirac pulse. The blue curve shows data for 3D simulations (3DQ1). The red curve indicates data for 2D simulations (2DQ1).*

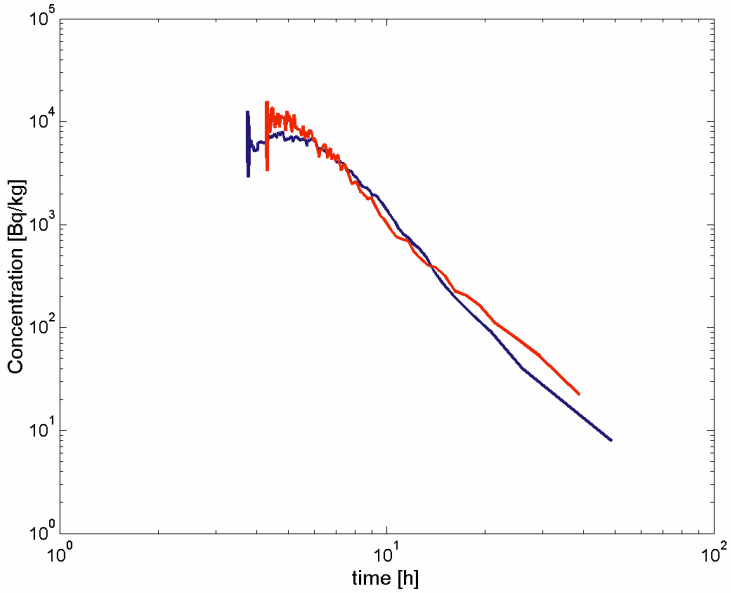

Figure 93 *Breakthrough concentration-time profile for ^{131}I Dirac pulse. The blue curve shows data for 3D simulations (3DQ1). The red curve indicates data for 2D simulations (2DQ1).*

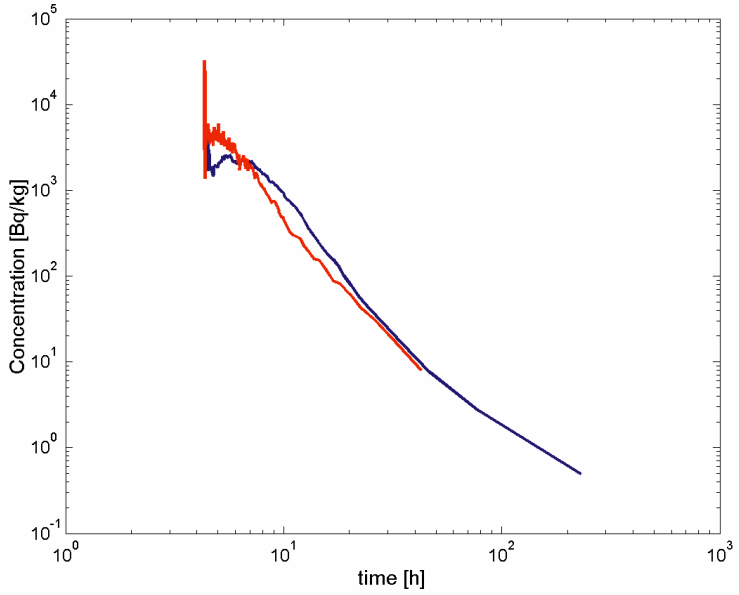

Figure 94 *Breakthrough concentration-time profile for ^{85}Sr Dirac pulse. The blue curve shows data for 3D simulations (3DQ1). The red curve indicates data for 2D simulations (2DQ1).*

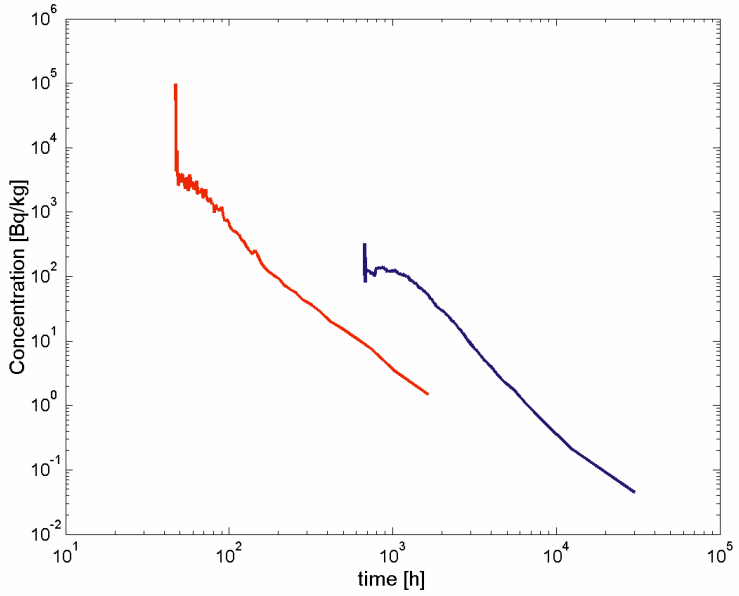

Figure 95 *Breakthrough concentration-time profile for ^{58}Co Dirac pulse. The blue curve shows data for 3D simulations (3DQ1). The red curve indicates data for 2D simulations (2DQ1).*

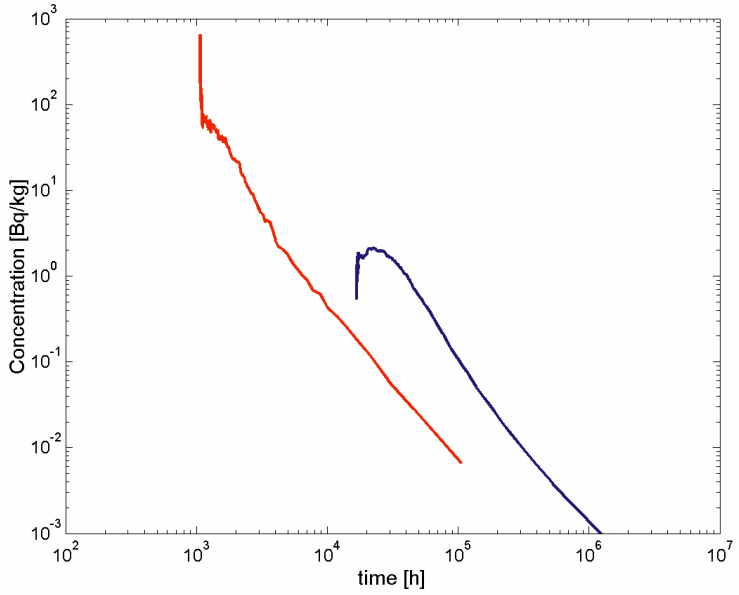

Figure 96 *Breakthrough concentration-time profile for ^{99}Tc Dirac pulse. The blue curve shows data for 3D simulations (3DQ1). The red curve indicates data for 2D simulations (2DQ1).*

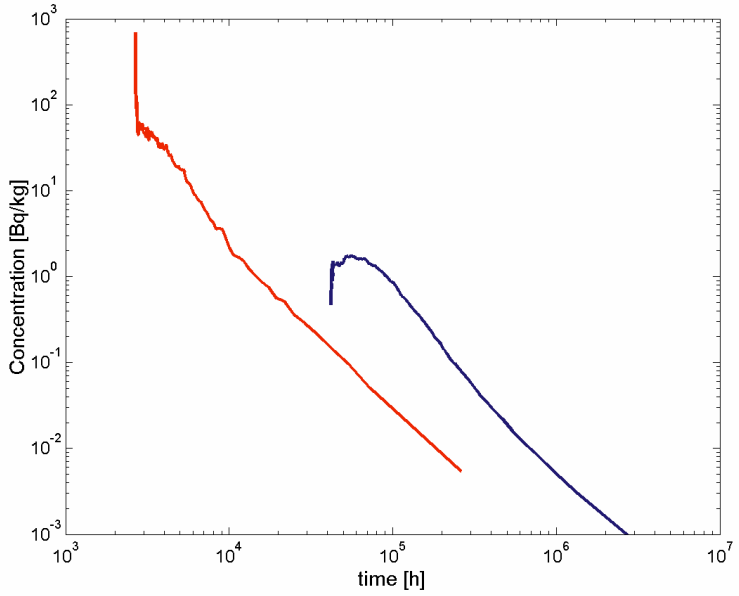

Figure 97 *Breakthrough concentration-time profile for ^{241}Am Dirac pulse. The blue curve shows data for 3D simulations (3DQ1). The red curve indicates data for 2D simulations (2DQ1).*

Appendix 3

Task 6B. Breakthrough Concentration-Time Curves (BTC)

- **Comparison of 2D & 3D simulations (Dirac pulse) – 3DQ2, 2DQ2**
- **Breakthrough time summary for modelled tracers (3DQ2)**
- **Maximum nuclide release rate (3DQ2)**
- **Comparison of Task 6A (3DQ1) and Task 6B (3DQ2) tracer arrival times**
- **Breakthrough time summary for modelled tracers (2DQ2)**
- **Maximum nuclide release rate (2DQ2)**
- **Comparison of Task 6A (2DQ1) and Task 6B (2DQ2) tracer arrival times**
- **Comparison of 2D & 3D simulations (constant injection) – 3DQ2, 2DQ2**

Comparison of 2D & 3D simulations (Dirac pulse) – 3DQ2, 2DQ2

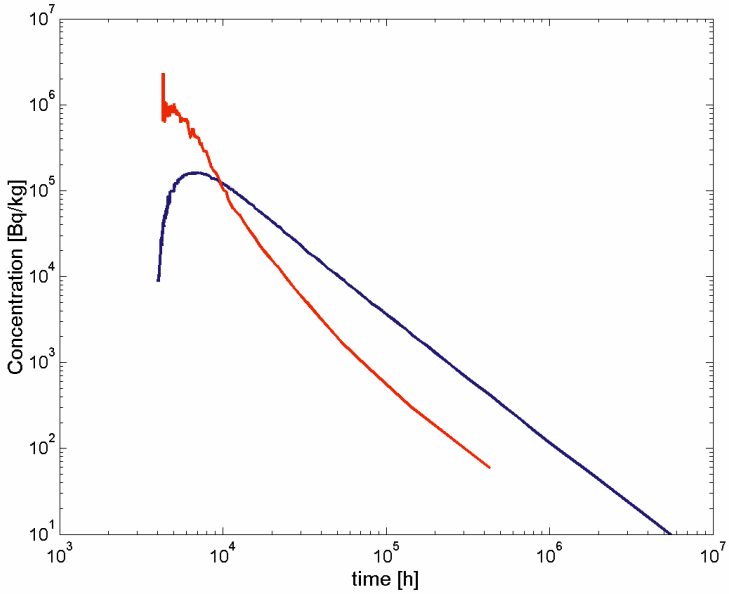

Figure 98 *Breakthrough concentration-time profile for Hto Dirac pulse. The blue curve shows data for 3D simulations (3DQ2). The red curve indicates data for 2D simulations (2DQ2).*

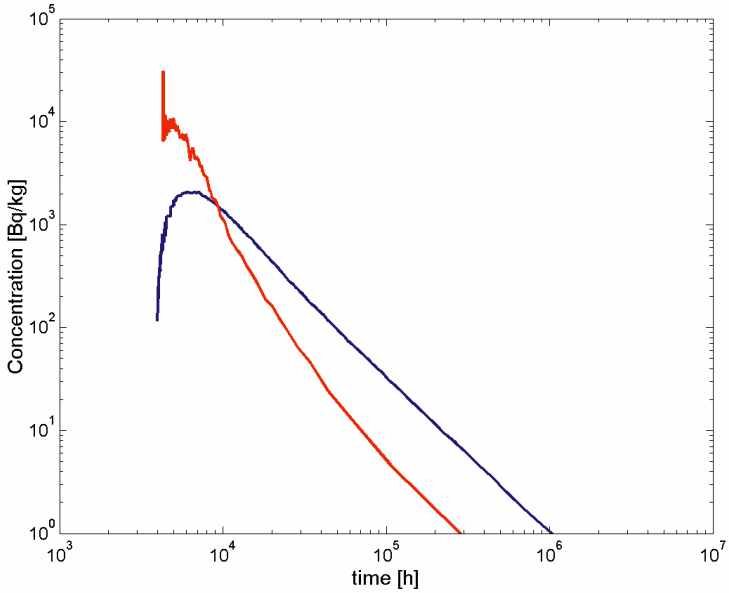

Figure 99 *Breakthrough concentration-time profile for ^{131}I Dirac pulse. The blue curve shows data for 3D simulations (3DQ2). The red curve indicates data for 2D simulations (2DQ2).*

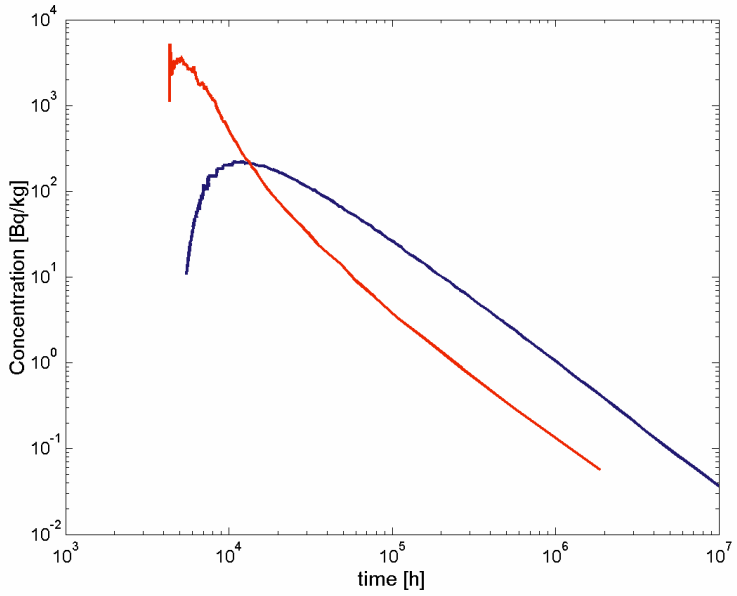

Figure 100 *Breakthrough concentration-time profile for ^{85}Sr Dirac pulse. The blue curve shows data for 3D simulations (3DQ2). The red curve indicates data for 2D simulations (2DQ2).*

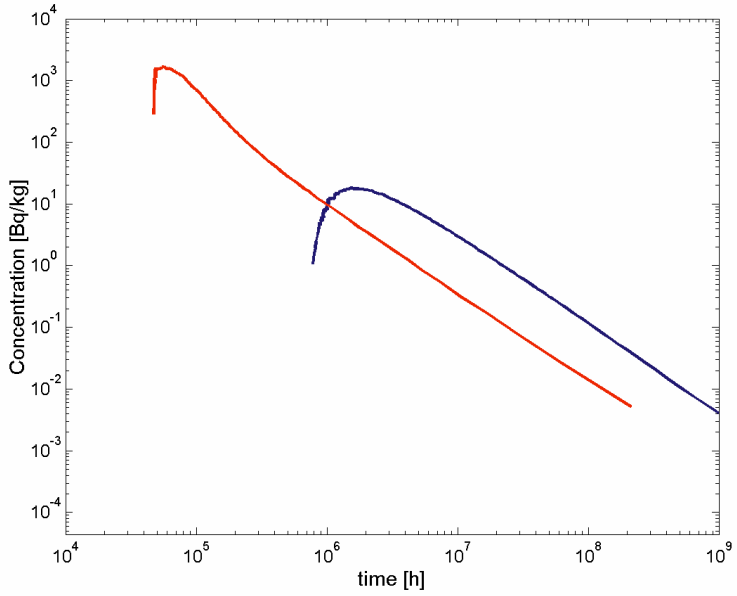

Figure 101 *Breakthrough concentration-time profile for ^{58}Co Dirac pulse. The blue curve shows data for 3D simulations (3DQ2). The red curve indicates data for 2D simulations (2DQ2).*

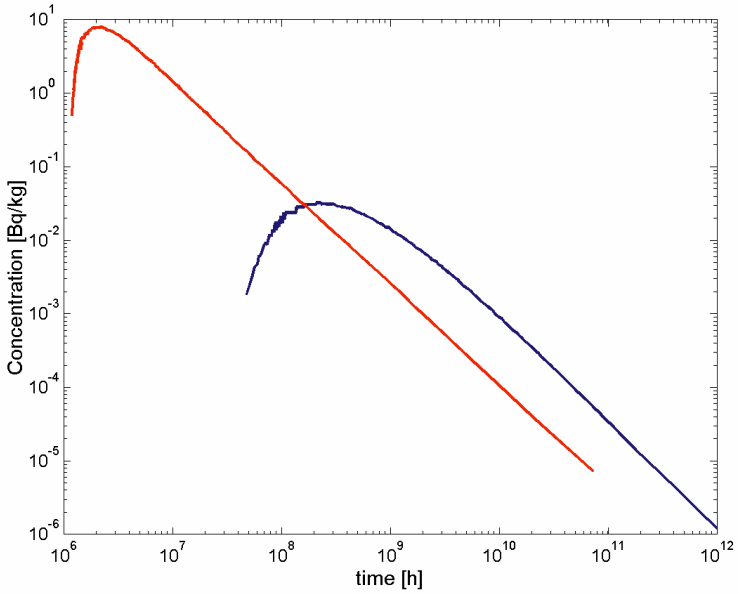

Figure 102 *Breakthrough concentration-time profile for ^{99}Tc Dirac pulse. The blue curve shows data for 3D simulations (3DQ2). The red curve indicates data for 2D simulations (2DQ2).*

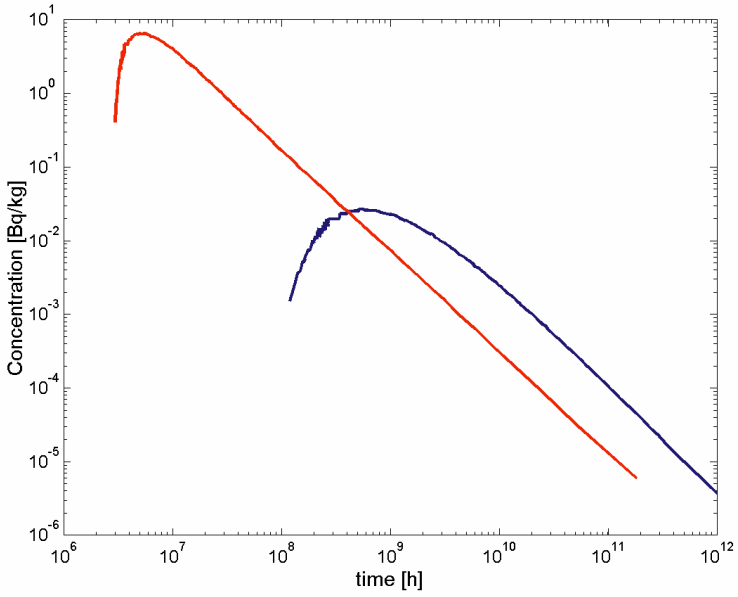

Figure 103 *Breakthrough concentration-time profile for ^{241}Am Dirac pulse. The blue curve shows data for 3D simulations (3DQ2). The red curve indicates data for 2D simulations (2DQ2).*

Breakthrough time summary for modelled tracers (3DQ2)

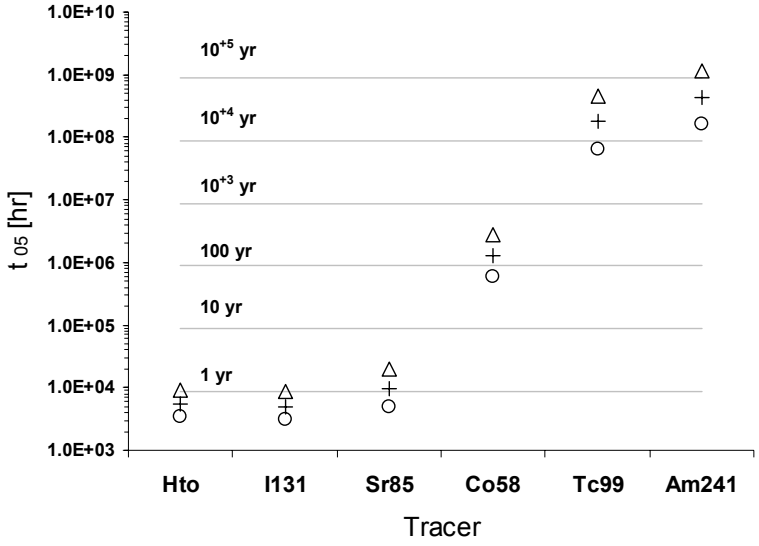

Figure 104 *Breakthrough times for 5% (t_{05}) of the Dirac pulse injected tracer (3DQ2). 5% (circles), 50% (+ symbols), and 95% (triangles) percentile levels are shown for the simulated results.*

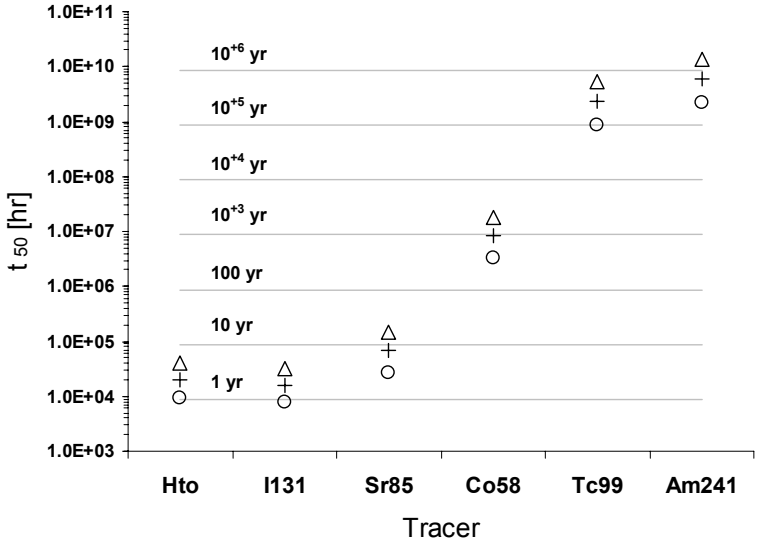

Figure 105 *Breakthrough times for 50% (t_{50}) of the Dirac pulse injected tracer (3DQ2). 5% (circles), 50% (+ symbols), and 95% (triangles) percentile levels are shown for the simulated results.*

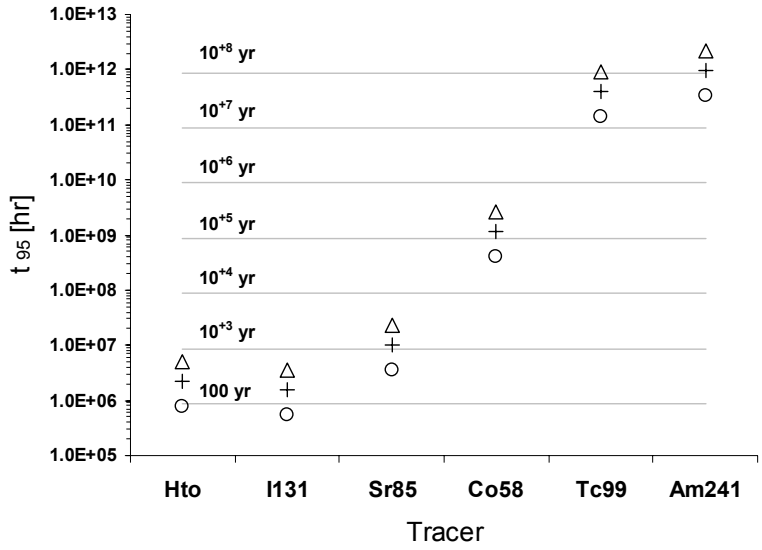

Figure 106 *Breakthrough times for 95% (t_{95}) of the Dirac pulse injected tracer (3DQ2). 5% (circles), 50% (+ symbols), and 95% (triangles) percentile levels are shown for the simulated results.*

Maximum nuclide release rate (3DQ2)

Table 11 **Maximum nuclide release rate [Bq/y] for simulation series 3DQ2. Results are given for Dirac pulse data only. Simulation data is based upon mean peak breakthrough concentration for 100 realisations where the injected mass is the same as that used in Task 6A. The maximum nuclide release rate for the constant injection boundary condition (1 MBq/y), however, is obtained when the system has attained steady state and is 1 MBq/y.**

Tracer	Dirac-M_R [Bq/y]
Hto	4.44×10^{5}
^{131}I	5.49×10^{5}
^{85}Sr	1.39×10^{5}
^{58}Co	1.10×10^{3}
^{99}Tc	4.04
^{241}Am	1.63

Comparison of Task 6A (3DQ1) and Task 6B (3DQ2) tracer arrival times

Table 12 **Mean travel time (t_{05}) and standard deviation (σ_{t05}) for Task 6B Dirac pulse simulation results (3DQ2), and arrival time ratios for comparison between Task 6A (3DQ1) and Task 6B simulation results. Time ratios are Task 6B arrival times divided by Task 6A arrival times.**

Tracer	Dirac-t_{05} [h]	Dirac-σ_{t05}	t_{05}-Ratio
Hto	5.24×10^{3}	1.75×10^{3}	1.47×10^{3}
^{131}I	4.86×10^{3}	1.56×10^{3}	1.36×10^{3}
^{85}Sr	1.00×10^{4}	4.17×10^{3}	2.27×10^{3}
^{58}Co	1.42×10^{6}	5.96×10^{5}	1.95×10^{3}
^{99}Tc	2.09×10^{8}	1.18×10^{8}	1.10×10^{4}
^{241}Am	5.19×10^{8}	2.92×10^{8}	1.09×10^{4}

Table 13 **Mean travel time (t_{50}) and standard deviation (σ_{t50}) for Task 6B Dirac pulse simulation results (3DQ2), and arrival time ratios for comparison between Task 6A (3DQ1) and Task 6B simulation results. Time ratios are Task 6B arrival times divided by Task 6A arrival times.**

Tracer	Dirac-t_{50} [h]	Dirac-σ_{t50}	t_{50}-Ratio
Hto	2.11×10^{4}	9.51×10^{3}	3.80×10^{3}
^{131}I	1.66×10^{4}	7.04×10^{3}	3.00×10^{3}
^{85}Sr	7.57×10^{4}	3.89×10^{4}	1.07×10^{4}
^{58}Co	9.31×10^{6}	4.67×10^{6}	7.22×10^{3}
^{99}Tc	2.74×10^{9}	1.48×10^{9}	7.34×10^{4}
^{241}Am	6.80×10^{9}	3.68×10^{9}	7.28×10^{4}

Table 14 **Mean travel time (t_{95}) and standard deviation (σ_{t95}) for Task 6B Dirac pulse simulation results (3DQ2), and arrival time ratios for comparison between Task 6A (3DQ1) and Task 6B simulation results. Time ratios are Task 6B arrival times divided by Task 6A arrival times.**

Tracer	Dirac-t_{95} [h]	Dirac-σ_{t95}	t_{95}-Ratio
Hto	2.38×10^{6}	1.28×10^{6}	1.58×10^{5}
^{131}I	1.65×10^{6}	8.89×10^{5}	1.14×10^{5}
^{85}Sr	1.08×10^{7}	5.85×10^{6}	4.07×10^{5}
^{58}Co	1.24×10^{9}	6.71×10^{8}	2.27×10^{5}
^{99}Tc	4.30×10^{11}	2.32×10^{11}	8.35×10^{5}
^{241}Am	1.07×10^{12}	5.75×10^{11}	8.34×10^{5}

Breakthrough time summary for modelled tracers (2DQ2)

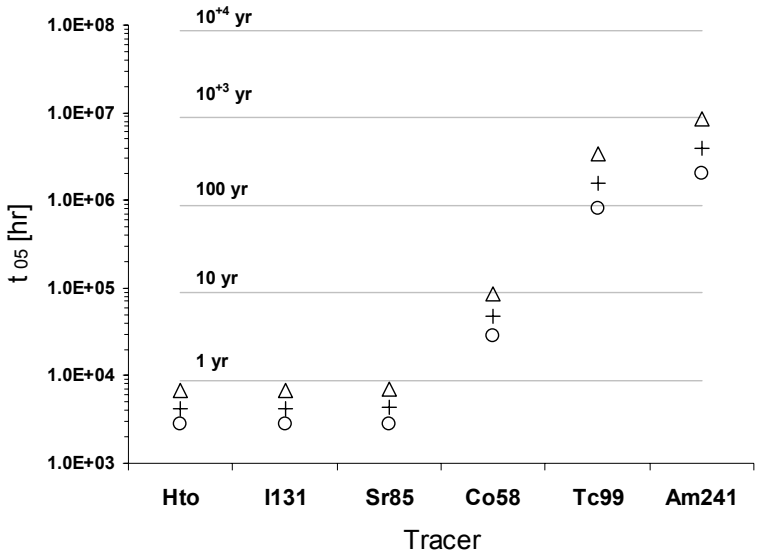

Figure 107 *Breakthrough times for 5% (t_{05}) of the Dirac pulse injected tracer (2DQ2). 5% (circles), 50% (+ symbols), and 95% (triangles) percentile levels are shown for the simulated results. Experimental results (squares) are shown for Hto, ^{131}I, ^{85}Sr, and ^{58}Co.*

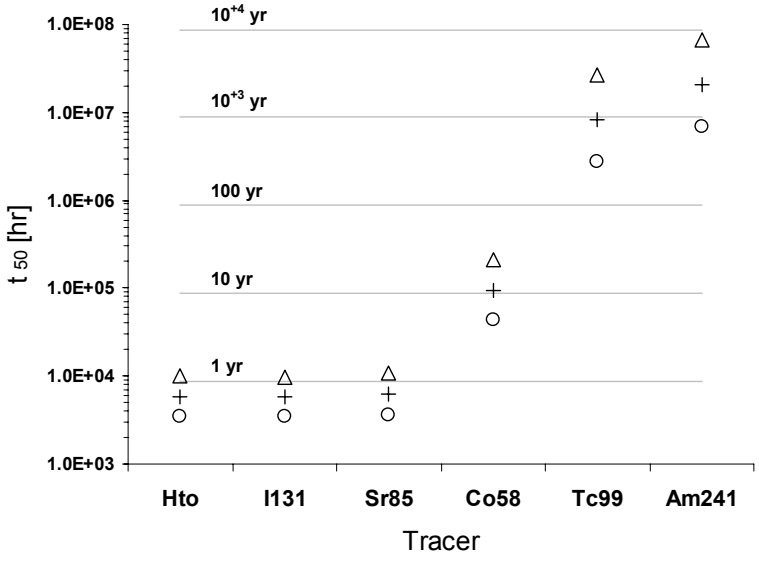

Figure 108 *Breakthrough times for 50% (t_{50}) of the Dirac pulse injected tracer (2DQ2). 5% (circles), 50% (+ symbols), and 95% (triangles) percentile levels are shown for the simulated results. Experimental results (squares) are shown for Hto, ^{131}I, ^{85}Sr, and ^{58}Co.*

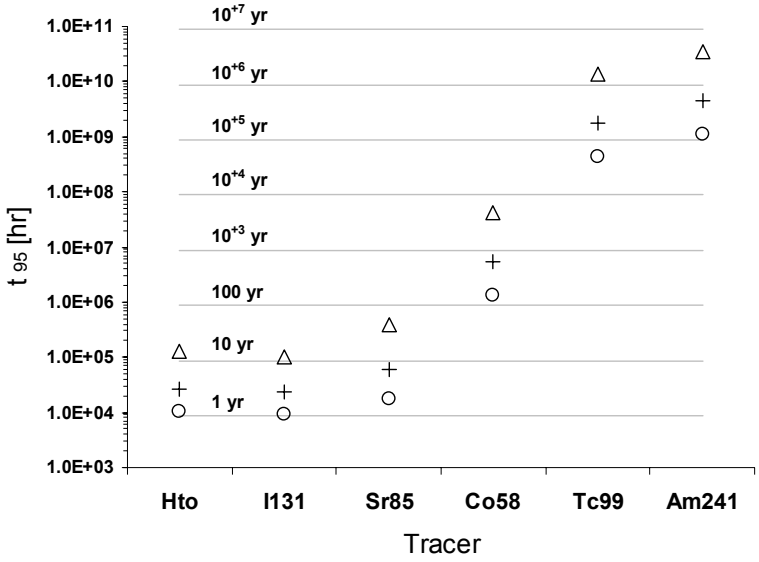

Figure 109 *Breakthrough times for 95% (t_{95}) of the Dirac pulse injected tracer (2DQ2). 5% (circles), 50% (+ symbols), and 95% (triangles) percentile levels are shown for the simulated results. Experimental results (squares) are shown for Hto, ^{131}I, ^{85}Sr, and ^{58}Co.*

Maximum nuclide release rate (2DQ2)

Table 15 **Maximum nuclide release rate [Bq/y] for simulation series 2DQ2. Results are given for Dirac pulse data only. Simulation data is based upon mean peak breakthrough concentration for 100 realisations where the injected mass is the same as that used in the Task 6A simulations. The maximum nuclide release rate for the constant injection boundary condition (1 MBq/y), however, is obtained when the system has attained steady state and is 1 MBq/y.**

Tracer	Dirac-M_R [Bq/y]
Hto	4.73×10^{6}
^{131}I	5.23×10^{6}
^{85}Sr	2.30×10^{6}
^{58}Co	1.02×10^{5}
^{99}Tc	9.83×10^{2}
^{241}Am	3.93×10^{2}

Comparison of Task 6A (2DQ1) and Task 6B (2DQ2) tracer arrival times

Table 16 **Mean travel time (t_{05}) and standard deviation (σ_{t05}) for Task 6B Dirac pulse simulation results (2DQ2), and arrival time ratios for comparison between Task 6A (2DQ1) and Task 6B simulation results. Time ratios are Task 6B arrival times divided by Task 6A arrival times.**

Tracer	Dirac-t_{05} [h]	Dirac-σ_{t05}	t_{05}-Ratio
Hto	5.16×10^{3}	1.53×10^{3}	1.01×10^{3}
^{131}I	5.15×10^{3}	1.52×10^{3}	1.01×10^{3}
^{85}Sr	5.28×10^{3}	1.58×10^{3}	1.02×10^{3}
^{58}Co	5.34×10^{4}	1.89×10^{4}	1.10×10^{3}
^{99}Tc	1.88×10^{6}	9.02×10^{5}	1.72×10^{3}
^{241}Am	4.68×10^{6}	2.25×10^{6}	1.72×10^{3}

Table 17 **Mean travel time (t_{50}) and standard deviation (σ_{t50}) for Task 6B Dirac pulse simulation results (2DQ2), and arrival time ratios for comparison between Task 6A (2DQ1) and Task 6B simulation results. Time ratios are Task 6B arrival times divided by Task 6A arrival times.**

Tracer	Dirac-t_{50} [h]	Dirac-σ_{t50}	t_{50}-Ratio
Hto	7.43×10^{3}	2.52×10^{3}	1.05×10^{3}
^{131}I	7.36×10^{3}	2.48×10^{3}	1.05×10^{3}
^{85}Sr	7.95×10^{3}	2.82×10^{3}	1.11×10^{3}
^{58}Co	1.14×10^{5}	5.52×10^{4}	1.55×10^{3}
^{99}Tc	1.15×10^{7}	8.39×10^{6}	6.63×10^{3}
^{241}Am	2.86×10^{7}	2.09×10^{7}	6.64×10^{3}

Table 18 **Mean travel time (t_{95}) and standard deviation (σ_{t95}) for Task 6B Dirac pulse simulation results (2DQ2), and arrival time ratios for comparison between Task 6A (2DQ1) and Task 6B simulation results. Time ratios are Task 6B arrival times divided by Task 6A arrival times.**

Tracer	Dirac-t_{95} [h]	Dirac-σ_{t95}	t_{95}-Ratio
Hto	4.27×10^{4}	3.54×10^{4}	1.93×10^{3}
^{131}I	3.74×10^{4}	2.88×10^{4}	1.70×10^{3}
^{85}Sr	1.08×10^{5}	1.17×10^{5}	4.68×10^{3}
^{58}Co	1.03×10^{7}	1.25×10^{7}	2.09×10^{4}
^{99}Tc	3.39×10^{9}	4.18×10^{9}	2.04×10^{5}
^{241}Am	8.46×10^{9}	1.04×10^{10}	2.04×10^{5}

Comparison of 2D & 3D simulations (constant injection) – 3DQ2, 2DQ2

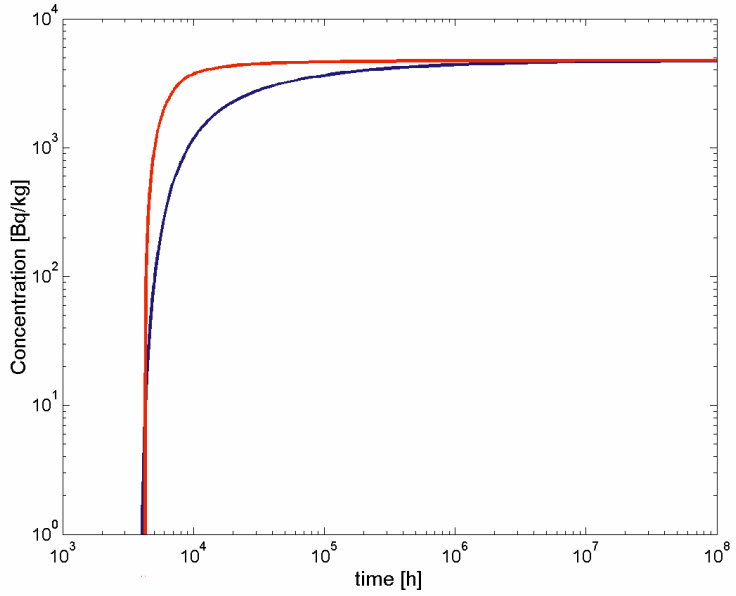

Figure 110 *Breakthrough concentration-time profile for Hto (1 MBq/y constant injection). The blue curve shows data for 3D simulations (3DQ2). The red curve indicates data for 2D simulations (2DQ2).*

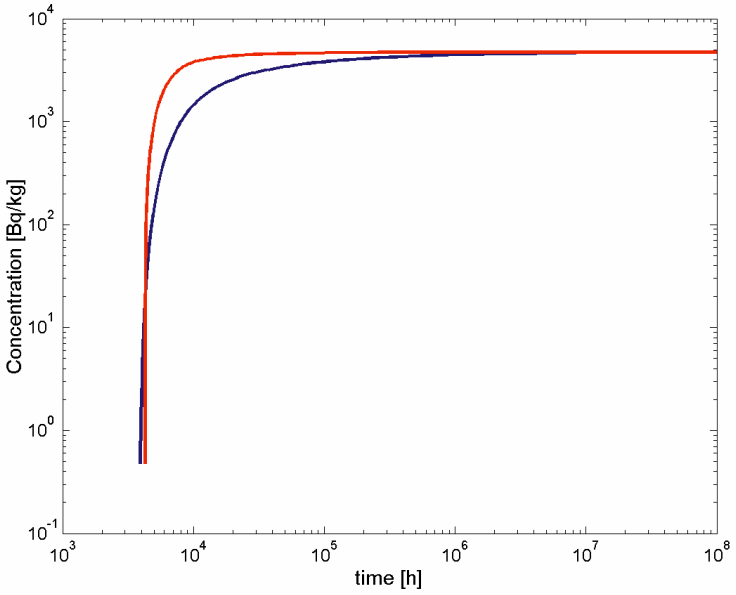

Figure 111 *Breakthrough concentration-time profile for ^{131}I (1 MBq/y constant injection). The blue curve shows data for 3D simulations (3DQ2). The red curve indicates data for 2D simulations (2DQ2).*

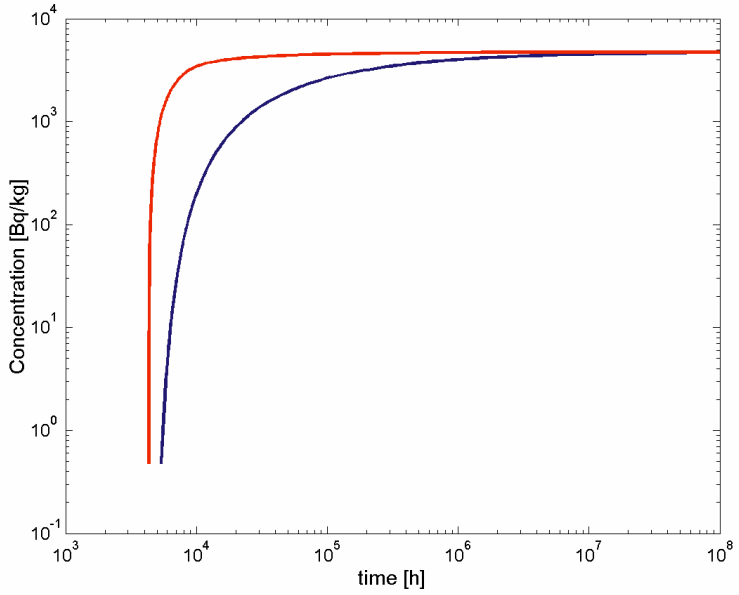

Figure 112 *Breakthrough concentration-time profile for ^{85}Sr (1 MBq/y constant injection). The blue curve shows data for 3D simulations (3DQ2). The red curve indicates data for 2D simulations (2DQ2).*

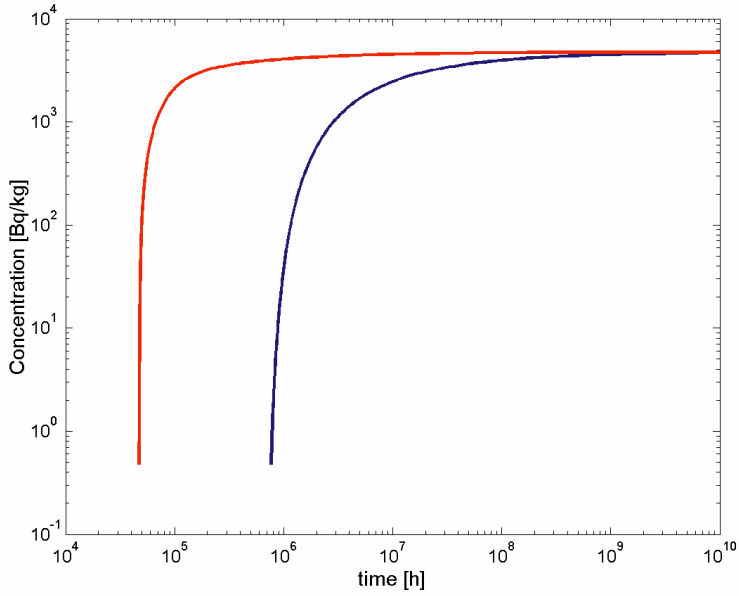

Figure 113 *Breakthrough concentration-time profile for ^{58}Co (1 MBq/y constant injection). The blue curve shows data for 3D simulations (3DQ2). The red curve indicates data for 2D simulations (2DQ2).*

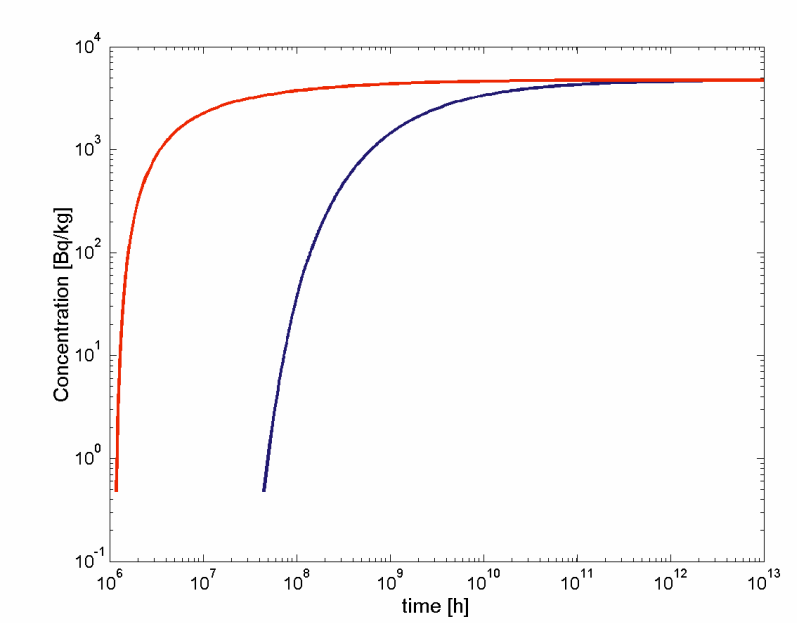

Figure 114 *Breakthrough concentration-time profile for ^{99}Tc (1 MBq/y constant injection). The blue curve shows data for 3D simulations (3DQ2). The red curve indicates data for 2D simulations (2DQ2).*

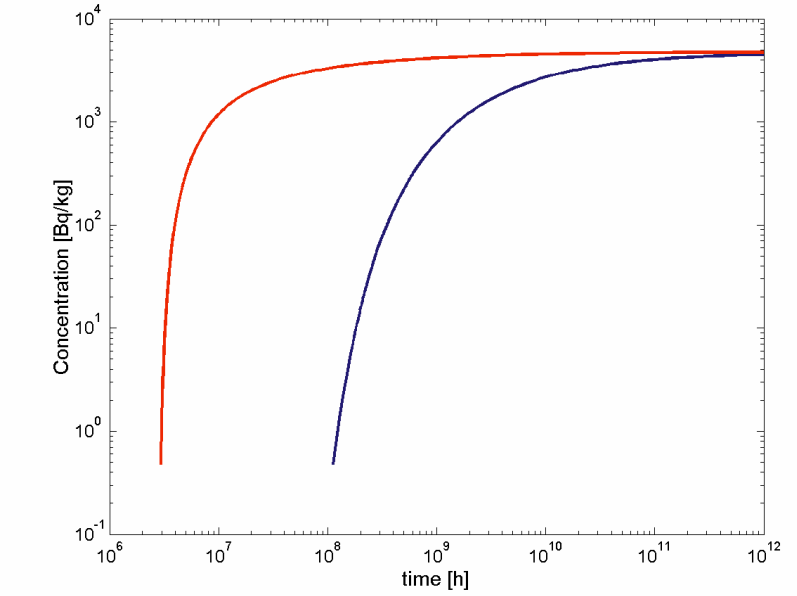

Figure 115 *Breakthrough concentration-time profile for ^{241}Am (1 MBq/y constant injection). The blue curve shows data for 3D simulations (3DQ2). The red curve indicates data for 2D simulations (2DQ2).*

Appendix 4

Task 6B2. Breakthrough Concentration-Time Curves (BTC)

– **Comparison of selected simulations (Dirac pulse) with and without background fracturing**

Comparison of selected simulations (Dirac pulse) for cases with and without background fracturing

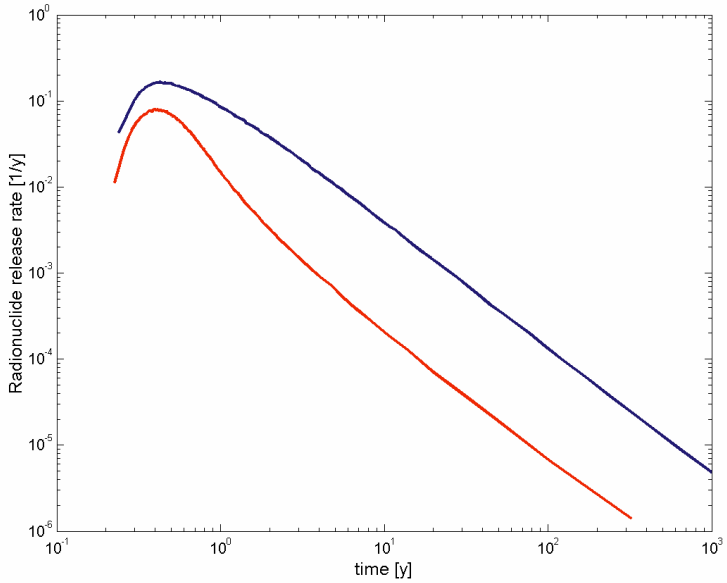

Figure 116 *Breakthrough flux-time profile for Hto Dirac pulse where Feature A transmissivity is 10 times the background value. The blue curve shows data for simulations with background fractures. The red curve indicates data for simulations without background fractures.*

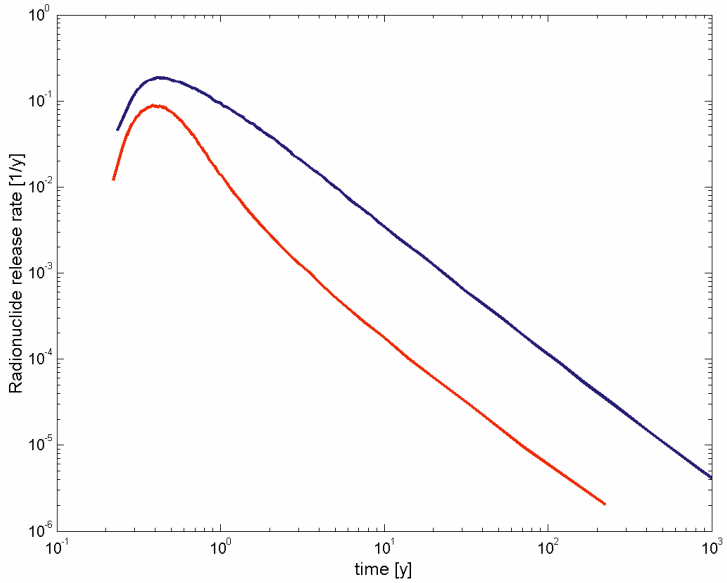

Figure 117 *Breakthrough flux-time profile for ^{131}I Dirac pulse where Feature A transmissivity is 10 times the background value. The blue curve shows data for simulations with background fractures. The red curve indicates data for simulations without background fractures.*

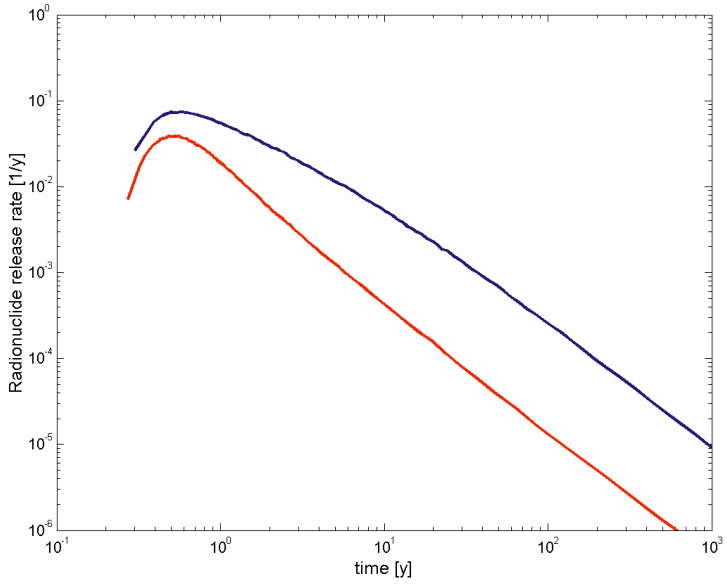

Figure 118 *Breakthrough flux-time profile for ^{85}Sr Dirac pulse where Feature A transmissivity is 10 times the background value. The blue curve shows data for simulations with background fractures. The red curve indicates data for simulations without background fractures.*

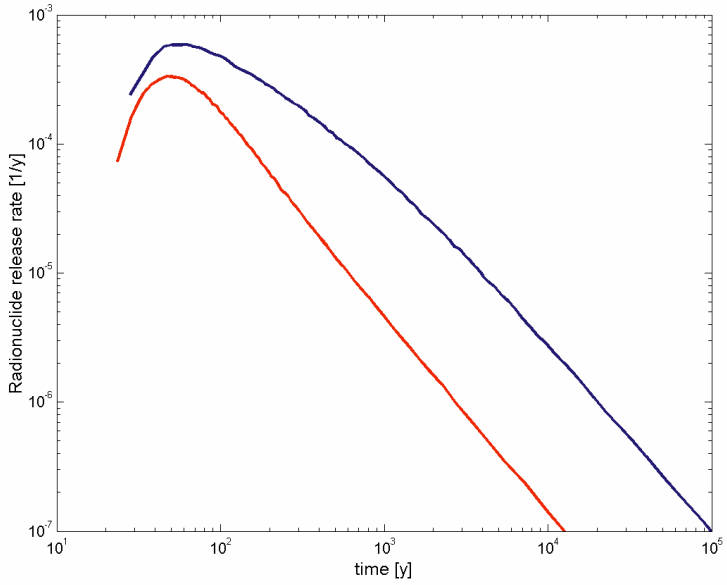

Figure 119 *Breakthrough flux-time profile for ^{58}Co Dirac pulse where Feature A transmissivity is 10 times the background value. The blue curve shows data for simulations with background fractures. The red curve indicates data for simulations without background fractures.*

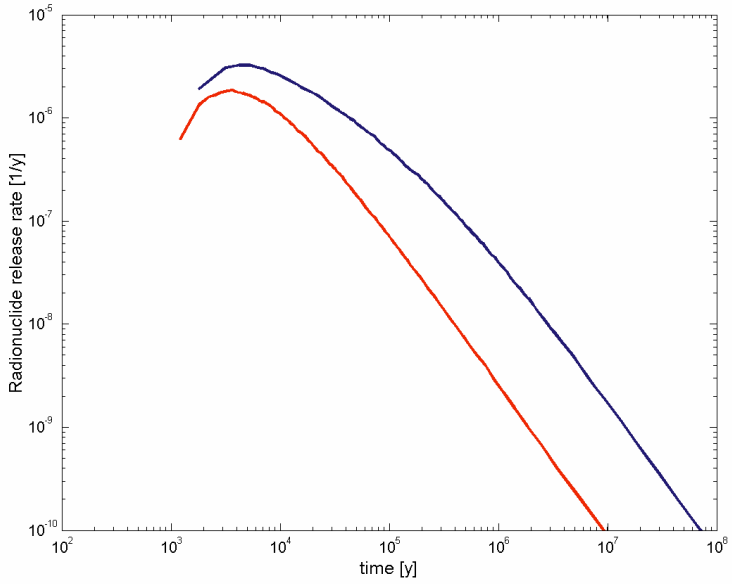

Figure 120 *Breakthrough flux-time profile for ^{99}Tc Dirac pulse where Feature A transmissivity is 10 times the background value. The blue curve shows data for simulations with background fractures. The red curve indicates data for simulations without background fractures.*

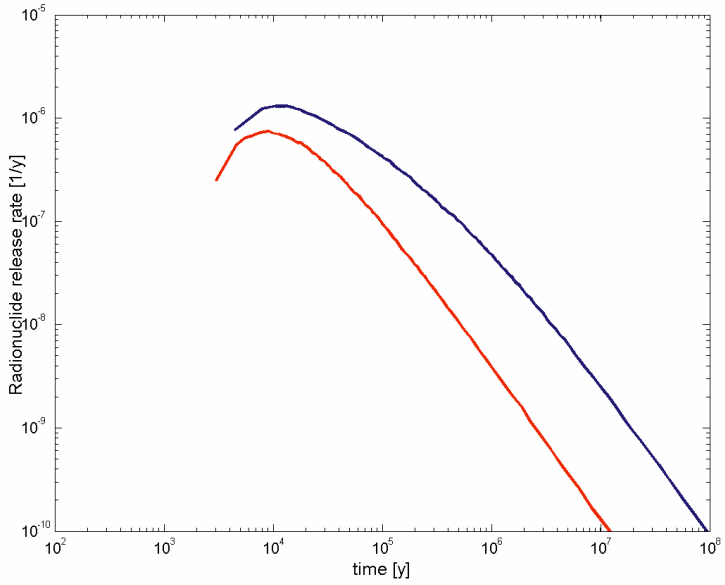

Figure 121 *Breakthrough flux-time profile for ^{241}Am Dirac pulse where Feature A transmissivity is 10 times the background value. The blue curve shows data for simulations with background fractures. The red curve indicates data for simulations without background fractures.*

Breakthrough time summary for modelled tracers – simulations with background fractures

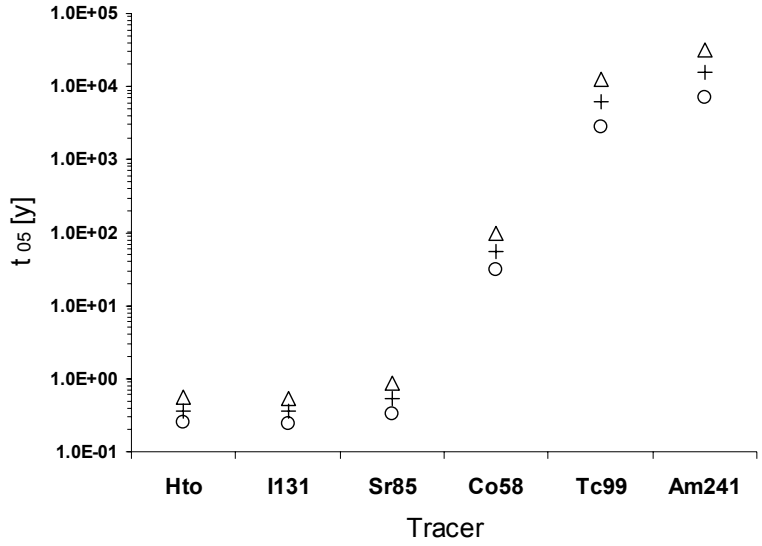

Figure 122 *Breakthrough times for 5% (t_{05}) of the Dirac pulse injected tracer where Feature A transmissivity is 10 times the background value. 5% (circles), 50% (+ symbols), and 95% (triangles) percentile levels are shown for the simulated results.*

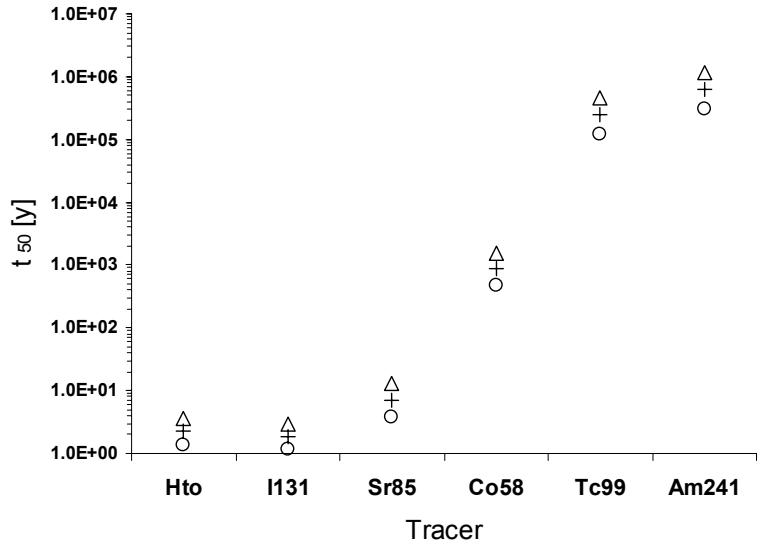

Figure 123 *Breakthrough times for 50% (t_{50}) of the Dirac pulse injected tracer where Feature A transmissivity is 10 times the background value. 5% (circles), 50% (+ symbols), and 95% (triangles) percentile levels are shown for the simulated results.*

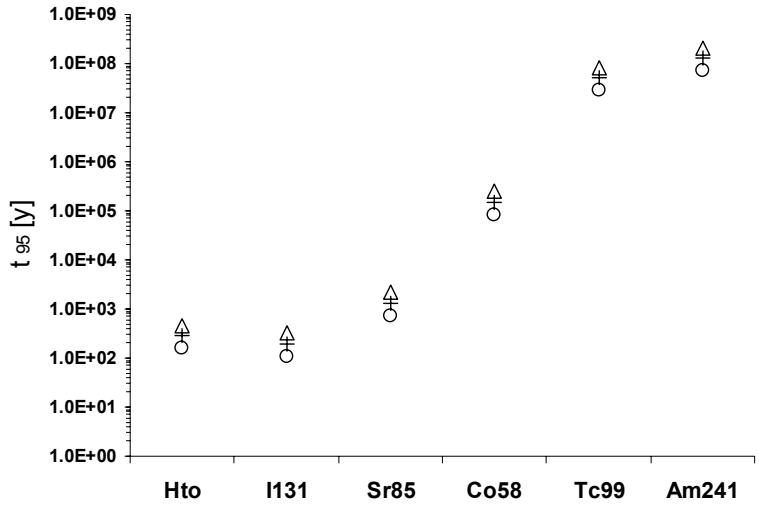

Figure 124 *Breakthrough times for 95% (t_{95}) of the Dirac pulse injected tracer where Feature A transmissivity is 10 times the background value. 5% (circles), 50% (+ symbols), and 95% (triangles) percentile levels are shown for the simulated results.*

Breakthrough time summary for modelled tracers – simulations without background fractures

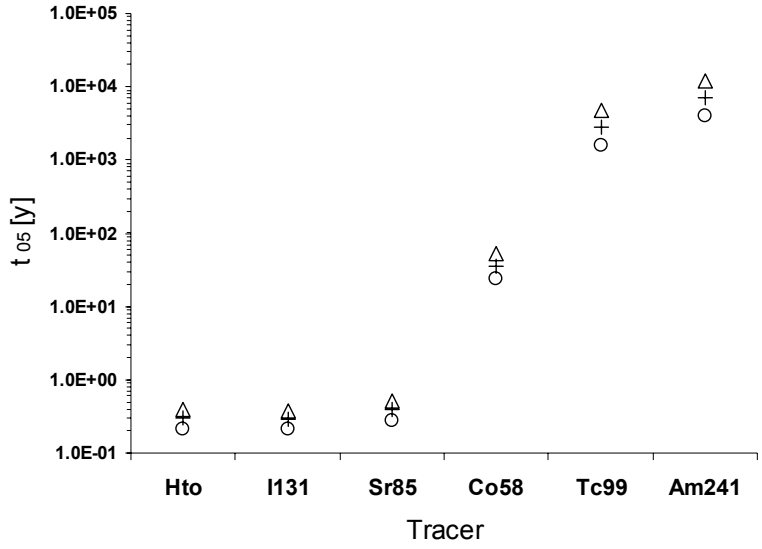

Figure 125 *Breakthrough times for 5% (t_{05}) of the Dirac pulse injected tracer where Feature A transmissivity is 10 times the background value. 5% (circles), 50% (+ symbols), and 95% (triangles) percentile levels are shown for the simulated results.*

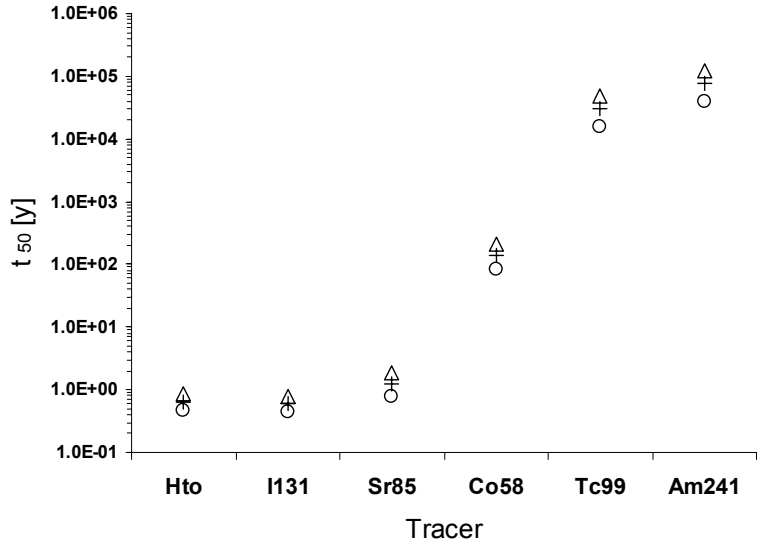

Figure 126 *Breakthrough times for 50% (t_{50}) of the Dirac pulse injected tracer where Feature A transmissivity is 10 times the background value. 5% (circles), 50% (+ symbols), and 95% (triangles) percentile levels are shown for the simulated results.*

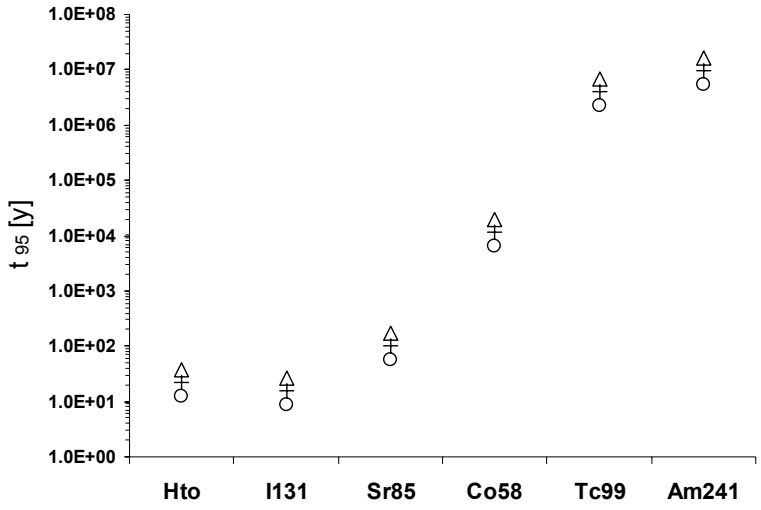

Figure 127 *Breakthrough times for 95% (t_{95}) of the Dirac pulse injected tracer where Feature A transmissivity is 10 times the background value. 5% (circles), 50% (+ symbols), and 95% (triangles) percentile levels are shown for the simulated results.*

Maximum nuclide release rate

Table 19 Maximum nuclide release rate [1/y] for simulations both with (case 1) and without background fractures (case 2). Results are given for Dirac pulse data only where Feature A transmissivity is 10 times the background value. Simulation data is based upon mean peak breakthrough concentration for 100 realisations.

Tracer	Case 1 [1/y]	Case 2 [1/y]
Hto	0.16	0.079
^{131}I	0.19	0.088
^{85}Sr	7.4×10^{-2}	0.039
^{58}Co	5.9×10^{-4}	3.4×10^{-4}
^{99}Tc	3.3×10^{-6}	1.9×10^{-6}
^{241}Am	1.3×10^{-6}	7.5×10^{-7}

Comparison of simulations for cases with and without background fractures (constant injection)

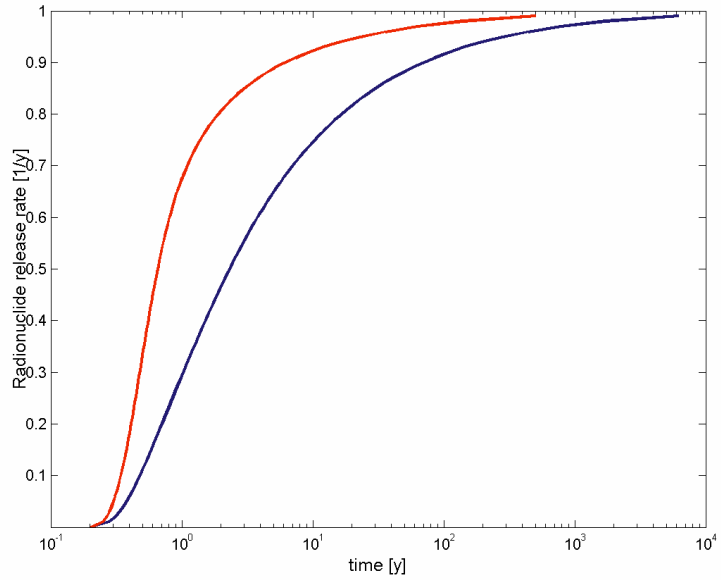

Figure 128 *Breakthrough concentration-time profile for Hto (constant injection) where Feature A transmissivity is 10 times the background value. The blue curve shows data for simulations with background fractures. The red curve indicates data for simulations without background fractures.*

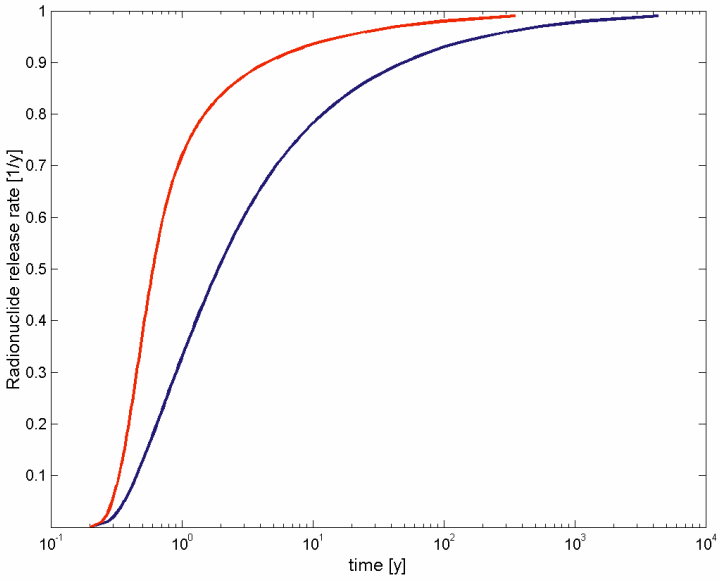

Figure 129 *Breakthrough concentration-time profile for ^{131}I (constant injection) where Feature A transmissivity is 10 times the background value. The blue curve shows data for simulations with background fractures. The red curve indicates data for simulations without background fractures.*

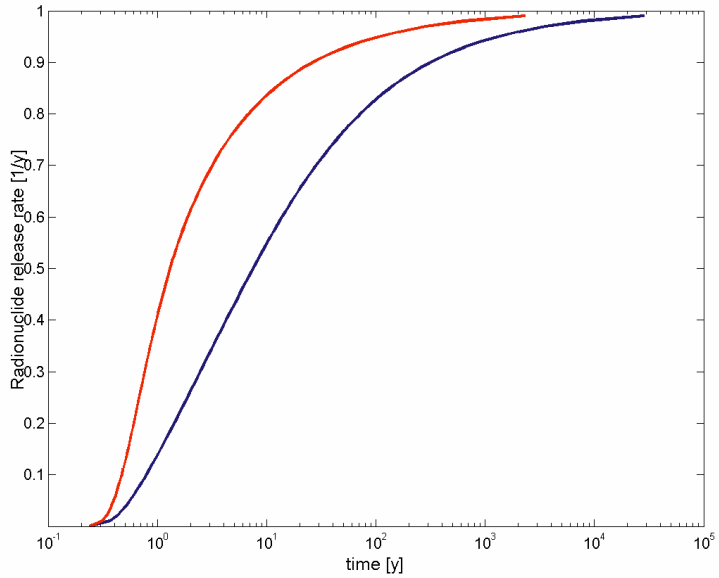

Figure 130 *Breakthrough concentration-time profile for ^{85}Sr (constant injection) where Feature A transmissivity is 10 times the background value. The blue curve shows data for simulations with background fractures. The red curve indicates data for simulations without background fractures.*

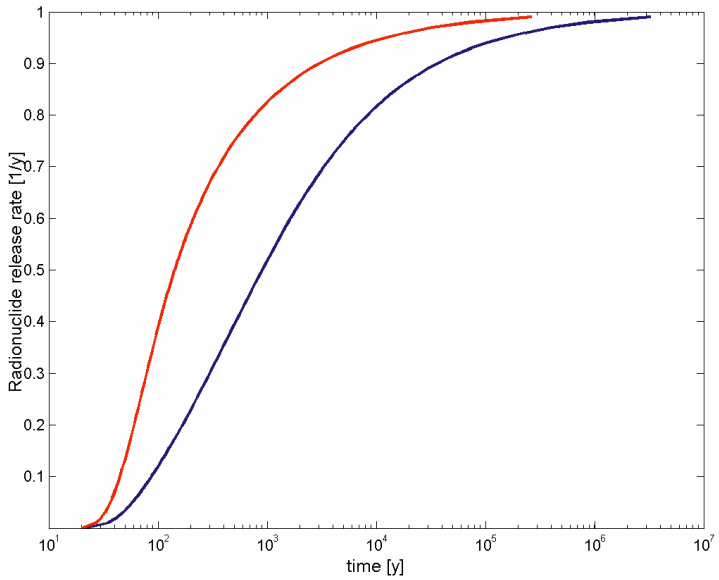

Figure 131 *Breakthrough concentration-time profile for ^{58}Co (constant injection) where Feature A transmissivity is 10 times the background value. The blue curve shows data for simulations with background fractures. The red curve indicates data for simulations without background fractures.*

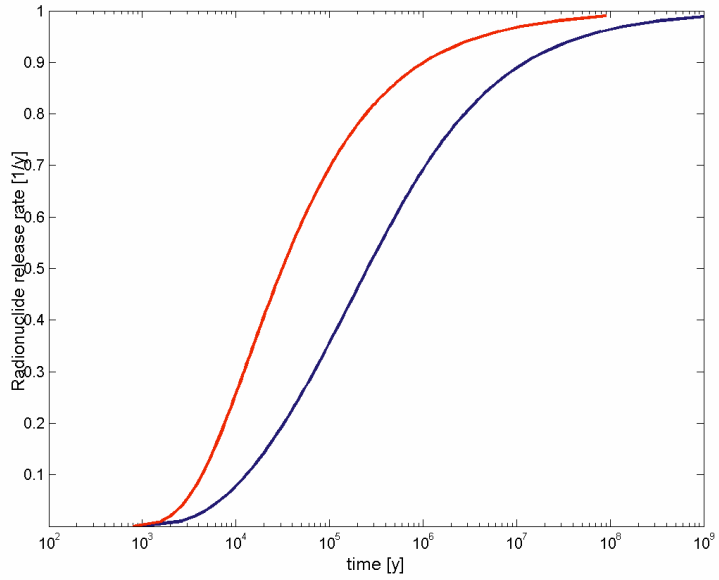

Figure 132 *Breakthrough concentration-time profile for ^{99}Tc (constant injection) where Feature A transmissivity is 10 times the background value. The blue curve shows data for simulations with background fractures. The red curve indicates data for simulations without background fractures.*

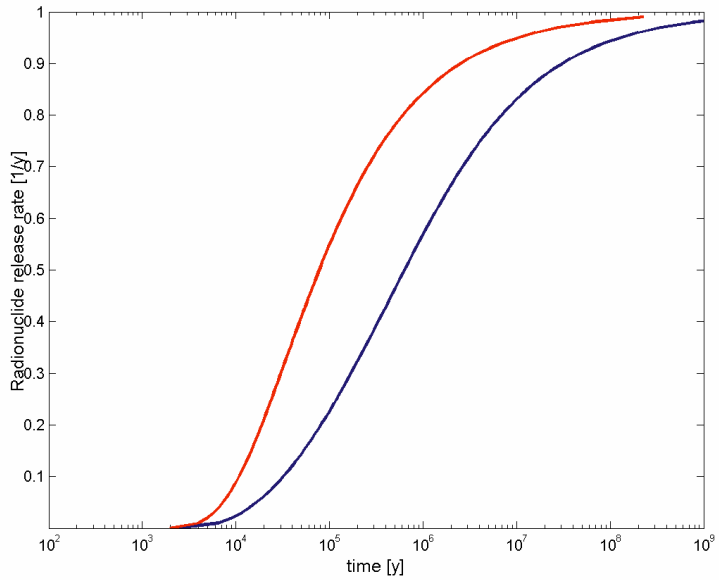

Figure 133 *Breakthrough concentration-time profile for ^{241}Am (constant injection) where Feature A transmissivity is 10 times the background value. The blue curve shows data for simulations with background fractures. The red curve indicates data for simulations without background fractures.*

Appendix 5

Sensitivity Analysis Concerning Channel Lengths

– **Comparison of 2D & 3D simulations with varying channel lengths**

Comparison of 2D & 3D simulations with varying channel lengths

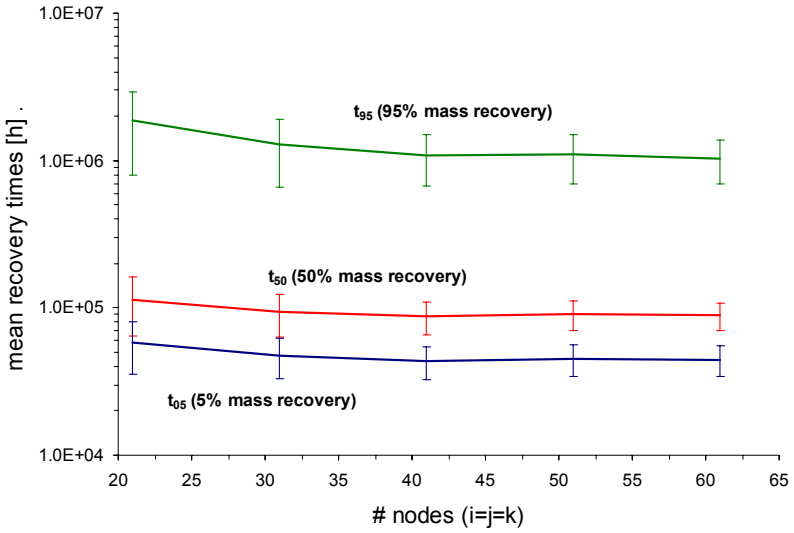

Figure 134 *Sensitivity of the simulated mean arrival times t_{05}, t_{50}, and t_{95} for ^{241}Am where the channel length has been varied from 0.25 m (61×61×61 nodes) to 0.75 m (21×21×21 nodes) within a constant simulation volume of 13 500 m^3. Simulation results consider a 3D flow field, a pumping flowrate of 0.4 l/min (Task 6A) and a Dirac pulse tracer injection boundary condition.*

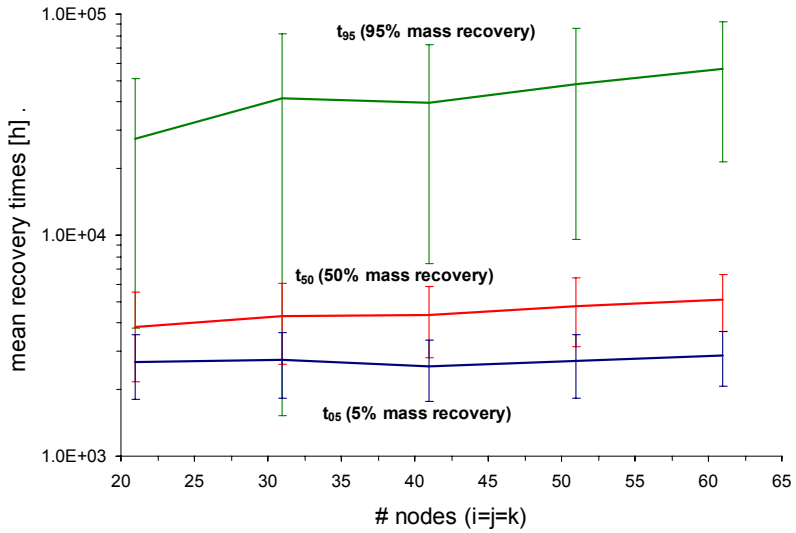

Figure 135 *Sensitivity of the simulated mean arrival times t_{05}, t_{50}, and t_{95} for ^{241}Am where the channel length has been varied from 0.25 m (61×61×61 nodes) to 0.75 m (21×21×21 nodes) within a constant simulation volume of 13 500 m^3. Simulation results consider a 2D flow field, a pumping flowrate of 0.4 l/min (Task 6A) and a Dirac pulse tracer injection boundary condition.*

Table 20 **Comparison of 2D and 3D simulations for ^{241}Am transport with varying numbers of network nodes in the simulation cube (Task 6A). The dimensions of the channel network was varied from 21×21×21 nodes up to 61×61×61 nodes. Data given includes: average number of channels traversed by particles from injection node to recovery node, FWS per channel, total FWS encountered along transport path, average flowrate (F_m) expected at a distance of 5 m from the recovery node, and the nominal FWS/q ratio based upon total FWS and F_m**

# nodes	21	31	41	51	61
L [m]	0.75	0.5	0.375	0.30	0.25
3D simulations:					
# channels traversed	12.38±1.08	18.48±1.22	24.16±1.33	30.58±1.58	36.15±1.44
FWS/channel [m^2]	0.98	0.29	0.12	0.06	0.04
total FWS [m^2]	12.19	5.39	2.97	1.93	1.32
F_m [m^3/y]	0.376	0.167	0.094	0.060	0.042
Nominal FWS/q	32.37	32.22	31.59	31.98	31.51
2D simulations:					
# channels traversed	10.07±0.93	15.15±1.22	20.08±1.28	25.04±1.28	30.18±1.42
FWS/channel [m^2]	0.56	0.25	0.14	0.09	0.06
total FWS [m^2]	5.66	3.79	2.82	2.25	1.89
F_m [m^3/y]	5.019	3.346	2.510	2.008	1.673
Nominal FWS/q	1.13	1.13	1.13	1.12	1.13

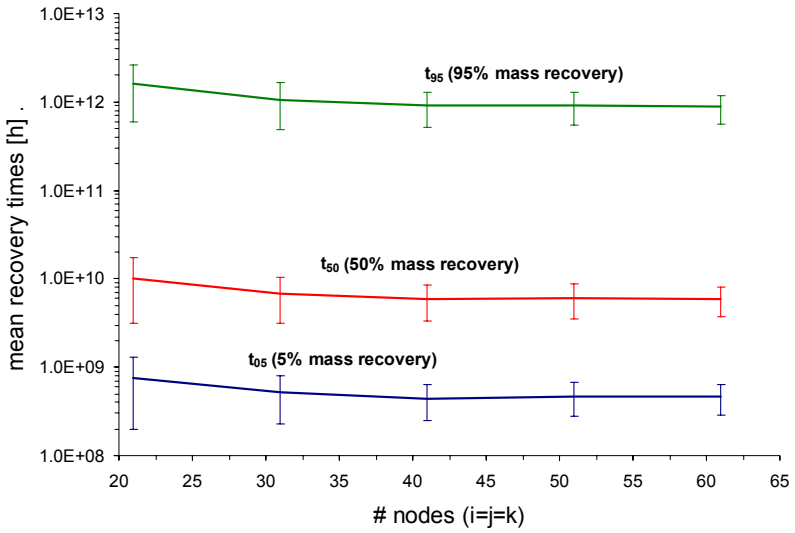

Figure 136 *Sensitivity of the simulated mean arrival times t_{05}, t_{50}, and t_{95} for ^{241}Am where the channel length has been varied from 0.25 m (61×61×61 nodes) to 0.75 m (21×21×21 nodes) within a constant simulation volume of 13 500 m^3. Simulation results consider a 3D flow field, a pumping flowrate of 0.4 µl/min (Task 6B) and a Dirac pulse tracer injection boundary condition.*

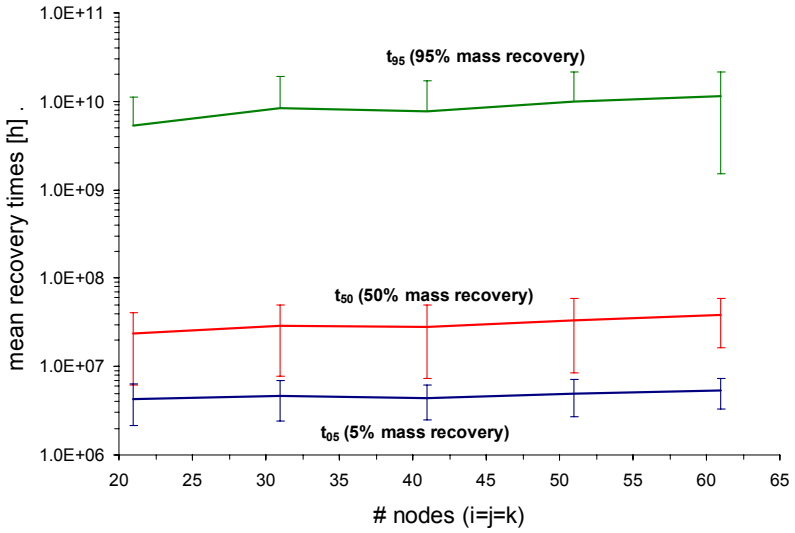

Figure 137 *Sensitivity of the simulated mean arrival times t_{05}, t_{50}, and t_{95} for ^{241}Am where the channel length has been varied from 0.25 m (61×61×61 nodes) to 0.75 m (21×21×21 nodes) within a constant simulation volume of 13 500 m^3. Simulation results consider a 2D flow field, a pumping flowrate of 0.4 µl/min (Task 6B) and a Dirac pulse tracer injection boundary condition. In some cases the 1-σ error for t_{95} is equal to or larger than the mean value and thus the lower error bar can therefore not be shown.*

Table 21 **Comparison of 2D and 3D simulations for ^{241}Am transport with varying numbers of network nodes in the simulation cube (Task 6B). The dimensions of the channel network was varied from 21×21×21 nodes up to 61×61×61 nodes. Data given includes: average number of channels traversed by particles from injection node to recovery node, FWS per channel, total FWS encountered along transport path, average flowrate (F_m) expected at a distance of 5 m from the recovery node, and the nominal FWS/q ratio based upon total FWS and F_m.**

# nodes	21	31	41	51	61
L [m]	0.75	0.5	0.375	0.30	0.25
3D simulations:					
# channels traversed	12.38±1.08	18.48±1.22	24.16±1.33	30.58±1.58	36.15±1.44
FWS/channel [m^2]	0.98	0.29	0.12	0.06	0.04
total FWS [m^2]	12.19	5.39	2.97	1.93	1.32
F_m [m^3/y]	3.76×10^{-4}	1.67×10^{-4}	9.41×10^{-5}	6.02×10^{-5}	4.18×10^{-5}
Nominal FWS/q	32374	32219	31593	31982	31513
2D simulations:					
# channels traversed	10.07±0.93	15.15±1.22	20.08±1.28	25.04±1.28	30.18±1.42
FWS/channel [m^2]	0.56	0.25	0.14	0.09	0.06
total FWS [m^2]	5.66	3.79	2.82	2.25	1.89
F_m [m^3/y]	5.02×10^{-3}	3.35×10^{-3}	2.51×10^{-3}	2.01×10^{-3}	1.67×10^{-3}
Nominal FWS/q	1128	1132	1125	1122	1127